On wave propagation in saturated and partially saturated porous media

Please check the document version of this publication:

• A submitted manuscript is the version of the article upon submission and before peer-review. There can be important differences between the submitted version and the official published version of record. People interested in the research are advised to contact the author for the final version of the publication, or visit the DOI to the publisher's website.
• The final author version and the galley proof are versions of the publication after peer review.
• The final published version features the final layout of the paper including the volume, issue and page numbers.

[Link to publication](#)

On wave propagation in saturated and partially saturated porous media

D.M.J. Smeulders

On wave propagation in saturated and partially saturated porous media

DAVID MARIA JACOBUS SMEULDERS

geboren te Nuenen

Dit proefschrift is goedgekeurd door de promotoren

prof.dr.ir. G. Vossers
en
prof.dr.ir. A. Verruijt.

Co-promotor:
dr.ir. M.E.H. van Dongen

Contents

1 Introduction

1.1 Background

Wave propagation phenomena in porous media are investigated by several research disciplines. In petrophysics, identification of oil and gas containing geological strata is a major point of interest. At the earth's surface, waves are produced by means of explosive charges or vibration tables. Analysis of reflected waves provides information about the geological subsoil. Using fast parallel computer facilities (Cray), crustal reconstruction is possible up to a depth of about 1 km. Exploitation of an oil well is only possible when sufficient knowledge about permeability and porosity properties of the oil containing strata is available. This is even more the case for enhanced oil recovery, when techniques like water or steam injection are applied to fully exploit an oil well. The drilling of bore holes, and the subsequent application of acoustic well logging, is commonly practised to gain information about permeability and porosity properties of the earth's subsoil. Propagation and damping of Rayleigh and Stonely surface waves is measured (Hsui & Toksöz 1986; Cheruvier & Winkler 1987).

Civil engineers are occupied by different problems like the effects of wave impacts on dikes (Ruygrok & van der Kogel 1980; Ebbens, Molenkamp & Ruygrok 1988) or pile-soil interactions under static and dynamic loadings (Boulon 1988). Soil-water-structure interactions are of interest in offshore industry, where large oil platforms have to be constructed, often involving offshore pile driving techniques, or during earthquakes, where liquefaction of the soil may, in some cases, occur.

In marine geophysics, acoustical techniques are used for studying sedimentary and crustal structures of the ocean basins. Research programmes are directed towards understanding the deep ocean processes that generate oceanic sediments and crustal layers. These processes directly affect the physical and acoustic properties of the sea floor, and are the origin of bathymetric, gravity and magnetic variations in the ocean basins. Acoustic and nonacoustic submarine and antisubmarine operations, inertial navigation and guidance, and a variety of other naval operations are directely influenced by the ocean floor. Questions about the continuity and source of the prominent refracting and reflecting layers of the ocean floor are studied by

underway single ship investigations and ocean floor instrumentation. Use is made of echo sounders, sparker arrays and airguns as sound sources, and detection is provided by multisensor towed arrays, sonobuoys or seismometers (Hampton 1974).

The absorbtion and reflection of sound waves is, obviously, of interest for lowering noise levels in industry, where for example the application of sound absorbing materials is studied, or in traffic, where, only recently, highly porous road covering is applied. Theoretical studies about sound absorbing materials were already performed in 1949 (Zwikker & Kosten).

In all the disciplines that we mentioned above, it has been noticed that the presence of small gasfractions in liquid-saturated pores has an immense effect on wave propagation, damping and reflection phenomena (see e.g. Anderson & Hampton 1980). The aim of the present study is to verify and to improve models describing wave propagation and damping in partially saturated porous media. Doing so, we will first give a survey of the two-phase theory for wave propagation in fully saturated elastic media, which is usually denoted as the Biot theory. This is done in chapter 2. Computational results for wave propagation and damping in a cylindrical porous sample are presented in chapter 3. Next, we will discuss the damping mechanisms of vibrating gas bubbles in a porous system. Darcy damping, thermal damping, viscous damping and acoustic damping will be treated. The effects of oscillating gas bubbles on wave propagation and damping are considered. It appears that it is convenient to introduce a dynamic compressibility of the pore fluid. All this is presented in chapter 4. A subject, which is of interest for wave propagation in both fully and partially saturated porous media, is the dynamic interaction between pore fluid and solid. This is discussed in chapter 5. A dynamic permeability parameter is introduced. Experimental determination of the properties of the porous media, and the preparation of a partially saturated column are discussed in chapter 6. Moreover, an experimental determination of the dynamic permeability is presented. In chapter 7, finally, we discuss wave experiments, performed on saturated and partially saturated porous media. Two porous columns are used in the wave experiments. The first is a column with a lenght of 1.4 m and a diameter of 74 mm, made of sand grains in the range 0.3-0.6 mm, which are glued together by means of an epoxy resin. The other is a column of natural Bentheim sandstone with a length of 1.1 m and a diameter of 75 mm. Use has been made of a vertical shock tube with a length of approximately 8 m and an internal diameter of 77 mm. This means that there is a gap of approximately 1 - 1.5 mm between the the porous medium and the shock tube wall, to prevent any shear interaction.

The application of the shock tube technique has some advantages over other methods, like ultrasound experiments. First of all, a step loading of a one-dimensional plane wave is a well defined boundary condition in wave propagation experiments. Secondly, the amplitude of the incident pressure step may easily be varied over a wide range (0.5 - 5 bar), which allows, in principle, the study of nonlinear effects. The energy content of the incident wave may be varied, which is hardly possible for other experimental techniques. In this way, also strongly damped wave phenomena may be detected. Finally, by means of the incident shock wave it is possible to measure the propagation, damping and reflection properties of the porous system over a wide range of frequencies (10 Hz - 100 kHz).

The interpretation of wave experiments is based on linear, one-dimensional theory. This means that we ignore any lateral motion of the pore fluid and of the porous skeleton. We consider the wave phenomena of both longitudinal compressional waves, that were described independently by Biot (1956) and by de Josselin de Jong (1956), and we ignore any shear wave effects. Some remarks on the influence of the gap between the porous column and the shock tube, on wave propagation and damping in the porous media are made in appendix B.

1.2   Literature survey

General balance equations for mass, momentum and heat tranfer in multi-component, multi-phase porous systems have been discussed by Whitaker (1977, 1986) and Bear & Bachmat (1984, 1990). A theoretical description of wave propagation in saturated porous media was already available in 1956 by Biot and by de Josselin de Jong. They predicted the existence of two longitudinal (P) waves and one transverse (S) wave. For the first P-wave, the pore fluid and the porous material are compressed simultaneously, but for the second P-wave, the porous material relaxes, while the pore fluid is compressed. These two wave modes are therefore often denoted as the "in-phase" and the "out-of-phase" mode, respectively. However, it was not until 1980 that the first experimental observation of the second longitudinal wave was reported (Plona 1980). Since then, the Biot theory has been succesfully applied to various problems, such as fourth sound in a superfluid system (Johnson 1980), fluid diffusion through elastic porous media (Chandler 1981), and acoustic velocity dispersion and attenuation in ultrasound experiments (Hovem & Ingram 1979). Using a shock tube technique, wave experiments were performed on air-filled and water-saturated porous media (Van der Grinten, van Dongen & van der Kogel 1985). Quantitative information on wave speeds, pore pressure amplitudes and damping was ob-

tained. In later experiments, also strain amplitudes of the porous material were measured (Van der Grinten, van Dongen & van der Kogel 1987).

Soon, acoustical properties of fully liquid saturated and gassy porous media were observed to be significantly different. An extended literature survey on the acoustics of gas-bearing sediments has been given by Anderson & Hampton (1980). Later, the two phase Biot theory has been modified to allow for the presence of a third phase, i.e. the gas phase. Garg & Nayfeh (1986) and Berryman, Thigpen & Chin (1988) presented rather general models, applicable to a wide variety of gas volume fractions. Bedford & Stern (1983) described the effect of a small amount of gas bubbles on the propagation and damping of the two longitudinal waves, but they only took into account the thermal damping mechanism. It appears to be convenient to introduce a dynamic, i.e. frequency dependent, compressibility of the pore fluid. Experimental data on wave propagation in partially saturated porous media are scarce. They are given by Dontsov, Kuznetsov & Nakoryakov (1987), Sniekers, Smeulders, van Dongen & van der Kogel (1989) and Smeulders, De la Rosette & van Dongen (1992), who all used a shock tube technique.

A subject, which is of vital interest for the adequate interpretation of wave experiments in porous media, is the dynamic, i.e. frequency dependent, interaction between pore fluid and solid. This point was already mentioned by Zwikker & Kosten (1949) and Biot (1956). They derived analytical expressions for a cylindrical duct and a rectangular slit, and showed that their results may be generalized for an arbitrary porous medium. Other analytical work has been performed by Bedford, Costley & Stern (1984), who considered a porous material with cylindrical pores of random orientation. On a formal level, Lévy (1979), Auriault (1980) and Burridge & Keller (1981) derived a two-scale averaging procedure to describe the dynamical behaviour of a Newtonian fluid within a porous, elastic, medium. Auriault, Borne & Chambon (1985) were the first to present both numerical and experimental data for a schematized, periodic, porous medium. They compared their results to an asymptotic, high frequency, approximation. In 1987, Johnson, Koplik & Dashen described the dynamic permeability behaviour over the entire frequency range by a scaling function. It is shown that there is a transition from the low frequency behaviour, which is viscosity dominated, towards a high frequency behaviour, which is inertia dominated. Numerical calculations of the dynamic permeability for a variety of microstructures were presented by Sheng & Zhou (1988) and Yavari & Bedford (1990). Experimental data were obtained by Charlaix, Kushnick & Stokes (1988).

2 Continuum theory

2.1 Isotropic deformation

It is well known to soil mechanics engineering practice, that a soil under load does not respond by instantaneous deflection, but rather settles gradually. Such settlement is caused by a slow-rate adaptation of the soil to the load variation, and this so called consolidation process is described by the stress-strain relations of the fluid-solid system. A one-dimensional treatment of this behaviour was first presented by Terzaghi (1925). The general theory of the deformation of a porous elastic solid, containing a viscous compressible fluid, was established by Biot (1941, 1955). In the first paper the isotropic case is considered, whereas in the second the theory is generalized to anisotropic materials. Stress-strain relations are derived on the basis of energy considerations by applying and extending the classical theory of elasticity.

The elastic coefficients, determining the deformation properties of fluid-solid systems, are related to measurable quantities by Gassmann (1951), Biot & Willis (1957), Geertsma & Smit (1961), Brown & Korringa (1975), Korringa (1981), and Berryman (1981). In this section, we will introduce the isotropic stress-strain relations and corresponding elastic coefficients. In the next section, measurable quantities are presented and a linkage to the elastic coefficients is made. Finally we will show that the stress-strain relations may also be derived from continuity and constitutive considerations.

Considering a fluid-filled elastic skeleton with a statistical distribution of interconnected pores, the porosity is usually denoted by:

$$\phi_0 = \frac{V_\phi}{V_b}, \tag{2.1}$$

where V_ϕ is the volume of the pores contained in a sample of bulk volume V_b. It is understood that the term "porosity" refers to the effective porosity, thus including only the interconnected void spaces as opposed to those pores which are sealed off. In the following, the word "pore" will refer to the effective pores, while the sealed pores will be considered as part of the solid

volume V_s. The stress tensor in the porous material is:

$$\begin{pmatrix} \tau_{11} + \tau & \tau_{12} & \tau_{13} \\ \tau_{21} & \tau_{22} + \tau & \tau_{23} \\ \tau_{31} & \tau_{32} & \tau_{33} + \tau \end{pmatrix}, \qquad (2.2)$$

with the symmetry property $\tau_{ij} = \tau_{ji}$.

If we consider a cube of unit size of the bulk material, τ represents the total normal tension force applied to the fluid part of the faces of the cube. Denoting by p the pressure of the fluid in the pores we may write:

$$\tau = -\phi_0 p. \qquad (2.3)$$

The remaining components τ_{ij} of the stress tensor are the forces applied to that portion of the cube faces occupied by the solid. They are a result both of the fluid pressure p and the additional intergranular stresses σ_{ij}:

$$\tau_{ij} = -\sigma_{ij} - (1 - \phi_0)p\delta_{ij}, \qquad (2.4)$$

where the Kronecker symbol δ_{ij} is obviously introduced because the pore fluid cannot exert nor sustain any shear forces. We notice that the additional intergranular stresses σ_{ij} are defined negative in tension. They are called "additional" because they add up to the fluid pressure induced stresses in the solid (see equation 2.4).

In the entire fluid-solid system chemical reactions are assumed not to occur. The solid skeleton is considered to have compressibility and shearing rigidity, and the fluid may be compressible. The deformation of a unit cube is assumed to be completely reversible and elastically linear. Each volume element is described by its averaged displacement of the fluid $\mathbf{U}(\mathbf{r}, t)$ and of the solid parts $\mathbf{u}(\mathbf{r}, t)$. The strain components for the solid and the fluid, respectively, are:

$$e_{ij} = \frac{1}{2}\left(\frac{\partial u_j}{\partial x_i} + \frac{\partial u_i}{\partial x_j}\right) \qquad (2.5)$$

$$\varepsilon_{ij} = \frac{1}{2}\left(\frac{\partial U_j}{\partial x_i} + \frac{\partial U_i}{\partial x_j}\right). \qquad (2.6)$$

In the case of complete isotropy, the stress-strain relations for the solid and the fluid component respectively may be written (Biot 1955):

$$\tau_{ij} = 2Ge_{ij} + Ae_{kk}\delta_{ij} + Q\varepsilon_{kk}\delta_{ij} \qquad (2.7)$$

$$\tau = Qe_{kk} + R\varepsilon_{kk}, \qquad (2.8)$$

where summation over repeated indices is assumed. A, Q and R are generalized elastic coefficients which can be related to such measurable quantities

as the fluid bulk modulus K_f, the skeletal frame shear modulus G and to K_b and K_a, which are the jacketed and unjacketed bulk moduli of the skeletal frame respectively. These relations will be treated in the next section.

2.2 A survey of measurable quantities

In literature, several different approaches and corresponding notations are used to describe the deformation behaviour of a fluid-solid system. All relevant bulk moduli characterizing this porous medium deformation behaviour will now unambiguously be established by discussing some conventional soil mechanics measurement techniques. It is not our aim to present detailed derivations; relevant literature is being referred to. Skeletal frame bulk moduli are obtained by allowing the pore pressure p and the external pressure p_e to vary independently (Biot & Willis 1957). This may be achieved by enclosing a fluid-saturated specimen of the porous material in a thin impermeable jacket, and then subjecting it to an external fluid pressure p_e. To ensure constant internal fluid pressure, the inside of the jacket may be made to communicate with the atmosphere through a tube. Assuming a dry specimen exhibits the same properties as a fully saturated one, the conventional jacketed test is usually performed on a dry specimen. In the unjacketed compressibility test, on the other hand, a sample of the material is immersed and saturated in a fluid to which is applied a pressure $p_e = p$, and deformation measurements are made over a time scale long enough for pressure equilibrium establishment throughout the pores. Defining the differential pressure $p_d = p_e - p$, we may write:

$$
\begin{aligned}
\frac{1}{K_b} &= -\frac{1}{V_b}\left(\frac{\partial V_b}{\partial p_d}\right)_p \\
\frac{1}{K_a} &= -\frac{1}{V_b}\left(\frac{\partial V_b}{\partial p}\right)_{p_d} \\
\frac{1}{K_\phi} &= -\frac{1}{V_\phi}\left(\frac{\partial V_\phi}{\partial p}\right)_{p_d}
\end{aligned}
\tag{2.9}
$$

From these it is immediately obvious that $K_a = K_\phi$ if the solid part is homogeneous, because changing p with constant p_d means applying the same incremental pressure to the outer and inner pore surface, and in case of homogeneous bodies, whether or not isotropic, the application of such incremental pressure leads to a linear mapping which does not change the porosity ϕ_0.

We will now link these measurable bulk moduli to the generalized elastic coefficients in the stress-strain relations (2.7, 2.8). From complicated but

7

straightforward equilibrium considerations, based on the isotropic equations (2.7) and (2.8), the generalized Gassmann equations may be derived (Biot & Willis 1957):

$$A = \frac{(1-\phi_0)^2 K_a - (1-2\phi_0)K_b + \phi_0 K_b(\frac{K_a}{K_f} - \frac{K_a}{K_\phi})}{1 - \phi_0\frac{K_a}{K_\phi} - \frac{K_b}{K_a} + \phi_0\frac{K_a}{K_f}} - \frac{2}{3}G$$

$$Q = \frac{\phi_0 K_a(1 - \phi_0 - \frac{K_b}{K_a})}{1 - \phi_0\frac{K_a}{K_\phi} - \frac{K_b}{K_a} + \phi_0\frac{K_a}{K_f}} \tag{2.10}$$

$$R = \frac{\phi_0^2 K_a}{1 - \phi_0\frac{K_a}{K_\phi} - \frac{K_b}{K_a} + \phi_0\frac{K_a}{K_f}},$$

where we have defined the fluid bulk modulus $K_f^{-1} = \rho_f^{-1}(\partial\rho_f/\partial p)$, ρ_f being the fluid density. Confining ourselves from now on to the homogeneous case, equations (2.10) may be simplified somewhat:

$$A = \frac{(1-\phi_0)^2 K_a - (1-2\phi_0)K_b + \phi_0 K_b(\frac{K_a}{K_f} - 1)}{1 - \phi_0 - \frac{K_b}{K_a} + \phi_0\frac{K_a}{K_f}} - \frac{2}{3}G$$

$$Q = \frac{\phi_0 K_a(1 - \phi_0 - \frac{K_b}{K_a})}{1 - \phi_0 - \frac{K_b}{K_a} + \phi_0\frac{K_a}{K_f}} \tag{2.11}$$

$$R = \frac{\phi_0^2 K_a}{1 - \phi_0 - \frac{K_b}{K_a} + \phi_0\frac{K_a}{K_f}}$$

Obviously, in the homogeneous case we may also write $K_a = K_s$, where we have introduced the skeletal grain bulk modulus:

$$\frac{1}{K_s} = -\frac{1}{V_s}\left(\frac{\partial V_s}{\partial p}\right)_{p_d} \tag{2.12}$$

Next assuming the porous skeleton and the pore fluid to be much more compressible than the skeletal grains themselves ($K_f/K_s \ll 1$ and also $K_b/K_s \ll 1$), equations (2.11) may be rewritten:

$$A = \frac{(1-\phi_0)^2}{\phi_0}K_f + K_b - \frac{2}{3}G$$

$$Q = K_f(1 - \phi_0) \tag{2.13}$$

$$R = \phi_0 K_f$$

Another measurable quantity is discussed by Verruijt (1982). Considering a compression test on a saturated sample, with drainage being prevented by an impermeable membrane surrounding the sample, Skempton's coefficient B is defined to be the ratio of the pore pressure increment dp to the increment of external pressure dp_e:

$$B = \left(\frac{\partial p}{\partial p_e}\right)_{m_f},\qquad (2.14)$$

where the subscript m_f indicates that the fluid is not allowed to flow across the outer boundaries of the sample, so the contained fluid mass m_f is preserved. We may also define a corresponding undrained bulk modulus K^* (Brown & Korringa 1975):

$$\frac{1}{K^*} = -\frac{1}{V_b}\left(\frac{\partial V_b}{\partial p_e}\right)_{m_f}\qquad (2.15)$$

Both Skempton's coefficient and the undrained bulk modulus may be related to previously defined bulk moduli. We may write (Verruijt 1982):

$$B = \frac{1 - \frac{K_b}{K_a}}{\phi_0(\frac{K_b}{K_f} - \frac{K_b}{K_\phi}) + 1 - \frac{K_b}{K_a}}\qquad (2.16)$$

and correspondingly (Biot & Willis 1957, Brown & Korringa 1975):

$$K^* = \frac{K_a - K_b + \phi_0 K_b(\frac{K_a}{K_f} - \frac{K_a}{K_\phi})}{1 - \phi_0\frac{K_a}{K_\phi} - \frac{K_b}{K_a} + \phi_0\frac{K_a}{K_f}}\qquad (2.17)$$

2.3   Continuity and constitutive relations

We will now derive equations (2.7) and (2.8) by application of continuity and constitutive relations for the isotropic homogeneous case. In this section, we will make a strict distinction between quantities themselves and their infinitesimal variations. Quantities themselves will be zero-subscripted. So ρ_{f0} and ρ_{s0} denote fluid and solid density respectively. Skeletal grains are considered incompressible, and deformations of the fluid-solid system are assumed reversible and elastically linear. The linearized continuity equations then are:

$$\frac{\partial}{\partial t}(\phi\rho_f) + \phi_0\rho_{f0}\nabla.\mathbf{w} = 0\qquad (2.18)$$

$$\frac{\partial}{\partial t}[(1-\phi)\rho_s] + (1-\phi_0)\rho_{s0}\nabla.\mathbf{v} = 0,\qquad (2.19)$$

where we have defined the averaged velocities $\mathbf{w} = \frac{\partial \mathbf{U}}{\partial t}$ and $\mathbf{v} = \frac{\partial \mathbf{u}}{\partial t}$ of the fluid and solid parts of an arbitrary volume element. The corresponding constitutive relations are:

$$dp_s = 0 \tag{2.20}$$

$$\frac{1}{K_f} = \frac{1}{\rho_{f0}} \frac{\partial \rho_f}{\partial p} \tag{2.21}$$

From equations (2.19) and (2.20) a relation between porosity changes and skeletal deformation is found:

$$\frac{\partial \phi}{\partial t} = (1 - \phi_0) \nabla \cdot \mathbf{v} \tag{2.22}$$

Substitution of equations (2.21) and (2.22) into (2.18) yields:

$$-\phi_0 \frac{\partial p}{\partial t} = (1 - \phi_0) K_f \nabla \cdot \mathbf{v} + \phi_0 K_f \nabla \cdot \mathbf{w} \tag{2.23}$$

This equation is merely the time derivative of equation (2.8), substituting expressions (2.13) for the Q and R parameters and using the identities:

$$\frac{\partial e_{kk}}{\partial t} = \nabla \cdot \mathbf{v} \tag{2.24}$$

$$\frac{\partial \varepsilon_{kk}}{\partial t} = \nabla \cdot \mathbf{w} \tag{2.25}$$

Additional constitutive equations are needed to describe porous skeleton deformation behaviour. They are obtained from Hooke's law, giving the stress-strain relations in the case of small strains in isotropic bodies (Love 1944, p. 102):

$$-\sigma_{ij} = (K_b - \frac{2}{3}G)e_{kk}\delta_{ij} + 2Ge_{ij} \tag{2.26}$$

The factor $K_b - \frac{2}{3}G$ is often referred to as λ, whereas μ is frequently used as a different notation for G. λ and μ are known as Lamé's coefficients. Multiplicating equation (2.23) by the factor $(1 - \phi_0)/\phi_0$ and then adding it to the time derivative of equation (2.26), we find the resulting equation is the time derivative of equation (2.7). So equations (2.23) and (2.26) are the full equivalents of equations (2.7) and (2.8), describing the deformation behaviour of the solid-fluid system.

10

2.4 Momentum equations

Considering a rigid fluid-filled porous medium at low Reynolds numbers, pressure gradients ought to be balanced by viscous forces:

$$0 = -\frac{\partial p}{\partial x_j} - \frac{\eta \phi_0}{k_0} w_j, \qquad (2.27)$$

where η is the fluid viscosity and k_0 is the steady-state permeability. This expression is known as Darcy's law. In the case of oscillating fluid motion, Darcy's law obviously only holds in the low frequency limit. At higher frequencies unsteady terms have to be added:

$$\phi_0 \rho_f \frac{\partial w_j}{\partial t} + (\alpha_\infty - 1)\phi_0 \rho_f \frac{\partial w_j}{\partial t} = -\phi_0 \frac{\partial p}{\partial x_j} - b_0 w_j, \qquad (2.28)$$

where we have defined $b_0 = \eta \phi_0^2 / k_0$. Furthermore, $\alpha_\infty \geq 1$ is often referred to as the tortuosity parameter; a purely geometrical quantity independent of solid or fluid density. The first term on the left hand side of equation (2.28) is the inertia term, whereas the second term on the left hand side is the unsteady interaction term, originating from the pore fluid being accelerated in a narrowing-widening microstructural porous geometry. So the direction of acceleration on microscale may very well differ from the macroscopic acceleration direction. If this is not the case, considering a cylindrical duct for example, α_∞ equals 1, and therefore the degree of tortuosity is described by the factor $(\alpha_\infty - 1)$. In the high frequency limit, we find that the steady interaction term may be ignored to arrive at:

$$\alpha_\infty \phi_0 \rho_f \frac{\partial w_j}{\partial t} = -\phi_0 \frac{\partial p}{\partial x_j} \qquad (2.29)$$

Resuming, we find pressure gradients are either balanced by viscous forces (low frequency limit) or by inertia forces (high frequency limit). Therefore a rollover frequeny ω_c is discerned, when viscous forces are of equal magnitude as inertia forces. From equations (2.27) and (2.29) we may write:

$$\omega_c = \frac{\eta \phi_0}{k_0 \alpha_\infty \rho_f} \qquad (2.30)$$

The introduction of ω_c obviously offers the opportunity to define dimensionless frequencies, which will later prove to be of some convenience considering wave propagation and damping in porous media.

If next an arbitrary small motion of the porous solid material is allowed,

11

only minor modifications in the steady and unsteady interaction terms of equation (2.28) are required:

$$\phi_0 \rho_f \frac{\partial w_j}{\partial t} = -\phi_0 \frac{\partial p}{\partial x_j} + b_0(v_j - w_j) + (\alpha_\infty - 1)\phi_0 \rho_f \frac{\partial}{\partial t}(v_j - w_j) \quad (2.31)$$

For the fluid-saturated porous material as a whole we may subsequently write:

$$\phi_0 \rho_f \frac{\partial w_j}{\partial t} + (1 - \phi_0)\rho_s \frac{\partial v_j}{\partial t} = -\frac{\partial \sigma_{ij}}{\partial x_i} - \frac{\partial p}{\partial x_j}, \quad (2.32)$$

where σ_{ij} are the additional intergranular stresses, introduced in section 2.1. They are defined negative in tension. Subtracting equation (2.31) from (2.32) and rearranging terms we may finally write for the solid and fluid components respectively:

$$-\frac{\partial \sigma_{ij}}{\partial x_i} - (1 - \phi_0)\frac{\partial p}{\partial x_j} = \frac{\partial}{\partial t}(\rho_{11} v_j + \rho_{12} w_j) + b_0(v_j - w_j) \quad (2.33)$$

$$-\phi_0 \frac{\partial p}{\partial x_j} = \frac{\partial}{\partial t}(\rho_{12} v_j + \rho_{22} w_j) - b_0(v_j - w_j), \quad (2.34)$$

where we have defined the density terms:

$$\begin{aligned} \rho_{12} &= -(\alpha_\infty - 1)\phi_0 \rho_f \\ \rho_{11} &= (1 - \phi_0)\rho_s - \rho_{12} \\ \rho_{22} &= \phi_0 \rho_f - \rho_{12} \end{aligned} \quad (2.35)$$

The above equations (2.33, 2.34) are in exact analogy with those formulated by Biot (1956) and De Josselin de Jong (1956).

2.5 Axial symmetry

As experiments are performed on a porous column with lenght L_0 and radius r_0, cylindrical coordinates are obviously appropriate. In this section we will derive the dynamic and stress-strain equations describing the fluid-solid system. These equations will be averaged over the cross-sectional area of the porous sample. We assume plane wave propagation is described accurately by these averaged relations. We may write for the axial (z) direction:

$$-\frac{\partial \sigma_{zz}}{\partial z} - \frac{1}{r}\frac{\partial}{\partial r}(r\sigma_{rz}) - (1 - \phi_0)\frac{\partial p}{\partial z} = \frac{\partial}{\partial t}(\rho_{11} v_z + \rho_{12} w_z) + b_0(v_z - w_z) \quad (2.36)$$

$$-\phi_0 \frac{\partial p}{\partial z} = \frac{\partial}{\partial t}(\rho_{12} v_z + \rho_{22} w_z) - b_0(v_z - w_z), \quad (2.37)$$

12

where we have assumed axial symmetry. Now averaging over the cross-sectional area of the sample we find equation (2.37) remains unchanged whereas equation (2.36) may be rewritten:

$$-\frac{\partial \sigma_{zz}}{\partial z} - (1 - \phi_0)\frac{\partial p}{\partial z} = \frac{\partial}{\partial t}(\rho_{11}v_z + \rho_{12}w_z) + b_0(v_z - w_z), \qquad (2.38)$$

where we have assumed no shear interaction to take place between the tube wall and the sample, i.e. $\sigma_{rz} = 0$ at the sample wall. For the stress-strain relations we proceed in an identical way, writing them in cylindrical coordinates and applying the same cross-sectional averaging technique. From equations (2.26) and (2.23) we find:

$$-\frac{\partial \sigma_{zz}}{\partial t} = (K_b + \frac{4}{3}G)\frac{\partial v_z}{\partial z} + (K_b - \frac{2}{3}G)\frac{2v_c}{r_0} \qquad (2.39)$$

$$-\phi_0 \frac{\partial p}{\partial t} = (1 - \phi_0)K_f(\frac{\partial v_z}{\partial z} + \frac{2v_c}{r_0}) + \phi_0 K_f(\frac{\partial w_z}{\partial z} + \frac{2w_c}{r_0}), \qquad (2.40)$$

where we have introduced v_c and w_c as the lateral velocity of the skeletal material and the lateral fluid velocity at the wall, i.e. at radius $r = r_0$. The factor $K_b + \frac{4}{3}G$ is known as the "constrained modulus" K_p.

3 Computational results

3.1 Wave motion

We will now consider the dilatation waves, defined by the dynamic equations (2.37, 2.38) and the stress-strain relations (2.39, 2.40). All essential features are brought out by discussing the one-dimensional situation, i.e. by neglecting all lateral velocities. We will describe the propagation of a plane wave parallel with the XY-plane, and thus assume an $\exp i(\omega t - \kappa z)$ dependence for all relevant parameters. From equations (2.39) and (2.40) we find:

$$- i\omega \hat{\sigma}_{zz} = -i\kappa K_p \, \hat{v}_z \tag{3.1}$$

$$- i\omega \phi_0 \hat{p} = -i\kappa K_f \left[(1 - \phi_0)\hat{v}_z + \phi_0 \hat{w}_z \right] \tag{3.2}$$

Using these equations and introducing the inverse squared complex velocity $\zeta = \kappa^2/\omega^2$, we may subsequently eliminate $\hat{\sigma}_{zz}$ and $\hat{p}$ from the dynamic equations (2.37) and (2.38) to find the following set for $\hat{v}_z$ and $\hat{w}_z$:

$$\begin{array}{rcl} \hat{w}_z[\; -R\zeta + \rho_{22} - ib/\omega \;] & = & \hat{v}_z[\quad Q\zeta - \rho_{12} - ib/\omega \;] \\ \hat{w}_z[\quad Q\zeta - \rho_{12} - ib/\omega \;] & = & \hat{v}_z[\; -P\zeta + \rho_{11} - ib/\omega \;] \end{array} \tag{3.3}$$

Use has been made of the notation we introduced before: $R = \phi_0 K_f$, $Q = (1 - \phi_0)K_f$ and a newly introduced parameter $P = K_p + K_f \frac{(1-\phi_0)^2}{\phi_0}$. We notice that the previously used steady-state parameter b_0 has been replaced by $b(\omega)$, describing the frequency dependent interaction force between fluid and solid. At low frequencies, $b(\omega)$ will show a Stokes-flow behaviour, whereas at higher frequencies, when the viscous skin depth $\delta = \sqrt{2\eta/\omega\rho_f}$ decreases, inertial effects will become dominant. This effect was accounted for by Biot (1956), who modelled porous media as an ensemble of cylindrical ducts. In chapter 5 we will attempt to give a thorough description of this frequency dependent behaviour on the basis of the theory of Johnson, Koplik & Dashen (1987), and we will show $b(\omega)$ to be a function of the reduced frequency ω/ω_c. The resulting frequency dependence of $b(\omega)/b_0$ is given in figures 3.1. From the set (3.3) the dispersion relation is found:
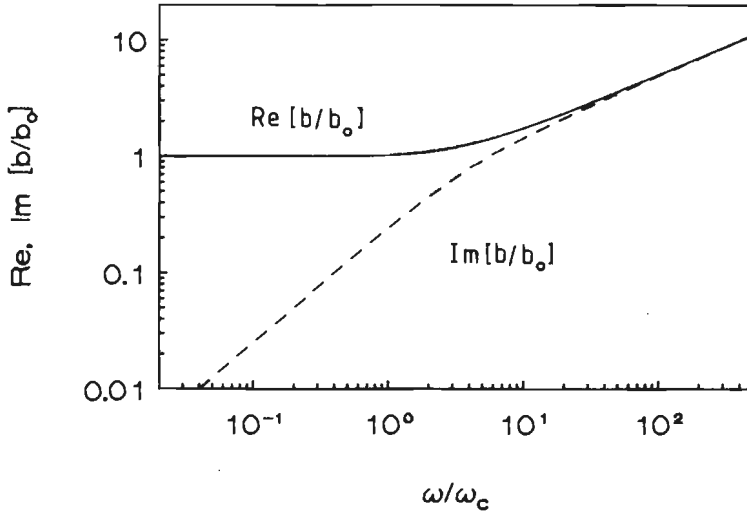
$$d_2\zeta^2 + d_1\zeta + d_0 = 0, \tag{3.4}$$

Figure 3.1: *Real and imaginary parts of the interaction term $b(\omega)/b_0$ as a function of the reduced angular frequency ω/ω_c.*

where we have used:

$$
\begin{aligned}
d_2 &= PR - Q^2 \\
d_1 &= -(P\rho_{22} + R\rho_{11} - 2Q\rho_{12}) + ib/\omega(P + R + 2Q) \qquad (3.5) \\
d_0 &= \rho_{11}\rho_{22} - \rho_{12}^2 - ib\rho/\omega
\end{aligned}
$$

Writing the dispersion relation in this way, we have introduced the bulk density $\rho = \rho_{11} + \rho_{22} + 2\rho_{12}$. Equation (3.4) has two complex roots $\zeta_1\ \zeta_2$, and there are therefore two damped dilatation waves, also called P-waves. The properties of both waves were illustrated by Biot (1956), who showed that the fluid and skeletal velocities are of the same sign for one root, and are of opposite sign for the other root. This means that there is one wave in which fluid and skeletal velocities are in phase, and another in which they are in opposite phase. In the same paper, it is also shown that the wave which propagates fastest, i.e. which has the highest phase velocity, has in-phase fluid and skeletal velocities, whereas the slower propagating wave has those velocities in opposite phase. As a matter of definition, the wave which propagates fastest will be denoted as the mode 1 wave, whereas the other one will be denoted the mode 2 wave. It is conceivable that mode 2 is damped more strongly than mode 1, because the out-of-phase character of mode 2 represents a highly effective dissipation mechanism. Dispersion plots of both phase velocity and damping are drawn in figures 3.2. The fluid-solid velocity ratios $\beta_j\ (j = 1,2)$ obviously follow from either one of the relations

15

in set (3.3). These ratios are depicted in figures 3.3. The in-phase behaviour
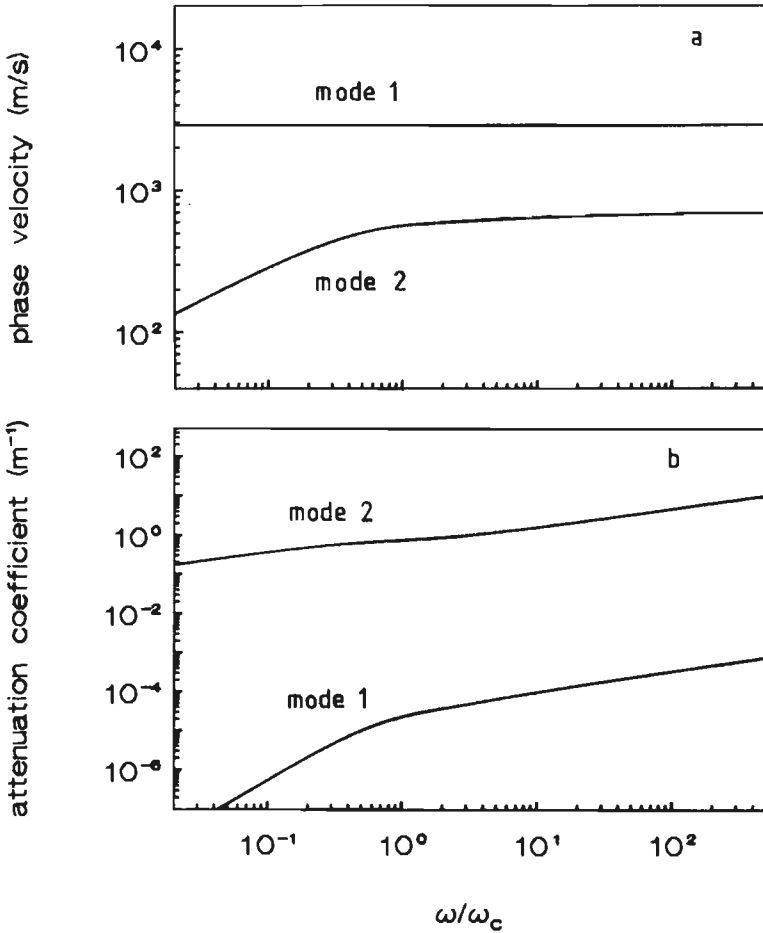
Figure 3.2: *Dispersion plots of phase velocity (a) and damping (b) of both wave modes. Parameter values are listed in table 3.1 at the end of this chapter.*

of the mode 1 wave is neatly illustrated by the ratio β_1, which is positive over the entire frequency range, whereas the mode 2 wave shows an overall out-of-phase behaviour. In the high frequency limit, the viscous skin depth δ tends to zero, and any dissipation may then be ignored, i.e. $b = 0$. The only coupling mechanism then left between fluid and solid movements is by the tortuosity parameter α_∞, which is an inertial coupling mechanism. In the low frequency limit, on the other hand, there is a viscous coupling mechanism between fluid and solid movements, represented by the b_0-coefficient or the corresponding permeability coefficient k_0. This is illustrated by combining
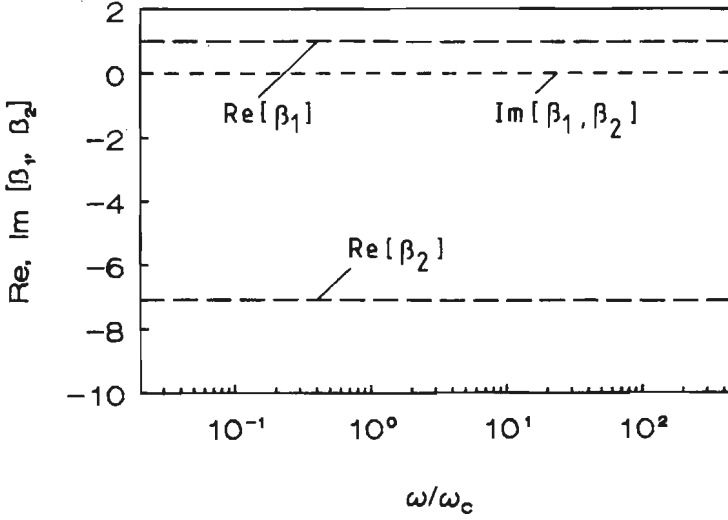
16

Figure 3.3: *fluid-solid velocity ratios β of both wave modes. Parameter values are listed in table 3.1 at the end of this chapter.*

the low frequency equation (2.27) with the fluid continuity relation (2.23) for a rigid porous medium. In this so-called stiff frame limit, we then find:

$$\frac{\partial p}{\partial t} = \frac{K_f k_0}{\eta \phi_0} \nabla^2 p, \qquad (3.6)$$

which is clearly a diffusion type equation. Thus, at low frequencies, the mode 2 wave corresponds to a diffusive type of propagation, governed by the hydraulic diffusivity coefficient $K_f k_0 / \eta \phi_0$, as was also previously shown (Bourbié 1987, p. 81).

In the case of high frequencies, we may ignore any viscosity effects. Combination of equations (2.29) and (2.23) for a rigid porous medium, yields the wave equation for the axial direction:

$$\frac{\partial^2 p}{\partial t^2} = \frac{\alpha_\infty \rho_f}{K_f} \frac{\partial^2 p}{\partial z^2} \qquad (3.7)$$

From this, we find that the phase velocity of the second dilatational wave equals the velocity of sound in the liquid c_l, modified by a factor $\sqrt{\alpha_\infty}$: $c_\alpha = c_l / \sqrt{\alpha_\infty}$. For the first dilatational wave, Van der Grinten (1987, p. 32) showed that a stiffer porous sample will increase the phase velocity. It will approache a limiting value. This so-called stiff frame velocity may be calculated from the dispersion relation (3.4), when the ratio K_f / K_p tends to zero:

$$c_1^2 = \frac{K_p}{(1-\phi_0)\rho_s + (1 - 1/\alpha_\infty)\phi_0 \rho_f} \qquad (3.8)$$

17

From this equation, it is easily seen that c_1 equals the longitudinal wave velocity $c_L = \sqrt{K_p/\rho_s}$, when $\phi_0 = 0$ (solid material).

For an elastic porous medium, generally, the phase velocities of both wave modes are found to be a function of the constrained modulus K_p. Both mode 1 and 2 phase velocities are depicted in figures 3.4a and 3.4b as a function of the constrained modulus K_p.

3.2   Step wave propagation

The porous column is submitted to an incident pressure step wave $\hat{p}_{in}$. Reflection and transmission phenomena are calculated by means of straightforward Fourier decomposition, as described by Van der Grinten, van Dongen & van der Kogel (1987). The incident wave partially reflects, denoted by $\hat{p}_r$, and partially transmits into the porous sample. Within the column, the initial step-wise pressure disturbance is distributed over the two wave modes. This process is obviously determined by boundary conditions, prescribing the values of pressure and stress in the sample at $z = 0$. These values are indicated by $\hat{p}_0$ and $\hat{\sigma}_0$, respectively. Using equations (3.1) and (3.2) we may now write ($j = 1, 2$):

$$\hat{\sigma}_{j0} = K_p \frac{\hat{v}_{j0}}{c_j} \tag{3.9}$$

$$\phi_0 \hat{p}_{j0} = K_f \left[(1 - \phi_0) \frac{\hat{v}_{j0}}{c_j} + \phi_0 \frac{\hat{w}_{j0}}{c_j} \right], \tag{3.10}$$

where we have defined the complex fluid velocity $c_j = \zeta_j^{-1/2}$. The stress boundary condition is:

$$\hat{\sigma}_0 = \hat{\sigma}_{10} + \hat{\sigma}_{20} = 0 \tag{3.11}$$

Using the relation $\hat{p}_0 = \hat{p}_{10} + \hat{p}_{20}$, and combining the above equations (3.9-3.11), we may compute the pressure distribution over both wave modes:

$$\frac{\hat{p}_{10}}{\hat{p}_0} = \frac{1 - \phi_0 + \phi_0 \beta_1}{\phi_0(\beta_1 - \beta_2)}$$

$$\frac{\hat{p}_{20}}{\hat{p}_0} = -\frac{1 - \phi_0 + \phi_0 \beta_2}{\phi_0(\beta_1 - \beta_2)}$$

From these relations it may be shown that, ignoring any viscosity effects, in the stiff frame limit the first wave will not cause any pore pressure increase: $\hat{p}_{10}/\hat{p}_0 \to 0$ and $\hat{p}_{20}/\hat{p}_0 \to 1$. That is because in the non-viscous stiff frame limit $\beta_1 \to -\rho_{12}/\rho_{22}$ and $\beta_2 \to \infty$. This behaviour is depicted in figure 3.4c, showing the gradually diminishing participation of the first wave mode

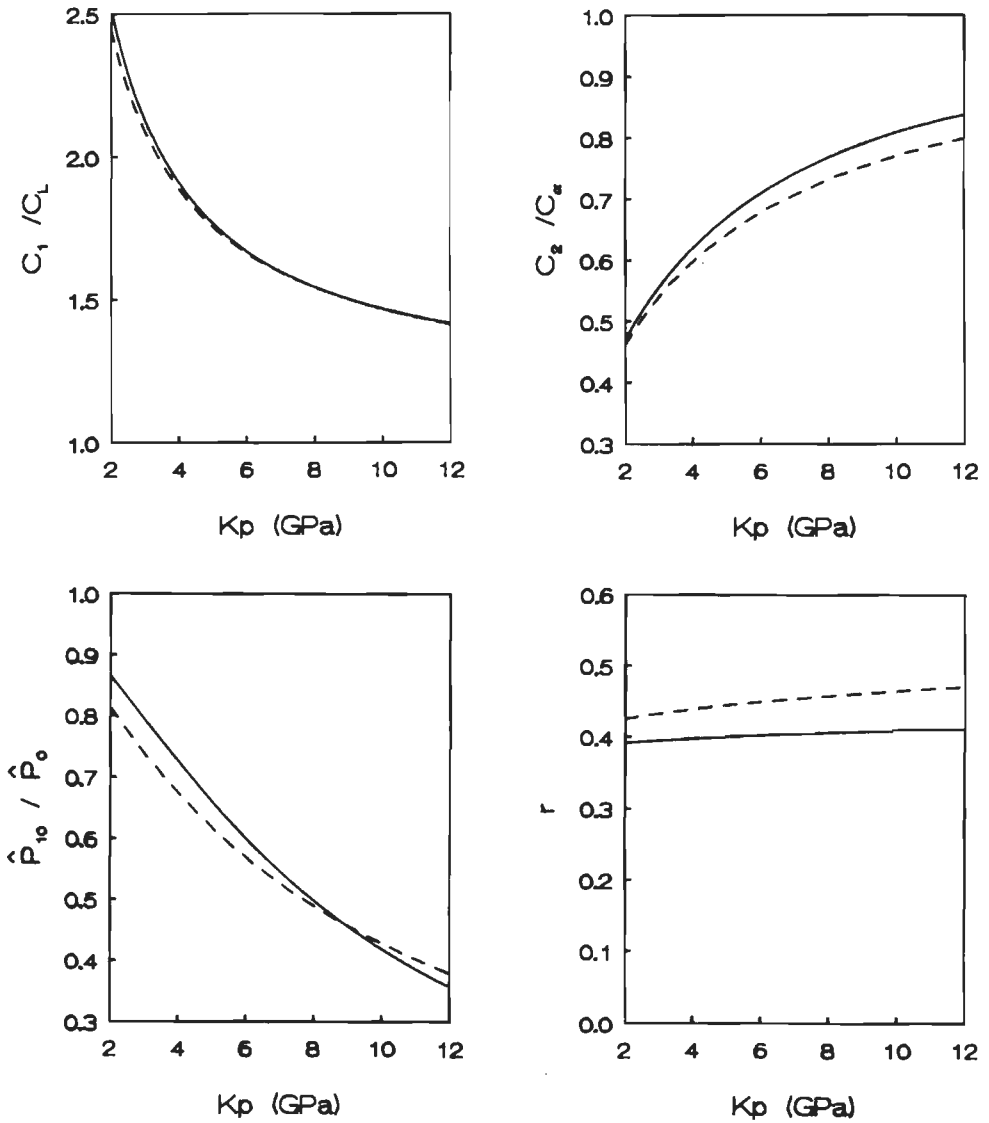Figure 3.4: *High frequency limits of reduced wave speeds (a, b), pore pressure amplitudes (c) and reflection coefficients (d) for $\alpha_\infty = 1$ (drawn lines) and $\alpha_\infty = 3$ (dashed lines). c_L is the longitudinal wave velocity and c_α is the modified speed of sound in the liquid. They are defined in the text. Parameter values are listed in table 3.1 at the end of this chapter.*

in the pore pressure built-up. Considering next the skeletal stresses, from equations (3.9 - 3.11) it may be found: $\hat{\sigma}_{10}/\hat{p}_0 = K_p K_f^{-1}(\beta_1 - \beta_2)^{-1}$ and for the second wave mode, of course (equation 3.11), the opposite is found. Having established the $z = 0$ values, we may now write at a distance z from the top of the porous sample:

$$\frac{\hat{p}(z,\omega)}{\hat{p}_0(\omega)} = \sum_{j=1}^{2} \frac{\hat{p}_{j0}(\omega)}{\hat{p}_0(\omega)} \exp(-i\kappa_j z) \qquad (3.12)$$

A similar relation holds for the stress wave propagation.

Again applying Fourier analysis, the above relation (3.12) may be illustrated in the time domain. Computations are performed for several z-values and depicted in figures 3.5. The same is done for the stress wave propagation. Considering the time dependent pressure behaviour at a fixed z-value, we notice the arrival of the first, fast, wave mode, followed by a plateau, which ends upon the arrival of the second, slow, wave mode. Then, further pressure increase towards its end value appears to be a much more gradual process, which is caused by the second wave mode having a diffusive type of propagation at low frequencies. The sudden increase towards a plateau value may also be recognized in the stress plot. This, again, represents the in-phase behaviour of the first mode. The out-of-phase behaviour of the second wave mode is illustrated by the fact that the strain plateau value is followed by a gradual decrease, whereas at the same time the pore pressure is still increasing. Comparing the computational results at several z-values, we notice the first wave mode retains its step-like character, whereas damping clearly changes the features of the second wave mode.

3.3   Wave reflection

As the incident step-like pressure disturbance is not fully transmitted into the porous column, we will now consider the $\hat{p}_0/\hat{p}_{in}$-ratio, which is known as the transmission coefficient. As shown in figure 7.1, the column is surrounded by a liquid filled gap of some millimeters width. In the cross section of the shock tube at $z = 0$, the surface fraction of the porous column is A and the gap surface fraction is $1 - A$. We may now consider the continuity requirement for the velocities at $z = 0$:

$$\hat{w}_{in} - \hat{w}_r = A[(1 - \phi_0)\hat{v}_0 + \phi_0\hat{w}_0] + (1 - A)\hat{w}_{g0}, \qquad (3.13)$$

where we have introduced the gap fluid velocity $\hat{w}_g$. Defining the acoustic impedance $Z_l = \rho_l c_l$, with c_l being the velocity of sound in the liquid above
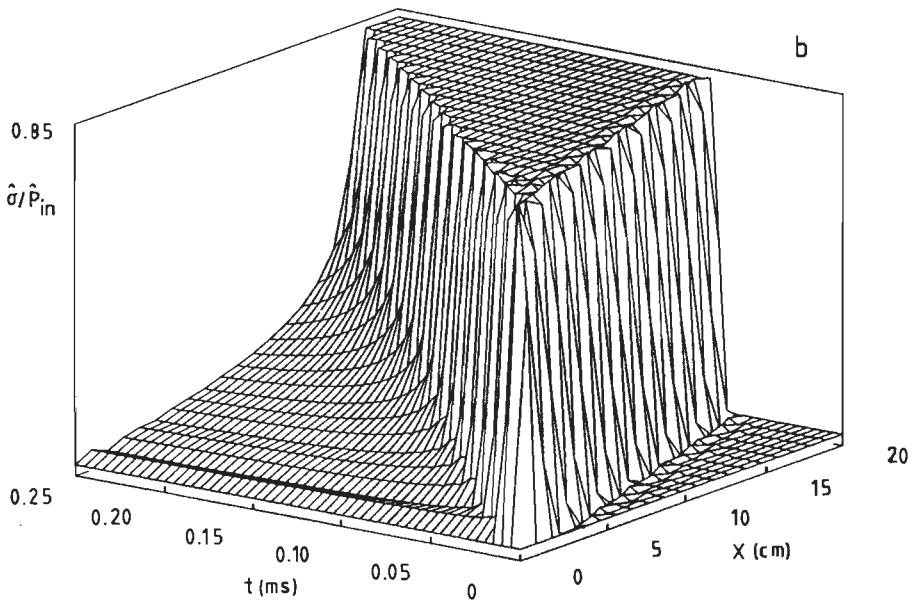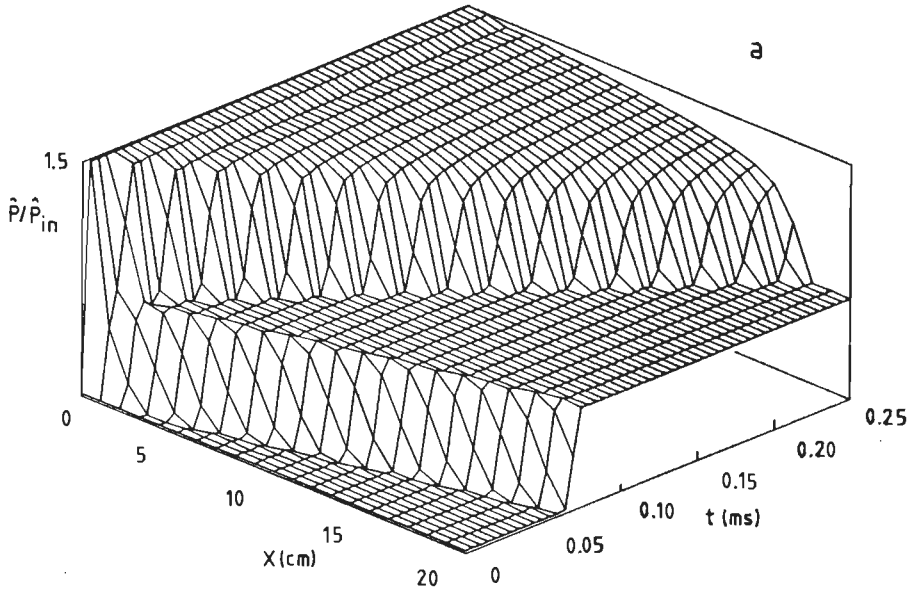
Figure 3.5: *Computed pore pressure (a) and skeletal stress (b) for a step-wise pore pressure disturbance at the top of a fluid-saturated porous medium. Parameter values are listed in table 3.1 at the end of this chapter.*

and surrounding the column, the above continuity relation may be rewritten:

$$\hat{p}_{in} - \hat{p}_r = A Z_l [(1 - \phi_0)\hat{v}_0 + \phi_0 \hat{w}_0] + (1 - A)\hat{p}_0, \qquad (3.14)$$

where we have used the pressure-velocity relations $Z_l = \hat{p}_{in}/\hat{w}_{in} = \hat{p}_r/\hat{w}_r = \hat{p}_0/\hat{w}_{g0}$. The above relation (3.14) may now be combined with the pressure boundary condition $\hat{p}_0 = \hat{p}_{in} + \hat{p}_r$ to yield:

$$\frac{\hat{p}_{in}}{\hat{p}_0} = (1 - \frac{1}{2}A) + \frac{1}{2}A Z_l \left[(1 - \phi_0)\frac{\hat{v}_0}{\hat{p}_0} + \phi_0 \frac{\hat{w}_0}{\hat{p}_0} \right], \qquad (3.15)$$

or after some algebraic manipulations:

$$\frac{\hat{p}_{in}}{\hat{p}_0} = (1 - \frac{1}{2}A) + \frac{1}{2}A Z_l \frac{\phi_0}{K_f} \left[c_1 \frac{\hat{p}_{10}}{\hat{p}_0} + c_2 \frac{\hat{p}_{20}}{\hat{p}_0} \right] \qquad (3.16)$$

The reflection coefficient r may now be calculated from the relation $r = \hat{p}_0/\hat{p}_{in} - 1$. In figure 3.4d, the reflection coefficient is drawn as a function of K_p.

porosity	ϕ_0	0.29	
constrained modulus	K_p	10.2	GPa
tortuosity	α_∞	2.7	
permeability	k_0	$90.91 \cdot 10^{-12}$	m^2
solid density	ρ_s	2650	kg/m^3
liquid density	ρ_l	1000	kg/m^3
liquid bulk modulus	K_l	2.2	GPa
viscosity of water	η	10^{-3}	Pa.s

Table 3.1   Parameter values used in computations.

4 Partially saturated pores

4.1 Preliminaries

It is not unlikely at all in soil mechanics engineering practice, to assume that porous media will hardly ever be fully liquid-saturated. One might envisage small gas remnants in oil saturated geological strata, or air bubbles trapped in marine sediments. In both cases, the saturating pore fluid consists of a liquid phase and a, usually small, amount of gas. In this chapter, the presence of gas bubbles in liquid saturated porous media will be accounted for by decomposing the fluid bulk modulus K_f:

$$\frac{1}{K_f} = \frac{s}{K_l} + \frac{1-s}{K_g}, \tag{4.1}$$

where we have denoted the liquid fraction in the pores by s and, obviously, the pore gasfraction by $1-s$. K_l is the liquid bulk modulus and K_g is an effective bulk modulus of the gas phase, which relates the averaged bubble volume V_g to a change in liquid pressure p_∞ far away from the bubble:

$$\frac{1}{K_g} = -\frac{1}{V_g}\frac{\partial V_g}{\partial p_\infty} \tag{4.2}$$

This approach is similar to the treatment of wave propagation in bubbly liquids by, among others, Van Wijngaarden (1970). As an illustration we will first consider the effective fluid velocity of sound, c_f, as a function of the amount of air added, without any porous material being involved. Writing the fluid density $\rho_f = (1-s)\rho_g + s\rho_l$, where by ρ_g we have denoted the gas density, from equation (4.1) we may write:

$$\frac{1}{c_f^2} = (1-s)\left[(1-s) + s\frac{\rho_l}{\rho_g}\right]\frac{1}{c_g^2} + s\left[s + (1-s)\frac{\rho_g}{\rho_l}\right]\frac{1}{c_l^2},$$

with c_l and c_g denoting the speed of sound in the liquid and in the gas, respectively. Resulting calculations are depicted in figure 4.1. We find that relatively small gasfractions seriously affect the fluid speed of sound, up to a degree where this speed of sound may even get lower than the speed of sound in air. It is only natural to assume that bubbles similarly control the
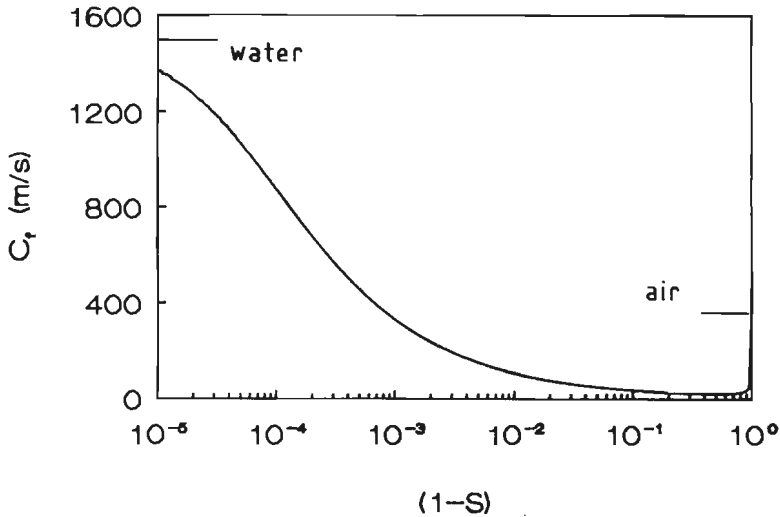
Figure 4.1: *Speed of sound in water as a function of the amount of air* $(1 - s)$ *added.*

acoustic properties of porous media. Any phenomenological description of wave propagation and damping in partially saturated porous media should also incorporate the dynamic gas bubble behaviour, which is omitted in the previous illustration, depicted in figure 4.1. Gas bubbles in liquid can vibrate and they have a fundamental resonance frequency. Damping mechanisms of vibrating gas bubbles have been reviewed by Van Wijngaarden (1972). We will now go over to the case of a liquid-saturated porous medium, containing vibrating gas bubbles.

4.2 General relations

It may be clear that damping of oscillating gas fractions in a porous medium is depending upon the shape and structure of the gas fractions under consideration. From visualization experiments presented in chapter 6, we have learned that the occuring gas fractions commonly occupy several pores and have a ramified shape, e.g. like alveoli in the human lungs. Yet, the general feature of the gasfractions is still spherical, with part of the internal gasvolume being occupied by skeletal material and fluid inclusions. Therefore, in the forthcoming sections, the analysis is based upon this assumption of sphericity. Our aim is to characterize gas bubble dynamics, relating the average gas bubble volume to a change in liquid pressure far away from the bubble. We will let the origin of coordinates be at the bubble centre, which

is at rest. The radius of the bubble at any time t is $R(t)$ and r is the radius to any point in the gas or in the liquid. For liquid motion with spherical symmetry the continuity equation becomes:

$$\frac{\partial w_r}{\partial r} + 2\frac{w_r}{r} = 0$$

Solving this equation we find the liquid velocity equals $\frac{dR}{dt}$ at $r = R$ and vanishes at infinity:

$$w_r = \frac{dR}{dt}\left(\frac{R}{r}\right)^2 \tag{4.3}$$

Considering the porous skeleton to be incompressible, the liquid equation may be written:

$$\alpha_\infty \rho_f \left(\frac{\partial w_r}{\partial t} + w_r\frac{\partial w_r}{\partial r}\right) = -\frac{\partial p}{\partial r} - \frac{b_0}{\phi_0}w_r \tag{4.4}$$

In order to determine the equation of motion for the bubble, equation (4.3) is substituted into equation (4.4), and equation (4.4) is subsequently integrated over the liquid from $r = R$ to infinity:

$$\alpha_\infty \rho_f \left\{R\frac{d^2R}{dt^2} + \frac{3}{2}\left(\frac{dR}{dt}\right)^2\right\} = -[p_\infty - p(R)] - \frac{b_0}{\phi_0}R\frac{dR}{dt} \tag{4.5}$$

This is the well-known Rayleigh-Plesset equation (Plesset 1949; Van Wijn-gaarden 1970) with an extra term added to take into account the Darcy interaction mechanism. In order to eliminate the liquid pressure $p(R)$ at the bubble surface, we will now consider the pressure jump across this bubble surface:

$$p(R) = p_g - \frac{4\eta}{R}\frac{dR}{dt} - \frac{2\sigma}{R}, \tag{4.6}$$

where p_g is the gas bubble pressure and σ is the surface tension. In this equation (4.6) it is assumed that the bubble radius is not affected by the presence of the porous material. For a detailed description of the dynamic behaviour of the air-liquid contact surface within a porous medium, it is important to notice that the dynamic contact angle ϕ_d may differ signifi-cantly from the static contact angle ϕ_s, depending on the capillary number $Ca = \eta\frac{\partial R}{\partial t}/\sigma$. This is treated by Boender, Chesters & van der Zanden (1991). Extra damping of the gas bubble oscillations may also be caused by the fact that the advancing contact angle is not necessarily equal to the receding contact angle, which is, in fact, a hysteresis effect. For both phenomena, the corresponding pressure jumps over the air-liquid contact surface are of the order σ/Λ, where Λ is an effective pore radius.

For the experimental conditions described in chapter 7, however, it is found that $\sigma/\Lambda \ll \hat{p}_\infty$. For porous media with low Λ-values, or for small fluid pressure amplitudes, on the other hand, it would be necessary though to take into account the effects mentioned above. This is, however, beyond the scope of the present study.

Furthermore, the gas bubble pressure is assumed to be uniform throughout the bubble, which implies that the inertia and the viscosity of the gas are negligible. The fluid surrounding the bubble provides the inertia for the bubble system as is seen in the first term on the left hand side of equation (4.5). The second term on the right hand side of the foregoing equation (4.6) is associated with the radial viscous stress τ_{rr} in the fluid, which, in general, may be written: $\tau_{rr} = -2\eta \partial w_r/\partial r + 2/3\eta \ div \ \mathbf{w}$ (Bird, Stewart & Lightfoot 1960, p. 89). As the fluid is regarded incompressible the divergence term cancels. The same approach was also used by Dontsov, Kuznetsov & Nakoryakov (1987) but they ignored surface tension effects. Now linearizing both equations (4.5) and (4.6) and substituting an $\exp(i\omega t)$ dependence for all relevant quantities we find:

$$\hat{p}_\infty = \hat{p}_g + \frac{2\sigma}{R_0^2}\hat{R} + \alpha_\infty \rho_f \omega^2 R_0 \hat{R} - i\omega \hat{R}\left(4\frac{\eta}{R_0} + \frac{b}{\phi_0}R_0\right), \qquad (4.7)$$

where linearized quantities are $\hat{}$ overscribed, and R_0 is the equilibrium bubble radius. Furthermore, the steady-state parameter b_0 has again been replaced by the frequency dependent interaction term $b(\omega)$. Aiming to eliminate the gas bubble pressure $\hat{p}_g$ from the above equation (4.7) we may write the polytropic relation:

$$\frac{\hat{p}_g}{p_{g0}} = -3n\frac{\hat{R}}{R_0}, \qquad (4.8)$$

where by n we have denoted the polytropic constant. Zero-subscribed quantities correspond to a fixed reference equilibrium state. Defining the thermal diffusivity a_g of the gas phase, we may assume bubble oscillation to occur isentropically when the thermal penetration depth $\delta_T = \sqrt{2a_g/\omega}$ is much smaller than any characteristic pore radius Λ. The polytropic constant n will then be equal to the specific heat ratio $\gamma = c_p/c_v$, with c_p and c_v being the specific heats at constant pressure and volume, respectively. When, on the other hand, the conductivity of heat is so complete that isothermal conditions prevail, n is equal to unity. This is the case when $\delta_T \gg \Lambda$. In the intermediate case, however, $\hat{p}_g/p_{g0}$ is no longer in phase with $\hat{R}/R_0$; it is this difference in phase that gives rise to a thermal damping mechanism, which is described by n being a complex valued quantity. This will be the subject of discussion in section (4.3).

Substitution of equation (4.8) into (4.7) yields:

$$\hat{p}_\infty = \left(\frac{2\sigma}{R_0} - 3np_{g0}\right)\frac{\hat{R}}{R_0} + \alpha_\infty\rho_f\omega^2 R_0\hat{R} - i\omega\hat{R}\left(4\frac{\eta}{R_0} + \frac{b}{\phi_0}R_0\right) \qquad (4.9)$$

We have now found a relation linking a change in gas bubble radius to a change in liquid pressure far away from the bubble. This gives us the opportunity to evaluate the importance of every term in equation (4.9), contributing to the damping of vibrating gas bubbles at resonance. This is done in section (4.5). In section (4.6) equation (4.9) is subsequently used to calculate the dynamic fluid bulk modulus over the frequency domain. At first, however, we need a more profound understanding of the thermal damping (section 4.3) and we will also describe the way compressibility effects of the pore fluid give rize to an acoustic damping mechanism (section 4.4).

4.3   Thermal damping

Thermal damping of oscillating gas bubbles, submerged in an infinitely extended fluid, has been investigated by Pfriem (1940), Spitzer (1943) and Devin (1959). These theories will now be modified and applied to the case of oscillating gas bubbles in a fluid-saturated porous medium. We will first describe the case of pulsating gas bubbles in a fluid and then go over to the case of pulsating gas bubbles in a porous system.

4.3.1   Pulsating gas bubbles in a fluid

As before we define a spherical coordinate system originating at the centre of the bubble. The bubble, which is in an alternating pressure field p_∞, cannot be in equilibrium with this oscillating pressure but by pulsating itself. We will now consider a cycle of vibration of the bubble. As the bubble is compressed its temperature T rizes; when the rise of the temperature is appreciable, heat conduction becomes important and the bubble tends to cool off even before the expansion has started. When maximum compression is reached the temperature will already be decreasing as heat flows from the bubble into the surrounding fluid. It is obvious that in this case maximum temperature will be reached somewhat before maximum compression is established. Therefore the temperature of the bubble at a given volume will be somewhat greater during the compression part of a cycle than during the expansion part. Since there is a direct relation between volume and pressure of the gas bubble, at a given volume the pressure exerted on the

bubble during the compression will be greater than the corresponding pressure during the expansion. Hence more energy is required to compress the bubble than is regained in the subsequent expansion. The work done by the bubble during one cycle of its vibration is negative and represents a net flow of heat ΔQ (per unit mass of the gas phase) into the surrounding fluid. The process must obey the conservation of energy principle as stated in the first law of thermodynamics. When the gas is considered ideal we may write:

$$\frac{dQ}{dt} = c_p \frac{dT}{dt} - v_g \frac{dp_g}{dt}, \tag{4.10}$$

where c_p is the specific heat at constant pressure and v_g is the reciprocal gas density. The rate of heat accumulation is proportional to the divergence of the temperature gradient:

$$\rho_g \frac{dQ}{dt} = \lambda_g \nabla^2 T, \tag{4.11}$$

where λ_g is the thermal conductivity of the gas phase. In the previous equation we have considered the heat flow a result of conduction alone. This is because convection is unimportant, as the time factor for establishment of this process is considerably larger than the time taken for a half-cycle vibration of the bubble. Now combining both foregoing equations we find:

$$\frac{\partial(rT)}{\partial t} = a_g \frac{\partial^2(rT)}{\partial r^2} + \frac{r}{\rho_g c_p} \frac{dp_g}{dt}, \tag{4.12}$$

where, as before, a_g is the thermal diffusivity of the gas phase. The oscillations in the pressure, volume and temperature of the gas in the bubble are assumed small. Consequently we may write a linearized relation from equation (4.12) assuming an $\exp(i\omega t)$ dependence for all relevant quantities:

$$i\omega(r\hat{T}) = a_g \frac{\partial^2(r\hat{T})}{\partial r^2} + i\omega \frac{r}{\rho_{g0} c_p} \hat{p}_g, \tag{4.13}$$

where, again, zero-subscribed quantities represent the equilibrium state and small deviations are ˆ overscribed. A solution of this differential equation must satisfy the boundary conditions. At the centre of the bubble the change in temperature $\hat{T}$ must be finite and it must be zero at the bubble surface. The solution of equation (4.13) thus becomes:

$$r\hat{T} = \frac{R_0 \hat{p}_g}{c_p \rho_{g0}} \left[\frac{r}{R_0} - \frac{\sinh(\psi r)}{\sinh(\psi R_0)} \right], \tag{4.14}$$

where $\psi = (1+i)\sqrt{\omega/2a_g}$, with the dimension of reciprocal length. This relation was also found by Devin (1959). The temperature field within the gas

bubble is now known. Yet, we still need to determine the relation between a change in bubble radius $\hat{R}$ (or correspondingly a change in bubble volume $\hat{V}_g$) and a change in gas bubble pressure $\hat{p}_g$. We will therefore consider the total gas volume as the sum of all concentric shells with radius r and thickness dr. For each shell the temperature is known according to relation (4.14) and consequently also the internal energy $d\hat{E} = \rho_{g0} c_v \hat{T} 4\pi r^2 dr$. (The reason for considering the internal energy will become apparent). Subsequent substitution of equation (4.14) and integration over the bubble volume yields:

$$\hat{E} = \frac{4\pi}{\gamma} R_0 \hat{p}_g \left[\frac{1}{3} R_0^2 + \frac{1}{\psi^2} - \frac{R_0}{\psi} \coth(\psi R_0) \right] \tag{4.15}$$

This change in internal energy must obey the first law of thermodynamics, which is now written in the form:

$$i\omega \hat{E} = \hat{q} - i\omega p_{g0} \hat{V}_g, \tag{4.16}$$

where a harmonic variation has been substituted for all relevant quantities. Furthermore, $\hat{q}$ denotes the heat flow rate (i.e. unit energy per unit time) through the fluid-gas interface. From this relation (4.16) it becomes obvious that a relation between the change in volume and the change in pressure of the gas bubble may be found once the heat flow rate $\hat{q}$ from the surrounding fluid into the gas bubble is known. As this heat flow rate is proportional to the temperature gradient at the bubble surface: $\hat{q} = 4\pi R_0^2 \lambda_g [\partial \hat{T}/\partial r]_{R_0}$, we may write after substitution of equation (4.14):

$$\hat{q} = 4\pi \lambda_g \frac{R_0 \hat{p}_g}{c_p \rho_{g0}} \left[1 - \psi R_0 \coth(\psi R_0) \right] \tag{4.17}$$

Now substitution of both equations (4.15) and (4.17) into (4.16) yields an expression, which may be written in the same form as the polytropic relation which we stated previously (4.8). Doing so, we find the polytropic constant n is given by the relation:

$$n = \gamma \left\{ 1 + \frac{3(\gamma - 1)}{\psi R_0} \left[\coth(\psi R_0) - \frac{1}{\psi R_0} \right] \right\}^{-1} \tag{4.18}$$

The consequences of this result will now be considered for the porous system.

4.3.2 Pulsating gas bubbles in a porous system

As we stated previously, a gas bubble with radius R_0 in a fluid-saturated porous medium will commonly occupy several pores: $R_0 > \Lambda$, where Λ is a characteristic pore radius. Therefore, heat transfer processes will take
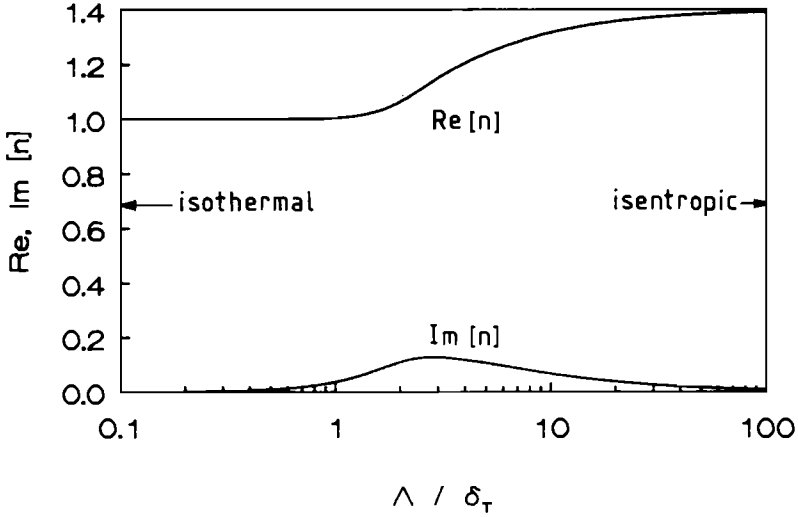
Figure 4.2: *Real and imaginary part of the polytropic constant as a function of the reciprocal, reduced, thermal penetration depth.*

place between the gas bubble and the surrounding porous structure rather than between the gas bubble and the surrounding fluid, as was the case in the previous section (4.3.1). The length scale related to the heat transfer processes and corresponding thermal damping mechanisms will be Λ rather than R_0. We have, consequently, presented in figure 4.2 both real and imaginary parts of the polytropic constant n as a function of Λ/δ_T, where $\delta_T = \sqrt{2a_g/\omega}$ is the thermal penetration depth. As expected, we find $n \to 1.0$ for small values of Λ/δ_T and $n \to 1.4$ for large values of Λ/δ_T. In between there is a transition zone with a non-zero imaginary part of n, which causes a phase difference between a change in pressure and a change in volume of the gas phase. This imaginary part of n is therefore responsible for the thermal damping mechanism. This is illustrated in figure 4.3, where we have plotted a diagram of the real part of the change in pressure of the gas bubble versus the real part of the change in volume of the gas bubble. The area enclosed by the compression and expansion curves represents the net loss of energy due to the heat conduction.
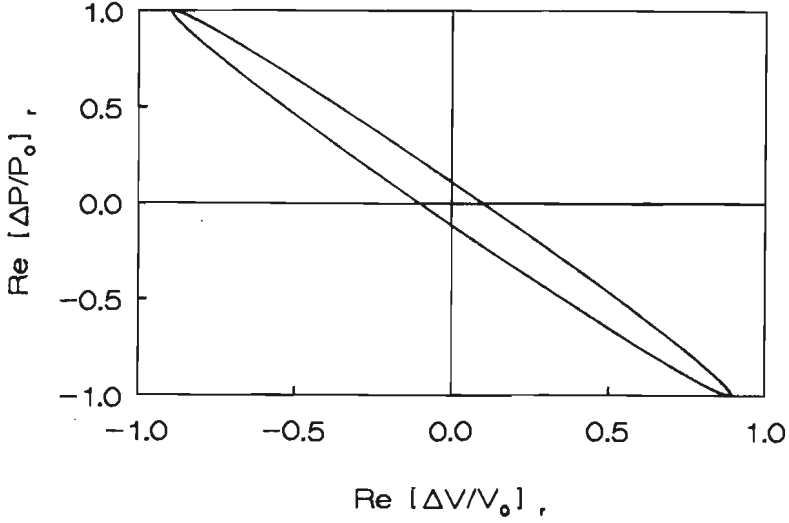
Figure 4.3: *Pressure-volume plot of the real part of the change in gas bubble pressure versus the real part of the change in gas bubble volume, at $\Lambda/\delta_T =$ 2.5. The index r denotes that the values are reduced by the maximum pressure amplitude $|\Delta p_g|/p_{g0}$.*

4.4 Acoustic damping

In this case the compressibility effect of the pore fluid is taken into account. The linearized continuity and momentum equations then become:

$$\frac{\partial \rho_f}{\partial t} + \rho_f \nabla.\mathbf{w} = 0$$

$$\alpha_\infty \rho_f \frac{\partial \mathbf{w}}{\partial t} = -\nabla p - \frac{b_0}{\phi_0}\mathbf{w}$$

Combining both foregoing equations we find:

$$\nabla^2 p - \frac{b_0}{\phi_0}\frac{1}{\rho_f c_l^2}\frac{\partial p}{\partial t} - \frac{\alpha_\infty}{c_l^2}\frac{\partial^2 p}{\partial t^2} = 0, \qquad (4.19)$$

where c_l is the speed of sound in liquid: $c_l^2 = \partial p/\partial \rho_f$. In spherical coordinates the above equation becomes:

$$\frac{\partial^2}{\partial r^2}(rp) - \frac{b_0}{\phi_0}\frac{1}{\rho_f c_l^2}\frac{\partial}{\partial t}(rp) - \frac{\alpha_\infty}{c_l^2}\frac{\partial^2}{\partial t^2}(rp) = 0 \qquad (4.20)$$

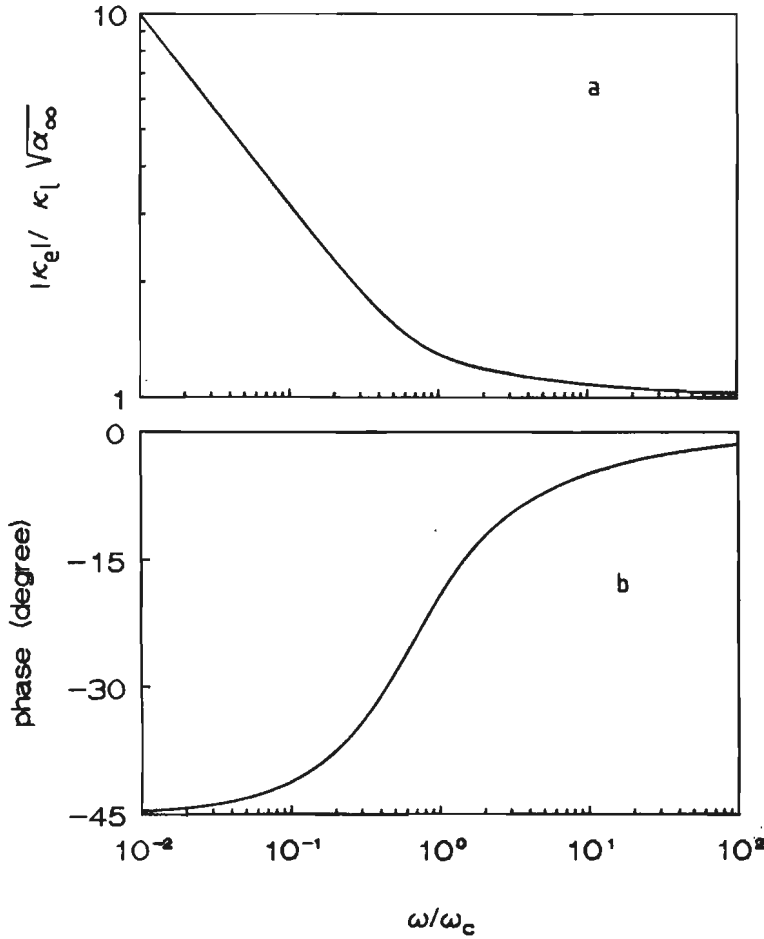After substitution of a harmonic pressure $p = \hat{p}\exp(i\omega t)$, the solution of

31

Figure 4.4: *Absolute (a) and phase values (b) of the effective wave number* κ_e *of the pore fluid.* κ_e *is reduced by the liquid wave number* κ_l *and the tortuosity parameter* α_∞.

the equation is given by a sperical pressure wave:

$$\hat{p} = \frac{R_0}{r}\hat{p}(R_0)e^{i\kappa_e(R_0-r)}, \qquad (4.21)$$

where we have defined an effective wave number $\kappa_e = \frac{\sqrt{\alpha_\infty}}{c_l}\sqrt{\omega^2 - i\omega\omega_c F}$, and F denotes the $b(\omega)/b_0$ ratio. This means that, at this stage, we have, as before, introduced the frequency dependent interaction term $b(\omega)$. A plot of the effective wave number κ_e/κ_l is shown in figure 4.4. Apparently, in the high frequency limit, the speed of sound is modified by a factor $\sqrt{\alpha_\infty}$, originating from the tortuosity of the porous medium. In the low frequency limit, viscosity effects are dominant, and we notice there is a $(\omega/\omega_c)^{-1/2}$

dependence of the absolute value of the wave number. Comparing this expression with the classical theory for an oscillating bubble in a compressible fluid (see e.g. Dowling & Ffowcs Williams 1982, p. 49), we find that the effect of the porous medium is represented by the effective wave number κ_e. For the velocity field we may write:

$$\hat{w} = \left(\frac{R_0}{r}\right)^2 \hat{w}(R_0)\frac{1 + i\kappa_e r}{1 + i\kappa_e R_0}e^{i\kappa_e(R_0-r)}, \tag{4.22}$$

where, obviously, $\hat{w}(R_0) = i\omega\hat{R}$ is the fluid velocity at the gas-fluid interface. Now integrating the momentum equation from R_0 to infinity we find:

$$\hat{p}_\infty = \hat{p}(R_0) + \frac{\alpha_\infty \rho_f R_0 \hat{R}}{1 + i\kappa_e R_0}(\omega^2 - i\omega\omega_c F) \tag{4.23}$$

For the pressure jump across the bubble surface we now write:

$$\hat{p}(R_0) = \hat{p}_g + \eta\left(2\frac{\partial \hat{w}_r}{\partial r} - \frac{2}{3}\nabla.\hat{\mathbf{w}}\right)_{R_0} + \frac{2\sigma\hat{R}}{R_0^2} \tag{4.24}$$

This yields:

$$\hat{p}(R_0) = \hat{p}_g - 4\eta i\omega \frac{\hat{R}}{R_0}\left(1 - \frac{\frac{1}{3}R_0^2\kappa_e^2}{1 + i\kappa_e R_0}\right) + \frac{2\sigma\hat{R}}{R_0^2} \tag{4.25}$$

For bubble radii up to a few millimeters the second term between the brackets in the above equation may be neglected for all frequencies. Subsequent combination of the above equations (4.23) and (4.25) and application of the polytropic relation leads to:

$$\hat{p}_\infty = \left(\frac{2\sigma}{R_0} - 3np_{g0} - 4\eta i\omega\right)\frac{\hat{R}}{R_0} + \frac{\alpha_\infty \rho_f R_0 \hat{R}}{1 + i\kappa_e R_0}(\omega^2 - i\omega\omega_c F) \tag{4.26}$$

We have now found a relation, which is essentially the same as the one we presented before (equation 4.9). It has only been modified by the acoustic damping, where it has been assumed that pulsating bubbles are radiating acoustical energy into the surrounding, infinitely extended, pore liquid.

4.5   Damping at resonance

In the case of undamped oscillating bubbles in a fluid-saturated porous medium, under isothermal conditions the resonant frequency is given by:

$$\omega_0 = \left[\frac{3p_{g0} - \frac{2\sigma}{R_0}}{\alpha\rho_f R_0^2}\right]^{1/2}$$
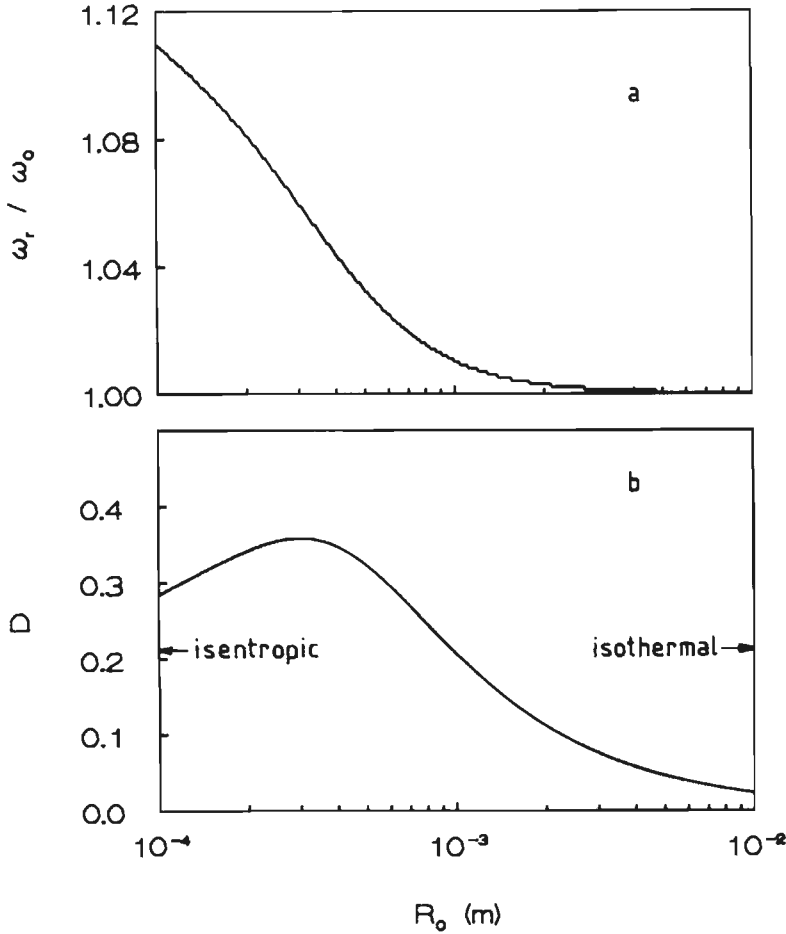
Figure 4.5: *Resonant frequency (a) and damping coefficient (b) of vibrating gas bubbles in a fluid-saturated porous medium. Only thermal damping is taken into consideration.*

When there is a transition from an adiabatic towards an isothermal condition, i.e. when thermal damping is taken into consideration, the oscillation of the bubble consists of a damped exponential sinusoidal vibration. The resonant frequency obviously becomes:

$$\omega_r = \mathcal{R}e \left[\frac{3np_{g0} - \frac{2\sigma}{R_0}}{\alpha\rho_f R_0^2} \right]^{1/2}, \qquad (4.27)$$

where n itself is a function of the angular frequency. Correspondingly, we may calculate the imaginary part ω_i, which is used to define the damping

34

constant D:

$$D = \frac{2\pi\omega_i}{\omega_r} \tag{4.28}$$

From equation (4.28) it is seen that D^{-1} is the number of cycles required for the amplitude of motion to reduce to e^{-1} of its original value. A numerical solution for ω_r and ω_i is found in an iterative manner. Results of computations for ω_r and D are presented in figure 4.5. We find that for bubble radii larger than 1 mm, the resonant frequency is given within one percent by the isothermal solution. That is because ω_r is directly proportional to R_0^{-1}. So, increasing R_0 values will yield lower resonant frequencies and a tendency towards the isothermal solution (see figure 4.2). It is interesting to note that the opposite is happening if there is no porous medium involved, and the length scale related to the heat transfer process is R_0 instead of Λ. Then, ω_r will remain proportional to R_0^{-1}, but the parameter R_0/δ_T, which replaces the parameter Λ/δ_T, will be proportional to $R_0^{1/2}$.

The damping reaches a maximum for bubble radii of approximately 0.3 mm, and tends to zero for smaller, and also for larger bubbles. So far, we have taken into account the thermal damping only. From the relation (4.26), however, we find that the total damping may be explained by losses, originating from four processes:

1. Darcy damping, due to the interaction forces between the fluid and the porous skeleton.

2. Thermal damping, caused by the annihilation of energy by heat flow between the gas in the bubble and the surrounding porous structure.

3. Sound radiation damping because of the compressibility effects of the pore fluid.

4. Viscous damping, due to viscous forces at the gas-liquid interface.

If we want to take into account all damping mechanisms mentioned above, we need to solve equation (4.26), where we have set $p_\infty = 0$, i.e. where we have removed the driving force. The equation is then, again, solved in an iterative manner. We may assume that the contributions of various dissipation mechanisms may be added to obtain the resulting damping coefficient (Van Wijngaarden 1972). A plot of the computed damping constants is given in figure 4.6. This plot may be compared directly to the ones presented by Devin (1959) and Van Wijngaarden (1972), who considered the case of oscillating gas bubbles in an infinitely extended fluid. In this case, Darcy damping is obviously not involved. In a fluid-saturated porous medium, however, we find that this Darcy damping is the most important damping mechanism for large pulsating gas bubbles. For small bubbles, both Darcy and thermal damping have to be taken into consideration. We also notice that neither the acoustic damping, nor the viscous damping, plays an
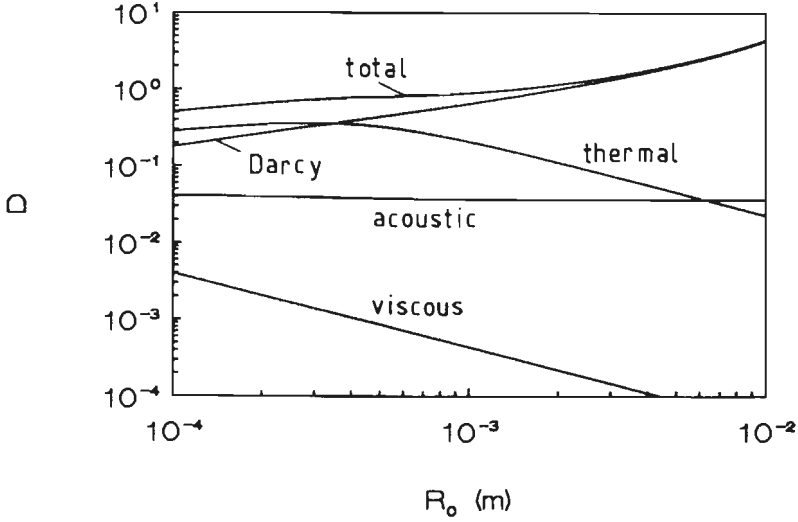
Figure 4.6: *Damping coefficients of vibrating gas bubbles in a fluid-saturated porous medium.*

important role over the entire bubble range.

4.6 Dynamic compressibility

In this section we will consider the effect of the previously discussed damping mechanisms over the entire frequency domain. From equations (4.2) and (4.26) we now find:

$$K_g = \left(np_{g0} - \frac{2}{3}\frac{\sigma}{R_0} \right) + \frac{4}{3}\eta i\omega - \frac{\frac{1}{3}\alpha_\infty \rho_f R_0^2}{1 + i\kappa_e R_0}(\omega^2 - i\omega\omega_c F) \qquad (4.29)$$

Ignoring surface tension, acoustic and viscous damping and taking $n \equiv 1$, we find the expression we reported before (Sniekers, Smeulders, van Dongen & van der Kogel 1989). We notice that the effective bulk modulus K_g of the gas phase becomes a complex valued quantity. The imaginary part of K_g causes a phase difference between a change in the gas volume $\hat{V}_g$ and a change in the exerted fluid pressure $\hat{p}_\infty$, which gives rise to an energy dissipation mechanism. We will therefore consider the contributions of the different damping mechanisms to the imaginary part of K_g. The contribution of the Darcy damping may be expressed by the ratio R_{Dar}:

$$R_{Dar} = \frac{1}{3}\alpha_\infty \rho_f R_0^2 \omega \omega_c \frac{\mathcal{R}e(F)}{\mathcal{I}m(K_g)}$$

The contribution of the thermal damping is expressed by the ratio R_{th}:

$$R_{th} = p_{g0} \frac{\mathcal{I}m(n)}{\mathcal{I}m(K_g)},$$

and the viscous contribution is, obviously, expressed by R_{visc}:

$$R_{visc} = \frac{4}{3} \frac{\eta\omega}{\mathcal{I}m(K_g)}$$

In all three cases, $\mathcal{I}m(K_g)$ is computed from equation (4.29). Results are depicted in figure 4.7. We find that $R_{visc} < 10^{-3}$ over the entire frequency
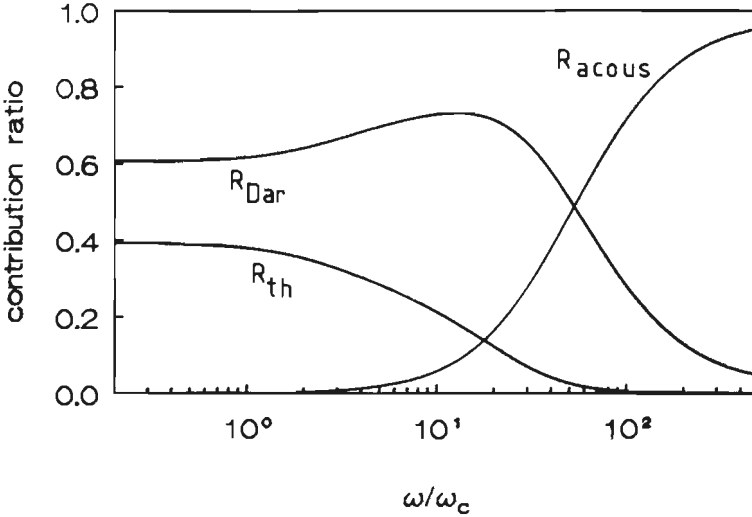

Figure 4.7: *Contribution ratios of different damping mechanisms. Computations are performed for a bubble radius of 1 mm.*

domain. Henceforth the viscous damping mechanism will be neglected. We also find that for low frequencies the damping of vibrating gas bubbles is entirely explained by both thermal and Darcy damping. However, this is no longer the case for high frequencies. From figure 4.7 it becomes clear that, in this case, the damping cannot be explained by thermal and Darcy damping alone. We also have to take into account the acoustic damping mechanism. For this acoustic damping mechanism we have not written an analytic expression for the contribution ratio R_{acous}, as we did for the other damping mechanisms. This is because from equation (4.29) it is seen that it is not possible to find one single term responsible for the acoustic damping. Furthermore, we find that for high frequencies the thermal damping mechanism may be ignored. That is because in this case gas bubbles are pulsating
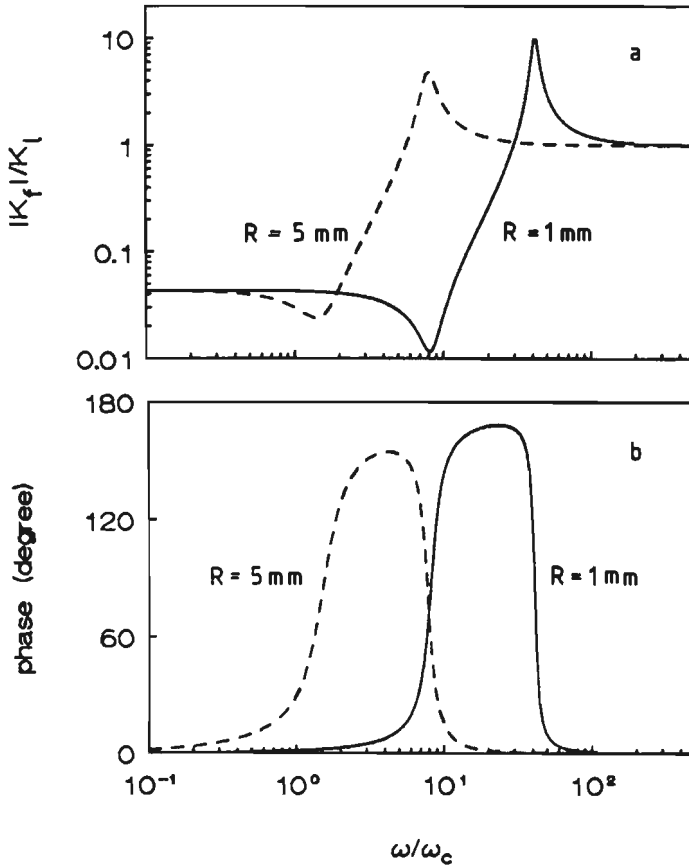
37

Figure 4.8: *Frequency dependent absolute values (a) and phase values (b) of the fluid bulk modulus in the isothermal case. Viscous and acoustic effects are neglected. Calculations are performed for a gasfraction of 0.1 % and bubble radii of 1 and 5 mm.*

isentropically, and there is, obviously, no thermal damping. Resuming, we find that the acoustic damping mechanism plays a very important role in the high frequency range. However, we have to notice that in our calculations it has been assumed that gas bubbles are freely radiating energy into the surrounded, infinitely extended, pore fluid. In our experiments this cannot be the case. Part of the radiated acoustic energy is reflected from the walls of the porous cylinder, and does not contribute to the energy dissipation of the system. Taking into account the acoustic damping in this way, will therefore overestimate its importance. In chapter 7, it will be shown from wave experiments that this is indeed the case. It is for this reason, that the forthcoming calculations will be performed omitting the acoustic damping

mechanism.

Combining equations (4.1) and (4.29), we are now able to compute the frequency dependent fluid bulk modulus. Results are depicted in figures 4.8. Calculations are performed for a gasfraction of 0.1 % and bubble radii of 1 and 5 mm. It may be clear from the previous considerations that we have performed these calculations taking into account the thermal and Darcy damping only. In this respect, our model is different from that of Bedford & Stern (1983), who took into account the thermal damping only. We find for both bubble radii that the general behaviour is identical. At low frequencies the dynamic bubble behaviour is of minor importance. The fluid bulk modulus is affected only by the extra steady-state compressibility of the gas bubbles: $K_g \rightarrow np_{g0} - \frac{2}{3}\frac{\sigma}{R_0}$. In the high frequency limit, on the other hand, the pore fluid acts as if there were no bubbles at all: $K_g \rightarrow -\infty$ and therefore $K_f \rightarrow K_l/s$, where s is usually close to (but less than) unity. In the intermediate transition region, relatively high absolute values of the bulk modulus occur; gas bubbles show an out-of-phase behaviour, i.e. increasing liquid pressure p_∞ causes gas bubbles to expand. This is neatly illustrated in the phase plot, where values of about π are reached in this case. The minimum absolute value of the bulk modulus occurs at the resonance frequency; gas bubbles are vibrating in phase with the exerted fluid pressure which results in a highly compressible fluid. From figure 4.8, it also becomes obvious that a change in bubble radius results in a frequency shift of the fluid bulk modulus (both absolute and phase values) due to a change in gas bubble resonant frequency.

4.7   Wave motion

In the previous section it was shown that the presence of gas bubbles in a fluid-saturated porous medium modifies the fluid bulk modulus K_f. Obviously, this will also change phase velocities and damping coefficients of both wave modes discussed in section 3.1. This is shown in figures 4.9. The results are somewhat different from those of Bedford & Stern (1983), because of different damping mechanisms. At low frequencies, we notice that the presence of a small amount of gas causes higher damping and lower phase velocities for both wave modes. Because of high energy dissipation, the damping of the second wave mode reaches its maximum when the gas bubbles are vibrating out-of-phase with respect to the exerted fluid pressure. In this case, the fluid becomes very stiff, which results in high mode 2 phase velocities. Mode 2 phase velocities may even attain higher values than the mode 1 phase velocities. In the high frequency limit, it becomes clear that an interchange of roles has taken place, both for the phase ve-
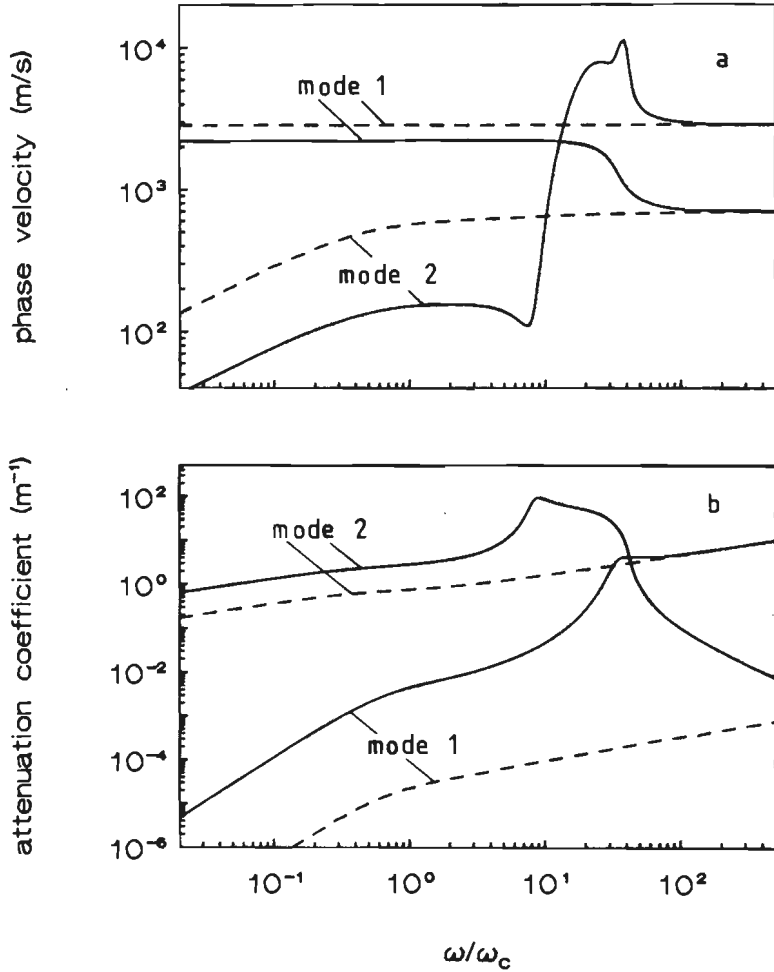
Figure 4.9: *Phase velocities (a) and attenuation coefficients (b) of compressional waves in a porous medium with water and equally sized air bubbles. Air volume fraction of the pores: 0.1 %; bubble radius: 1 mm. The dashed lines represent the fully saturated case.*

locities and the damping coefficients. The high frequency limit of mode 1 is the high frequency limit of the fully saturated mode 2 and vice versa. Summarizing, we find that the partially saturated porous medium acts as a frequency filter, with high atttenuation coefficients for one frequency range and low damping for another. This is illustrated again by the low mode 2 damping coefficients in the high frequency limit. The transmission phenomena, caused by an incident pressure step, have been calculated by means of a straightforward Fourier decomposition as described by Van der Grinten, van Dongen & van der Kogel (1987). The results are shown in the 3-D figure 4.10. As compared to the fully saturated case, which we discussed in chapter
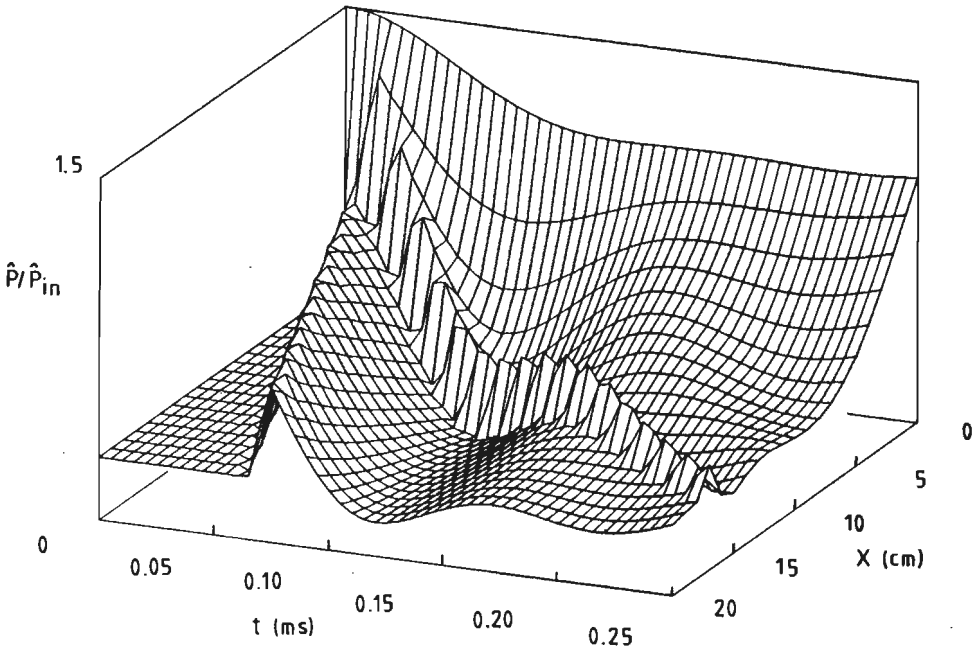
Figure 4.10: *Propagation of compressional waves in a partially saturated porous medium. Gasfraction: 0.1 %; bubble radius: 1 mm.*

3, we find that the two-step behaviour has completely disappeared. Instead, an oscillatory disturbance is seen to propagate in the porous material. At a longer time scale, this behaviour is depicted again in figure 4.11. In the fully saturated case, the gradual pressure increase, caused by the arrival of the second dilatational wave, commences from a certain offset value. Increasing

41

the gas fraction within the porous material, we notice that this offset value decreases. At a gasfraction of only 0.1 %, the offset value is already no longer visible (see figure 4.11). Furthermore, an oscillatory behaviour comes in, with higher frequencies involved when the gasfraction is increased. The gradual pressure increase is still observed, but it arrives later. The Fourier frequency spectrum of the oscillations, which we observed in the time domain (figure 4.11), is shown in figures 4.12 and 4.13. It consists of two frequency ranges, corresponding to the two Biot wave modes. The high frequency range corresponds to the second wave mode, which has low damping for high ω/ω_c values (see figure 4.9). The low frequency range corresponds to the first wave mode, which attains low damping coefficients in the low ω/ω_c region. We also notice that the Fourier spectrum is very sensitive to changes both in bubble radius and in gas fraction. This is depicted in both figures 4.12 and 4.13.
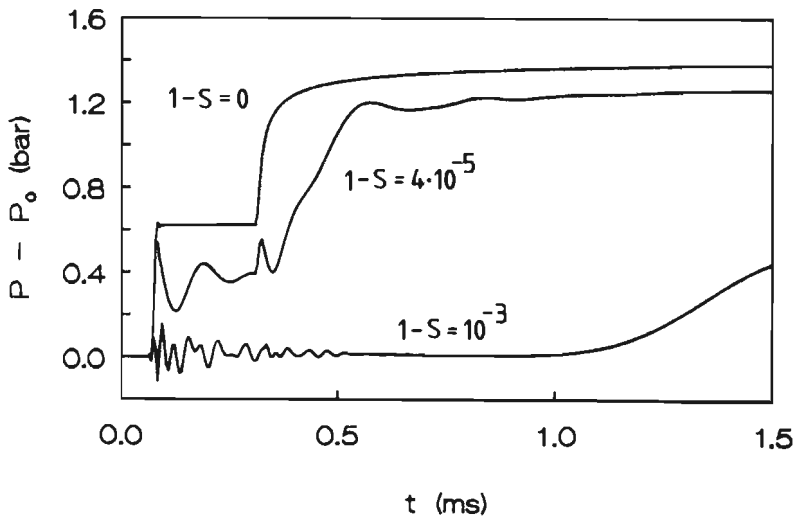
Figure 4.11: *Pressure development at increasing gasfraction at a depth of 22 cm. Bubble radius: 0.3 mm. p_0 is the atmospheric pressure. The incident pressure step $\hat{p}_{in}$ is 1.0 bar.*

Figure 4.12: *Fourier spectra at a depth of 22 cm. Two bubble radii have been considered for a gasfraction of 0.1 %. p_0 is the atmospheric pressure. The incident step $\hat{p}_{in}$ is 1.0 bar.*

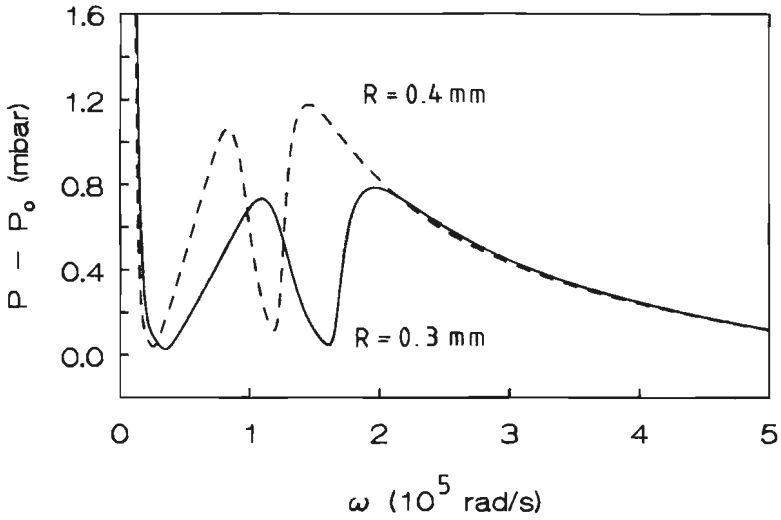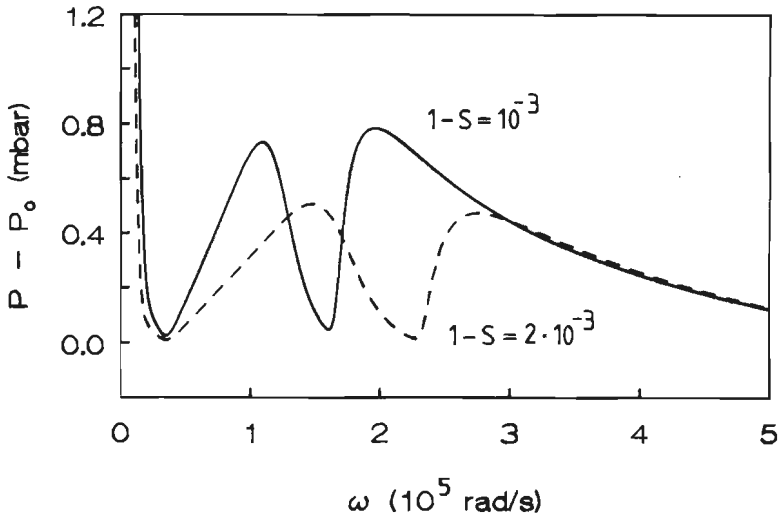Figure 4.13: *Fourier spectra at a depth of 22 cm. Two gasfractions have been considered for a bubble radius of 0.3 mm. p_0 is the atmospheric pressure. The incident step $\hat{p}_{in}$ is 1.0 bar.*

5   Dynamic permeability

5.1   Introduction

For many technological areas it is interesting to know how fluid flows through porous media. The dynamic permeability and tortuosity are important properties to describe the macroscopic flow through porous media, subjected to an oscillatory pressure gradient. It is important to notice that all important features are brought out considering a rigid porous medium. We will discuss this in section 5.4. Introducing an $\exp(i\omega t)$ dependence for the fluid pressure p and the macroscopic fluid velocity $\mathbf{w}$, the dynamic fluid behaviour may be characterized on a macroscopic scale by the ac permeability $k(\omega)$ or, alternatively, by the ac tortuosity $\alpha(\omega)$:

$$\frac{\eta \phi_0}{k(\omega)}\hat{\mathbf{w}} = -\nabla \hat{p} \tag{5.1}$$

$$i\omega \rho_f \alpha(\omega)\hat{\mathbf{w}} = -\nabla \hat{p} \tag{5.2}$$

In these two expressions, η is the fluid viscosity, ρ_f the fluid density and ϕ_0 the porosity. In the past few years, it has been the interest of many authors to express the macroscopic fluid behaviour in terms of averaged microscopic equations. Different authors have considered the steady-state permeability k_0 for stationary flow (Larson & Higdon 1988; Beasley & Torquato 1988; Rubinstein & Torquato 1989; Mei & Auriault 1991). The steady-state permeability is a real-valued quantity, defined by:

$$\lim_{\omega \to 0} k(\omega) = k_0 \tag{5.3}$$

For the dynamic permeability, however, less results are available. Lévy (1979), Auriault (1980) and Burridge & Keller (1981) derived a two-scale homogenization formalism to describe the dynamical behaviour of a Newtonian fluid within a porous, elastic, medium. Auriault, Borne & Chambon (1985) were the first to present both numerical and experimental data for a schematized, periodic, porous medium. They compared their results to an asymptotic, high frequency, approximation. In 1987, Johnson, Koplik & Dashen described the dynamic permeability behaviour over the entire frequency range by a scaling function. They argue that the reduced dynamic

permeability $k(\omega)/k_0$ must depend on a reduced frequency ω/ω_c, where ω_c is a rollover frequency from a viscosity dominated regime to an inertia dominated one:

$$\omega_c = \eta\phi_0/\rho_f k_0 \alpha_\infty, \qquad (5.4)$$

where α_∞ is the the tortuosity or added mass parameter, defined by:

$$\lim_{\omega \to \infty} \alpha(\omega) = \alpha_\infty \qquad (5.5)$$

The rollover frequency becomes apparent, equating the low frequency limit of (5.1) (i.e. for $k(\omega) \to k_0$) and the high frequency limit of (5.2) (i.e. for $\alpha(\omega) \to \alpha_\infty$). By analyzing the behaviour for high frequencies, Johnson *et al.* (1987) also found that $k(\omega)/k_0$ must be a function of yet another parameter

$$M = 8\alpha_\infty k_0/\phi_0\Lambda^2, \qquad (5.6)$$

where Λ is an independently measurable property of a porous material with the dimension of length. In the same paper the parameter M is suggested to be 1 for all porous media, at least approximately. All this was also briefly commented upon later (Johnson 1989). The assumption that there exists only one scaling function for all porous media was validated in later years, both numerically and experimentally. Numerical calculations of the dynamic permeability for a variety of microstructures were presented by Sheng & Zhou (1988) and Yavari & Bedford (1990). Experimental data were obtained by Charlaix, Kushnick & Stokes (1988).

In this chapter we will derive, from microstructure, the averaged dynamic permeability relations presented before by Lévy (1979), Auriault (1980) and Burridge & Keller (1981). Our relations are simplified somewhat because we have assumed the porous medium to be rigid. The unique macroscopic dynamic permeability $k(\omega)/k_0$, presented by Johnson *et al.* (1987), is subsequently expressed in terms of averaged microscopic relations. High frequency behaviour is studied.

Furthermore, we will present a way for numerical calculation of the constituents of the parameter M given in (5.6). Two different axisymmetrical pore geometries will be considered, and values of M for different pore geometries will be given.

5.2 Microstructural Approach

The microstructure of a random porous medium is generally characterized by a length scale a that is typical of the pore size. An extended statistical characterization in terms of various kinds of correlation functions has been

considered by several authors (Rubinstein & Torquato 1989; Bear & Bachmat 1990). Another scale of description is the macroscopic level, at which measurable continuous and differentiable quantities may be identified and boundary value problems can be stated and solved. Its length scale is called L. We now define ε as a/L. Considering a rigid fluid filled porous medium, we may write the linearized microscopic fluid equations:

$$\rho_f \frac{\partial \mathbf{u}}{\partial t} = -\nabla p + \eta \nabla^2 \mathbf{u} + (\eta + \eta') \nabla (\nabla . \mathbf{u}) \qquad (5.7)$$

$$\frac{1}{K_f} \frac{\partial p}{\partial t} = -\nabla . \mathbf{u}, \qquad (5.8)$$

where we have introduced the fluid velocity $\mathbf{u}$ at microscale. Furthermore, η' is the fluid dilatation viscosity and K_f is the fluid bulk modulus. Substitution of an $\exp(i\omega t)$ dependence for the fluid pressure p and fluid velocity $\mathbf{u}$ yields:

$$i\omega \rho_f \hat{\mathbf{u}} = -\nabla \hat{p} + \eta \nabla^2 \hat{\mathbf{u}} + (\eta + \eta') \nabla (\nabla . \hat{\mathbf{u}}) \qquad (5.9)$$

$$i\omega \frac{\hat{p}}{K_f} = -\nabla . \hat{\mathbf{u}} \qquad (5.10)$$

Equations (5.9) and (5.10) may be written in dimensionless form by introducing reference parameters $u_{ref} = \eta / \rho_f a$, $p_{ref} = L\eta^2 / \rho_f a^3$, $\omega_{ref} = \eta / \rho_f a^2$ and $t_{ref} = 1/\omega_{ref}$.

$$i\tilde{\omega} \tilde{\mathbf{u}} = -\frac{1}{\varepsilon} \tilde{\nabla} \tilde{p} + \tilde{\nabla}^2 \tilde{\mathbf{u}} + (1 + \frac{\eta'}{\eta}) \tilde{\nabla} (\tilde{\nabla} . \tilde{\mathbf{u}}) \qquad (5.11)$$

$$i\tilde{\omega} \tilde{p} = -\frac{1}{\varepsilon} \tilde{\nabla} . \tilde{\mathbf{u}}, \qquad (5.12)$$

where $\tilde{\nabla} = a\nabla$.

We may now apply the well-known technique of homogenization (Lévy 1979; Auriault 1980; Burridge & Keller 1981), involving the explicit recognition of two length scales in the problem by writing all quantities as a function of ε and the two spatial variables $\mathbf{x} = \mathbf{r}/L$ and $\mathbf{y} = \mathbf{r}/a$, and then expanding them as a perturbation series in ε. Furthermore, the gradient operator ∇ acts on both the x and y scales:

$$\tilde{\mathbf{u}} = \mathbf{u}_0(\mathbf{x}, \mathbf{y}) + \varepsilon \mathbf{u}_1(\mathbf{x}, \mathbf{y}) + ... \qquad (5.13)$$

$$\tilde{p} = p_0(\mathbf{x}, \mathbf{y}) + \varepsilon p_1(\mathbf{x}, \mathbf{y}) + ... \qquad (5.14)$$

$$\tilde{\nabla} = \varepsilon \nabla_x + \nabla_y \qquad (5.15)$$

Note that for convenience the ˜sign has been omitted in the right hand sides of the above equations. By now equating terms with equal powers of ε we obtain:

$$i\tilde{\omega}\mathbf{u}_0 = -\nabla_x p_0 - \nabla_y p_1 + \nabla_y^2 \mathbf{u}_0 \tag{5.16}$$

$$\nabla_y p_0 = 0 \tag{5.17}$$

$$i\tilde{\omega}p_0 = -\nabla_x.\mathbf{u}_0 - \nabla_y.\mathbf{u}_1 \tag{5.18}$$

$$\nabla_y.\mathbf{u}_0 = 0 \tag{5.19}$$

Similar equations were found by Lévy (1979) and Auriault (1980). Equation (5.17) indicates that the pressure p_0 is a function of the x spatial variable only and can therefore be identified as a measurable macroscopic quantity. Equation (5.19) indicates that the fluid may be regarded incompressible on the microscopic level (y-scale). As pressure and velocity are complex valued quantities, we may write from equation (5.16):

$$-i\tilde{\omega}\mathbf{u}_0^* = -\nabla_x p_0^* - \nabla_y p_1^* + \nabla_y^2 \mathbf{u}_0^* \tag{5.20}$$

The asterisk denotes complex conjungated quantities. Multiplication of equations (5.16) and (5.20) by $\mathbf{u}_0^*$ and $\mathbf{u}_0$, respectively, and subsequent addition yields:

$$-\nabla_y.(p_1\mathbf{u}_0^* + p_1^*\mathbf{u}_0) + \mathbf{u}_0^*.\nabla_y^2\mathbf{u}_0 + \mathbf{u}_0.\nabla_y^2\mathbf{u}_0^* = \mathbf{u}_0^*.\nabla_x p_0 + \mathbf{u}_0.\nabla_x p_0^* \tag{5.21}$$

In order to link this microscopic equation to its macroscopic equivalent we shall average it over the the y-variable. Aiming to define the average of any function g, defined for y in the fluid domain D_f, we will use the technique proposed by Burridge & Keller (1981). We consider a sphere $\Re$ of radius R and integrate g with respect to y over that part of D_f which is contained in $\Re$, and divide this integral by the volume of $\Re$. Finally, taking the limit of this ratio as $R \to \infty$ we call this limit $< g(x) >$. Applying this procedure to equation (5.21) we find:

$$< \mathbf{u}_0^*.\nabla_y^2\mathbf{u}_0 + \mathbf{u}_0.\nabla_y^2\mathbf{u}_0^* >=< \mathbf{u}_0^*.\nabla_x p_0 + \mathbf{u}_0.\nabla_x p_0^* > \; +$$

$$\lim_{R\to\infty} \frac{1}{\frac{4}{3}\pi R^3} \int_{S_{fR}} (p_1\mathbf{u}_0^* + p_1^*\mathbf{u}_0).n dy dy \tag{5.22}$$

The surface S_{fR} consists of two parts: the part of the pore surface within $\Re$: $(S_f)_R$, and the part of the surface of the sphere $\Re$ within D_f: $(S_R)_f$. Since the entire surface of the sphere is $4\pi R^2$, the integral over it is bounded by some constant times R^2. Divided by R^3 this integral is zero as $R \to \infty$. Therefore, the surface of integration in (5.22) may be replaced by $(S_f)_R$.

Considering this surface, we find any fluid velocity perpendicular to the pore surface $(S_f)_R$ to be zero, and we are left with:

$$< \mathbf{u}_0^* . \nabla_y^2 \mathbf{u}_0 + \mathbf{u}_0 . \nabla_y^2 \mathbf{u}_0^* > = < \mathbf{u}_0^* . \nabla_x p_0 + \mathbf{u}_0 . \nabla_x p_0^* > \qquad (5.23)$$

Defining the macroscopic fluid velocity $\tilde{\mathbf{w}} = < \tilde{\mathbf{u}}_0 >$, this equation may be rewritten:

$$< \tilde{\mathbf{u}}_0^* . \tilde{\nabla}_y^2 \tilde{\mathbf{u}}_0 + \tilde{\mathbf{u}}_0 . \tilde{\nabla}_y^2 \tilde{\mathbf{u}}_0^* > = \tilde{\mathbf{w}}^* . \tilde{\nabla}_x \tilde{p}_0 + \tilde{\mathbf{w}} . \tilde{\nabla}_x \tilde{p}_0^*, \qquad (5.24)$$

We have reintroduced the ˜ sign to focus attention to the dimensionless character of the quantities under consideration. The left hand side of the above equation (5.24) is the averaged microscopic fluid response to the applied macroscopic pressure gradients in the right hand side of equation (5.24). However, this linear (i.e. small amplitude) response of the pore fluid is usually described in terms of the macroscopic fluid velocity $\hat{\mathbf{w}} e^{i\omega t}$ and the dynamic, frequency dependent, tortuosity $\alpha(\omega)$. This relation was given by (5.2):

$$i\omega\alpha(\omega)\rho_f \hat{\mathbf{w}} = -\nabla_x \hat{p}_0, \qquad (5.25)$$

It is noted by comparing (5.1) and (5.2) that $\alpha(\omega)$ and $k(\omega)$ are not independent: $\alpha(\omega)/\alpha_\infty = -ik_0\omega_c/\omega k(\omega)$. In dimensionless form equation (5.25) becomes:

$$i\tilde{\omega}\alpha(\omega)\tilde{\mathbf{w}} = -\tilde{\nabla}_x \tilde{p}_0 \qquad (5.26)$$

As $\alpha(\omega)$ is a complex valued quantity we may write from (5.26):

$$- i\tilde{\omega}\alpha^*(\omega)\tilde{\mathbf{w}}^* = -\tilde{\nabla}_x \tilde{p}_0^* \qquad (5.27)$$

Multiplication of equations (5.26) and (5.27) by $\tilde{\mathbf{w}}^*$ and $\tilde{\mathbf{w}}$, respectively, and subsequent addition yields an energy equation at the macroscopic level:

$$2\mathcal{I}m[\alpha(\omega)]\tilde{\omega}|\tilde{\mathbf{w}}|^2 = \tilde{\mathbf{w}}^* . \tilde{\nabla}_x \tilde{p}_0 + \tilde{\mathbf{w}} . \tilde{\nabla}_x \tilde{p}_0^* \qquad (5.28)$$

In equation (5.24), the fluid response to the applied pressure gradients is written in terms of averaged microscopic velocities. In equation (5.28), on the other hand, the fluid response to the applied macroscopic pressure gradients is written in terms of the macroscopic tortuosity $\alpha(\omega)$. We may now equate both relations (5.24) and (5.28) to express $\alpha(\omega)$ in terms of ratios of averaged microscopic quantities:

$$\mathcal{I}m[\alpha(\omega)] = \frac{\langle \tilde{\mathbf{u}}_0^* . \tilde{\nabla}_y^2 \tilde{\mathbf{u}}_0 + \tilde{\mathbf{u}}_0 . \tilde{\nabla}_y^2 \tilde{\mathbf{u}}_0^* \rangle}{2\tilde{\omega}|\tilde{\mathbf{w}}|^2} \qquad (5.29)$$

We note that the right hand side of the above equation (5.29) is, in fact, only determined by the frequency and by the pore geometry because of the proportionality between all velocities involved. After some algebraic manipulations and reintroducing dimensions we may write:

$$\mathcal{I}m[\alpha(\omega)] = \frac{\eta}{2\omega\rho_f|\mathbf{w}|^2}\langle\frac{\partial}{\partial y_i}(u_{0j}^*\frac{\partial u_{0j}}{\partial y_i} + u_{0j}\frac{\partial u_{0j}^*}{\partial y_i}) - 2\frac{\partial u_{0j}^*}{\partial y_i}\frac{\partial u_{0j}}{\partial y_i}\rangle, \quad (5.30)$$

where summation over repeated indices is assumed. As it is obvious that we are considering harmonic flow behaviour, we have, for reason of convenience, omitted the ˆ sign for all velocities. Replacing in the previous derivation at the appropriate places (starting from equation 5.21) the addition by a subtraction, we may derive an expression for the real part of $\alpha(\omega)$ in a quite identical way:

$$\mathcal{R}e[\alpha(\omega)] = \frac{\langle|\tilde{\mathbf{u}}_0|^2\rangle}{|\tilde{\mathbf{w}}|^2} - \frac{\langle\tilde{\mathbf{u}}_0^*.\tilde{\nabla}_y^2\tilde{\mathbf{u}}_0 - \tilde{\mathbf{u}}_0.\tilde{\nabla}_y^2\tilde{\mathbf{u}}_0^*\rangle}{2i\tilde{\omega}|\tilde{\mathbf{w}}|^2}, \quad (5.31)$$

or alternatively:

$$\mathcal{R}e[\alpha(\omega)] = \frac{\langle|\mathbf{u}_0|^2\rangle}{|\mathbf{w}|^2} - \frac{\eta}{2i\omega\rho_f|\mathbf{w}|^2}\langle\frac{\partial}{\partial y_i}(u_{0j}^*\frac{\partial u_{0j}}{\partial y_i} - u_{0j}\frac{\partial u_{0j}^*}{\partial y_i})\rangle, \quad (5.32)$$

where, again, for reason of convenience, the ˆ sign has been omitted for all velocities.

5.3 High frequency behaviour

Having written the imaginary and real parts of $\alpha(\omega)$ in this way (equations (5.30) and (5.32)), we may now investigate the high frequency behaviour of $\alpha(\omega)$. In the limit of high frequencies, the viscous skin depth $\delta = \sqrt{2\eta/\omega\rho_f}$ eventually becomes much smaller than any characteristic pore size. Any vorticity, $\nabla \times \mathbf{u}$, generated at the pore walls decays to zero as one moves away from the pore walls into the bulk of the pore. Therefore, except for a boundary layer of thickness δ, the fluid motion is given by potential flow, $\mathbf{u} = -\nabla_y\psi$, for some ψ. In the forthcoming, we shall show that for an ideal fluid the quantity $\alpha(\omega)$ is a real valued quantity α_∞, independent of fluid properties. Then we shall relate, exactly, the corrections to this extreme high frequency limit α_∞ to the microscopic potential flow field for high frequencies. We note that since δ is arbitrarily small at high enough frequencies the walls of the pores appear to be flat in the boundary region. Therefore, introducing a boundary layer velocity $\mathbf{u}_{0\delta}$ at a distance δ from

the pore walls, the entire velocity field in the boundary layer is descibed by (Landau & Lifshitz 1959, p.91):

$$\mathbf{u}_0 = \mathbf{u}_{0\delta}[1 - e^{-ik\beta}] \tag{5.33}$$

(Also in this section, the ˆ sign is omitted). In this equation, β is a local coördinate, measured from the pore wall into the bulk of the pore, and $k = (1-i)/\delta$ is the shear wave number at frequency ω. By substituting (5.33) into (5.32), the second term in the right hand side of equation (5.32) vanishes and we readily arrive at ($\omega \to \infty$):

$$\mathcal{R}e[\alpha(\omega)] = \frac{\langle|\mathbf{u}_0|^2\rangle}{|\mathbf{w}|^2} \tag{5.34}$$

Obviously, in the extreme high frequency limit, the viscous skin depth δ tends to zero and we may write:

$$\lim_{\omega \to \infty} \mathcal{R}e[\alpha(\omega)] = \alpha_\infty = \frac{\langle|\mathbf{u}_p|^2\rangle}{|\mathbf{w}|^2}, \tag{5.35}$$

where $\mathbf{u}_p$ is the potential flow solution. In Appendix A, we show that the high frequency behaviour of $\mathcal{R}e[\alpha(\omega)]$, asymptotically approaching its extreme high frequency limit α_∞, may be described by rewriting equation (5.34) in terms of this extreme high frequency limit α_∞ and the viscous skin depth $\delta(\omega)$ ($\omega \to \infty$):

$$\mathcal{R}e[\alpha(\omega)] = \alpha_\infty[1 + \frac{1}{\Lambda_1}\delta(\omega)] \tag{5.36}$$

It is also shown in appendix A that Λ_1 has the dimension of length, and can be evaluated on the basis of steady potential flow theory:

$$\frac{2}{\Lambda_1} = \frac{[\frac{\partial}{\partial r}\int|\mathbf{u}_p|^2dV]_{\Delta\psi}}{\int|\mathbf{u}_p|^2dV} \tag{5.37}$$

In this equation, we have defined a flow potential difference $\Delta\psi$ between two arbitrary equipotential surfaces. Furthermore, $[\frac{\partial}{\partial r}G]_{\Delta\psi}$ denotes the derivative of some quantity G with respect to some outward virtual displacement r of the pore walls at constant $\Delta\psi$.

Next, we shall evaluate the asymptotic behaviour of the imaginary part $\mathcal{I}m[\alpha(\omega)]$ by combination of (5.30), (5.33) and (5.35) ($\omega \to \infty$):

$$\mathcal{I}m[\alpha(\omega)] = -\frac{\eta}{\omega\rho_f}\frac{\alpha_\infty}{\delta}\frac{\frac{1}{V_p}\int|\mathbf{u}_{pw}|^2dS}{\langle|\mathbf{u}_p|^2\rangle}, \tag{5.38}$$

50

where the integration is over the pore wall surface S, and V_p is the pore volume. Furthermore, $\mathbf{u}_{pw}$ denotes the potential flow velocity at the wall. Interpretating the averaging operation in the denominator of (5.38) we may write ($\omega \to \infty$):

$$\mathcal{I}m[\alpha(\omega)] = -\alpha_\infty \frac{\delta}{2} \frac{2}{\Lambda_2}, \qquad (5.39)$$

where the parameter Λ_2 has the dimension of length and is given by:

$$\frac{2}{\Lambda_2} = \frac{\int |\mathbf{u}_{pw}|^2 dS}{\int |\mathbf{u}_p|^2 dV_p} \qquad (5.40)$$

This expression (5.40) was derived earlier by Johnson *et al.* (1987), on the basis of energy flux and energy dissipation considerations. The integration in the numerator of (5.40) is over the pore wall surface S; that of the denominator is over the pore volume. Thus, $2/\Lambda_2$ is essentially the surface-to-pore volume ratio, in which each surface or volume element is weighted according to the local value of the field $\mathbf{u}_p$. The motivation for defining Λ_2 in this way becomes apparent considering a straightforward potential flow through a cylindrical duct with radius R. As $\mathbf{u}_p$ is the same everywhere in the duct, we easily find $\Lambda_2 = R$. The error in equation (5.39) is of $O(\delta^2)$ and thus equation (5.39) is satisfactorily accurate. Combination of (5.36) and (5.39) yields an expression for $\alpha(\omega)$ for higher frequencies with an error of $O(\delta^2)$ ($\omega \to \infty$):

$$\alpha(\omega) = \alpha_\infty [1 + \frac{\delta(\omega)}{\Lambda_1} - i\frac{\delta(\omega)}{\Lambda_2}] \qquad (5.41)$$

The parameters Λ_1 and Λ_2, however, are not independent. Following the same reasoning as Johnson *et al.* (1987), we have the further requirement that $\alpha(\omega)$ should satisfy a symmetry relation:

$$\alpha(-\omega) = \alpha^*(\omega) \qquad (5.42)$$

As we have $\delta(-\omega) = \mp i\delta(\omega)$ we readily find from equation (5.41):

$$\Lambda_1 = \Lambda_2 = \Lambda \qquad (5.43)$$

This modifies equation (5.41) to ($\omega \to \infty$):

$$\alpha(\omega) = \alpha_\infty [1 + (1 - i)\frac{\delta(\omega)}{\Lambda}] \qquad (5.44)$$

From equation (5.44) it becomes clear that the dynamic tortuosity $\alpha(\omega)/\alpha_\infty$ in the high frequency regime can be characterized by the parameter δ/Λ, or, alternatively, $\nu/\omega\Lambda^2$, where ν denotes the kinematic viscosity. Summarizing,

we may write that the dynamic tortuosity over the full frequency range is a function of at least two parameters:

$$\frac{\alpha(\omega)}{\alpha_\infty} = f\left(\frac{\omega}{\omega_c}, \frac{\nu}{\omega_c \Lambda^2}\right)$$

This, indeed, confirms the assumption by Johnson *et al.* (1987) that the dynamic permeability is a function of ω/ω_c and M. Furthermore, we have shown that the present results found for α_∞, Λ_1 and Λ_2 only contain real valued quantities that can be evaluated on the basis of steady potential flow theory. As the steady-state permeability k_0 may be computed from the Stokes flow problem, we are now able to investigate the parameter M. This will be treated in section 5.5 for axisymmetrical model pores of different geometries.

5.4   Relation to acoustics in deformable porous media

In this section we will consider the relevance of the results of this chapter to the acoustic properties of deformable porous media generally. The drag that the solid part of the porous medium exerts on the fluid part, is dominated by inertial effects in the strictly high frequency limit, and by viscous effects in the strictly low frequency limit. This drag is therefore characterized by the values for the tortuosity α_∞, and for the permeability k_0, respectively. In the Biot theory, this drag is described in terms of relative motion between fluid and solid. From relation (2.31), the equation of motion for the fluid constituent may be written:

$$i\omega \rho_f \hat{\mathbf{w}} = -i\omega \rho_f \left[\alpha(\omega) - 1\right] (\hat{\mathbf{w}} - \hat{\mathbf{v}}) - \nabla \hat{p}, \qquad (5.45)$$

where

$$\alpha(\omega) = \alpha_\infty - \frac{ib(\omega)}{\phi_0 \omega \rho_f} \qquad (5.46)$$

These relations were also found by Johnson & Plona (1982). The quantity $\alpha(\omega)$, appearing in (5.45), is independent of the elastic properties of both fluid and solid and is, in fact, identical with that defined in (5.2). This can be seen by considering the Biot equations in the limit that the skeletal frame moduli are much larger than the bulk modulus of the fluid, so that the fluid does not move ($\hat{\mathbf{v}} \equiv 0$); in this limit (5.45) reduces identically to (5.2). The implications are that the general properties of $\alpha(\omega)$, deduced in the previous sections, automatically apply to the acoustics of deformable porous media, via the Biot theory. The conventional approach has been to treat the pore
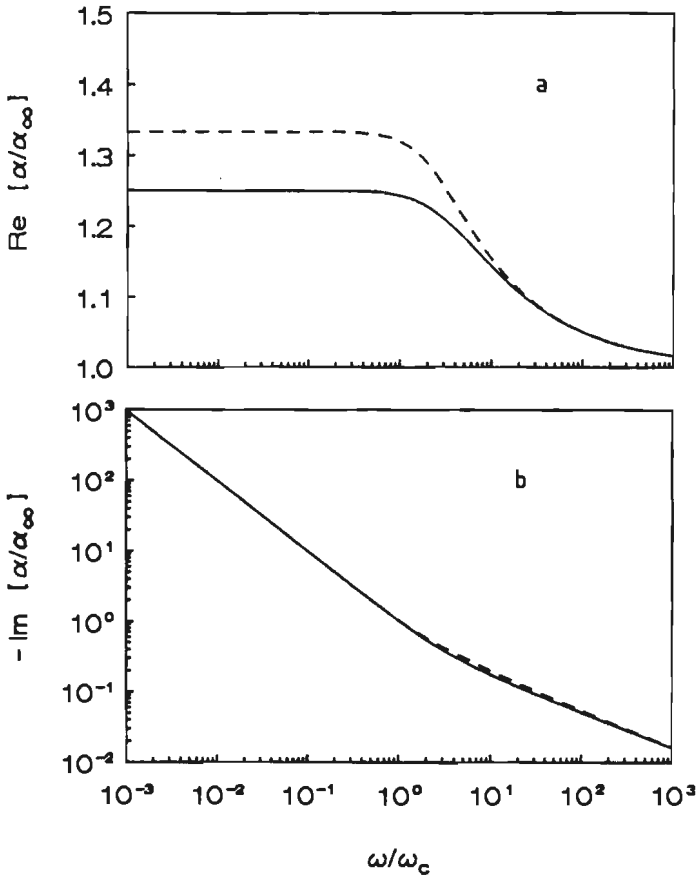
Figure 5.1: *Real parts (a) and negative imaginary parts (b) of the dynamic reduced tortuosity for the tube flow (dashed lines) and the scaling function by Johnson et al. (drawn lines). We have chosen $M = 1$.*

space as an ensemble of circular ducts of some radius R. In this case the interaction force $b(\omega)/b_0$ is given by (Zwikker & Kosten 1949; Biot 1956; Stoll 1974; Van der Grinten 1987, p. 22):

$$\frac{b(\omega)}{b_0} = \frac{1}{4} i \mu^2 \frac{J_1(i^{3/2}\mu)}{i^{3/2}\mu J_0(i^{3/2}\mu) - 2J_1(i^{3/2}\mu)}, \qquad (5.47)$$

where J_1 and J_0 are Bessel functions of first and zeroth order, respectively. Furthermore, $\mu = R\sqrt{\omega/\nu}$, where ν is the kinematic viscosity. It was noticed before (Biot 1956; Stoll 1974) that all porous media may be described by (5.47), where the argument μ of the Bessel functions was modified by multiplicative "structure factors" $\sqrt{\delta^2/8\xi}$ or $\sqrt{n^2/s}$. In the language of this chapter, we find that any porous medium $\mathcal{P}$ may be described as an ensem-

53

ble of circular ducts of radius $R = M_p \Lambda_p$. This yields $\mu = \sqrt{8 M_p \omega / \omega_c}$. For a porous medium consisting of a series of two-dimensional slits, for example, we find $M = 2/3$, yielding $\mu = \sqrt{16\omega/3\omega_c}$, which is in agreement with the Biot paper (1956). Although the introduction of "structure factors" may seem to be an ad hoc procedure, essentially any function that satisfies the conditions (5.3) and (5.44) of the previous sections, will adequately describe the fluid-solid interaction over the full frequency range. The following function was proposed by Johnson *et al.* (1987):

$$\frac{k(\omega)}{k_0} = \frac{1}{[1 + \frac{1}{2} i M \frac{\omega}{\omega_c}]^{1/2} + i \frac{\omega}{\omega_c}} \tag{5.48}$$

It is important to notice that in the original article, this function is written for the $\exp(-i\omega t)$ convention. Real and negative imaginary parts of the tortuosity for both functions (5.47) and (5.48) are plotted in figures 5.1a and 5.1b. For the sake of definiteness we have chosen $M = 1$. Use has been made of the relations (5.1), (5.2) and (5.46). We find that both functions display essentially the same behaviour. The only major difference is in the low frequency limit of $\mathcal{R}e[\alpha(\omega)]$ (1.33 versus 1.25). For high frequencies, $-\mathcal{I}m[\alpha(\omega)]$ shows an $\omega^{-1/2}$ dependence, whereas for low frequencies an ω^{-1} dependence is found.

5.5   Numerical computations

Numerical computations were performed on two different types of rotation-symmetrical pore geometries with lenght L, drawn in figures 5.2 and 5.3. Pore type 1 has a width W and a rotational axis $P_1 P_5$. The surface of revolution, bounding its pore volume, is described by the generator curve $P_2 P_3 P_4$. It consists of line-element $P_3 P_4$ and of 1/4 circle-segment $P_2 P_3$, with radius R and centre C. The geometry of pore type 1 can be varied in two different ways:
    - altering R while maintaining $W = L$.
    - altering W while maintaining $R = 0.5L$.
Pore type 2 is described by generator curve $P_2 P_3 P_4 P_5$. It consists of line-element $P_4 P_5$ and 1/4 circle-segment $P_2 P_3$, with radius R_1 and centre C_1, and 1/4 circle-segment $P_3 P_4$, with radius R_2 and centre C_2. Both centres define the straight line $C_1 C_2$ at a distance $0.5L$ from the rotational axis $P_1 P_6$. The distance between C_1 and C_2, $d(C_1, C_2)$, is defined by the relation $d(C_1, C_2) = R_1 + R_2 = 0.75L$. The geometry of pore type 2 can be varied by changing both R_1 and R_2 according to this relation.
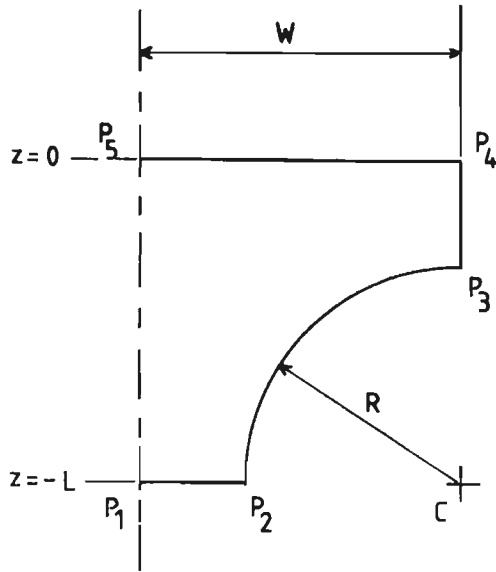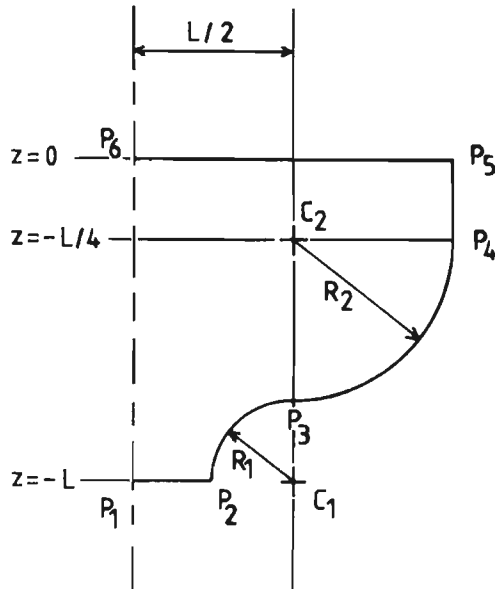
Figure 5.2: *poretype 1.*

Figure 5.3: *poretype 2.*

Using the SEPRAN finite element package (Cuvelier, van Steenhoven & Segal 1986), we computed α_∞, Λ_2 and k_0/ϕ_0 for poretype 1. Results are presented in figures 5.4 and 5.5. We used relations (5.35) and (5.40), respectively, to compute α_∞ and Λ_2. In this way, we solved the potential problem $\mathbf{u}_0 = -\nabla_y \psi$, where $\psi = 0$ at $z = 0$ and $\psi = 1$ at $z = -L$. Also, introducing the vector $\mathbf{n}$ normal to the pore walls, a Neumann type boundary condition was prescribed at the pore walls: $\mathbf{n}.\nabla_y \psi = 0$.

Furthermore, we computed k_0/ϕ_0 by solving the Stokes problem $\eta \nabla_y^2 \mathbf{u}_0 = -\nabla p$, where $p = 0$ at $z = 0$ and $p = 1$ at $z = -L$. A Dirichlet type boundary condition was prescribed at the pore walls: $\mathbf{u}_0 = \mathbf{0}$. For all computations, the accuracy was checked by refining the numerical grid several times.

Subsequently, we computed α_∞, Λ_2 and k_0/ϕ_0 for poretype 2. Also in this case, the accuracy was checked by grid refinement. The results of these computations are presented in figures 5.6. Varying this pore geometry, we achieved a perpendicular pore wall shift which enabled us to compute Λ_1, using equation (5.37). Results of this additional computation are included in figure 5.6b. We find in good approximation $\Lambda_1 = \Lambda_2$, as was also theoretically expected, thus showing reliability of our numerical methods. The results of all computations were then used to obtain the values for M, using equation (5.6). These M-values are listed in table 5.1.

R/L	M	W/L	M	R_1/L	M
0.3	1.04 ± 0.02	1.0	1.00 ± 0.02	0.05	1.25 ± 0.07
0.5	1.00 ± 0.02	0.9	0.99 ± 0.02	0.10	1.08 ± 0.07
0.6	0.98 ± 0.02	0.8	0.96 ± 0.02	0.15	1.03 ± 0.07
0.7	0.98 ± 0.02	0.7	0.95 ± 0.02	0.20	0.98 ± 0.05
0.75	0.97 ± 0.02	0.65	0.94 ± 0.02	0.25	0.96 ± 0.05
0.8	0.95 ± 0.02	0.6	0.93 ± 0.02	0.30	0.94 ± 0.05
0.85	0.95 ± 0.02			0.35	0.92 ± 0.05
0.9	0.93 ± 0.02			0.40	0.92 ± 0.02
				0.45	0.90 ± 0.02

Table 5.1. *Calculation of M-values for different pore types.*

It apppears that M is weakly dependent on pore geometry. The parameters R/L, W/L and R_1/L are varied over a wide range of magnitudes without affecting M for more then about 20%. Maximum deviation from $M = 1$ is found for strongly curved pore geometries. Thus, indeed, we find that many porous media satisfy the simple approximate scaling law that $k(\omega)/k_0$ is a function of only one independent parameter ω/ω_c.

Figure 5.4: *Numerical calculations of characteristic poretype 1 parameters.* $W/L = 1.0$. Λ *has been calculated using the* Λ_2-*approach.*
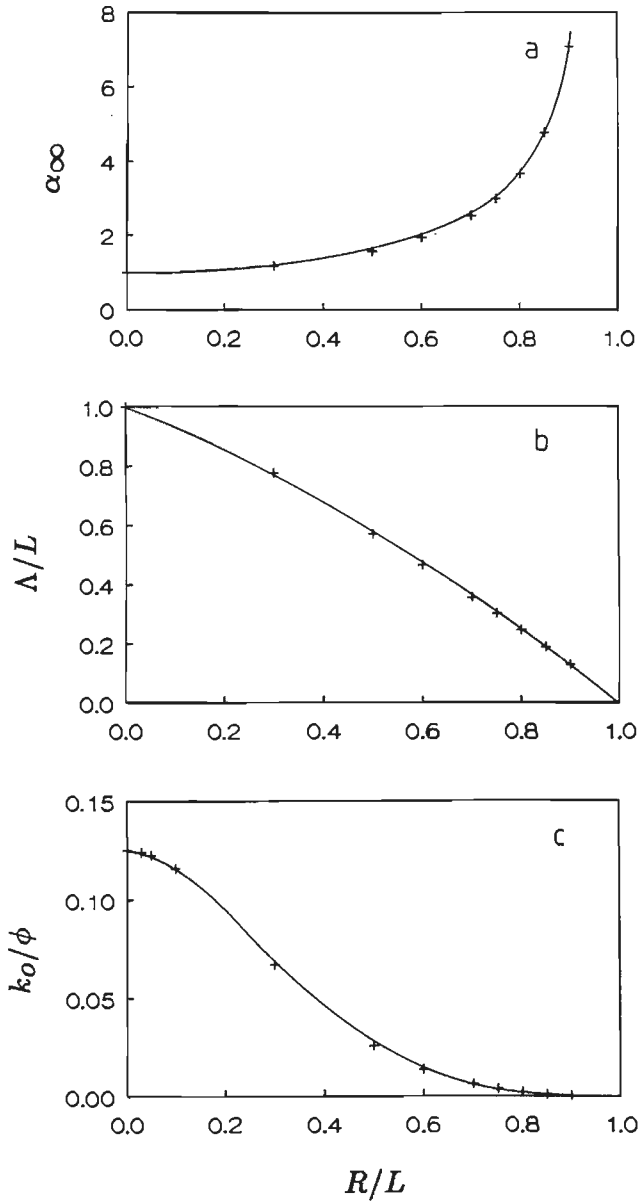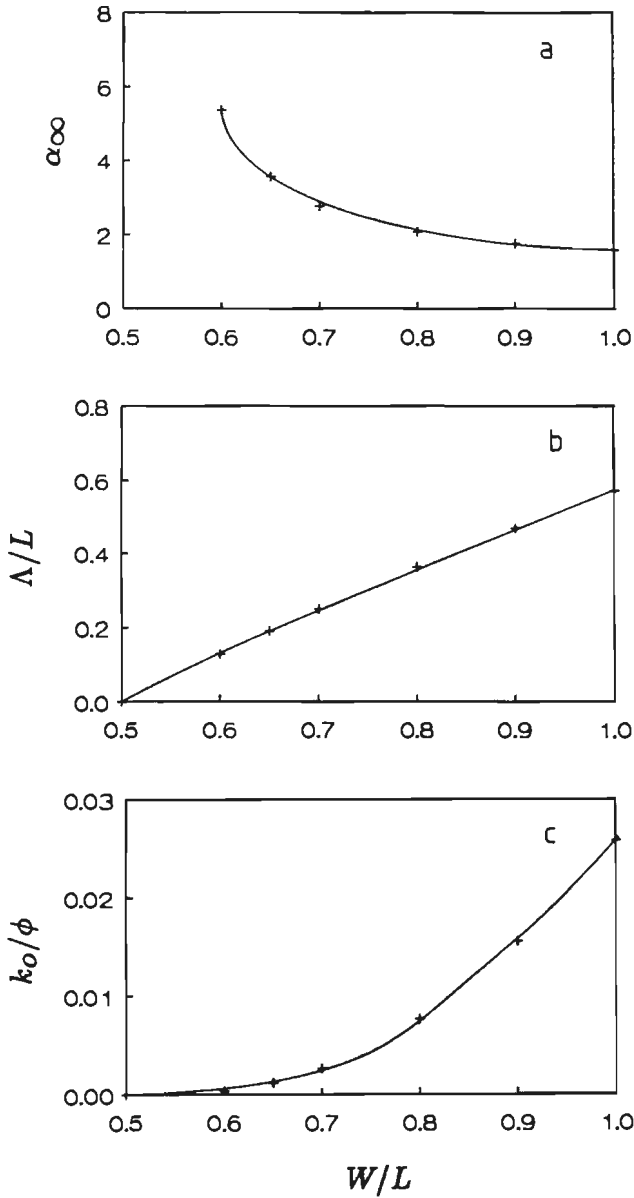
Figure 5.5: *Numerical calculations of characteristic poretype 1 parameters.* $R/L = 0.5$. Λ *has been calculated using the* Λ_2-*approach.*
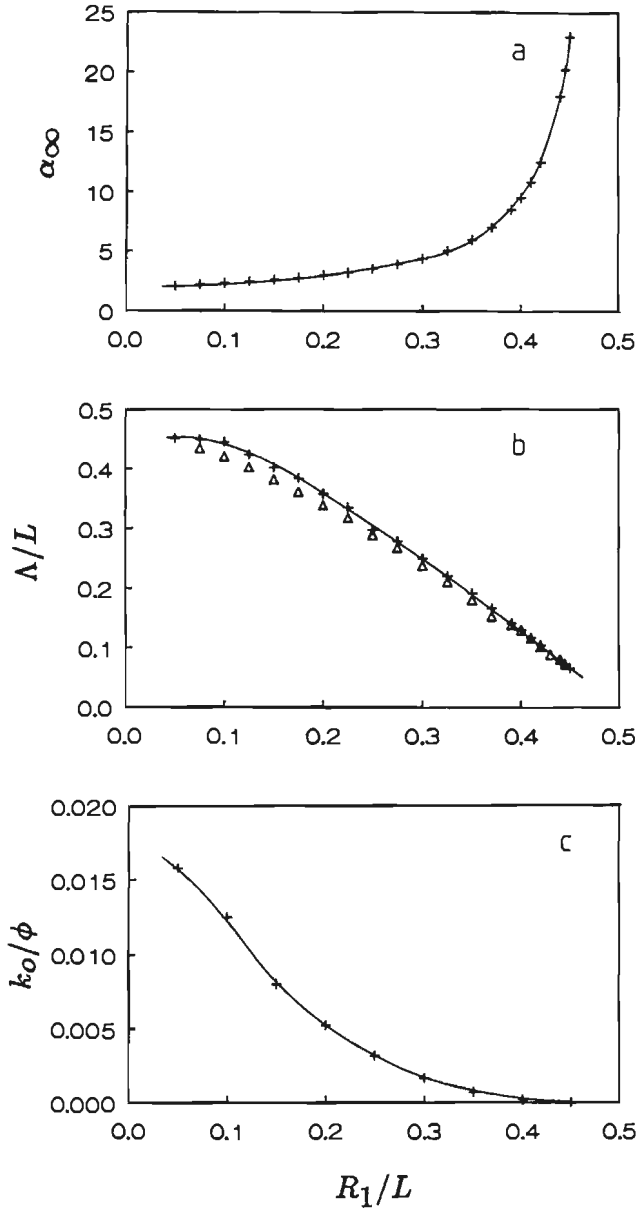
Figure 5.6: *Numerical calculations of characteristic poretype 2 parameters.* Λ *has been calculated using both the* Λ_1 ($\triangle$) *and* Λ_2 (+) *approach.*

6　Parameter tests

6.1　Porosity and homogeneity

We determined the porosity of five model porous media and of a sample of Bentheim sandstone. The model porous media are made out of five different particle types: a) glass beads; size range: 0.40-0.52 mm, b) glass beads; size range: 1.16-1.40 mm, c) glass beads; size range: 2.50-3.50 mm, d) sand grains; size range: 0.3-0.6 mm, e) sand grains; size range: 2.0-4.0 mm. Each model porous medium contains only one particle type. These particles are glued together and to the walls of a brass cylinder by means of an epoxy resin (Scotchcast, 3M electrical resin 8, 5236). Each model porous sample has a length L_0 of 100 mm and a diameter d_0 of 60 mm. The brass cylinder has a lenght of 250 mm. The Bentheim sandstone sample, finally, has a length L_0 of 50 mm and a diameter d_0 of 74.5 mm. Porosities (ϕ_0) are measured by using the standard two-weight (dry and buoyant) method. This implies that we determined the dry weight G_0 of the porous sample, and the weight G_1 of the same sample when it was fully water saturated and fully water immersed. From these experiments both porosity ϕ_0 and particle density ρ_s are found:

$$(1 - \phi_0)V_b = \frac{G_0 - G_1}{g\rho_w}$$

$$1 - \frac{\rho_w}{\rho_s} = \frac{G_1}{G_0},$$

where V_b is the bulk volume of the porous sample, g is the constant of gravity, and ρ_w is the water density. Measured porosities and particle densities are presented in table 6.1 at the end of this paragraph.

In this way, however, only an average porosity value is obtained. For the porous samples that are studied in this chapter, we assume that local deviations from the average values are small, because of small sample lengths, i.e low L_0/d_0 ratios. In chapter 7, however, we describe wave experiments performed on porous samples that have much higher L_0/d_0 ratios. For these experiments we used a) a column consisting of sand grains in the range 0.3-0.6 mm, which are glued together by means of an epoxy resin (Scotchcast, 3M electrical resin 8, 5236), and b) a column of Bentheim sandstone with a length of 1102 mm and a diameter of 74.5 mm. The former column has a
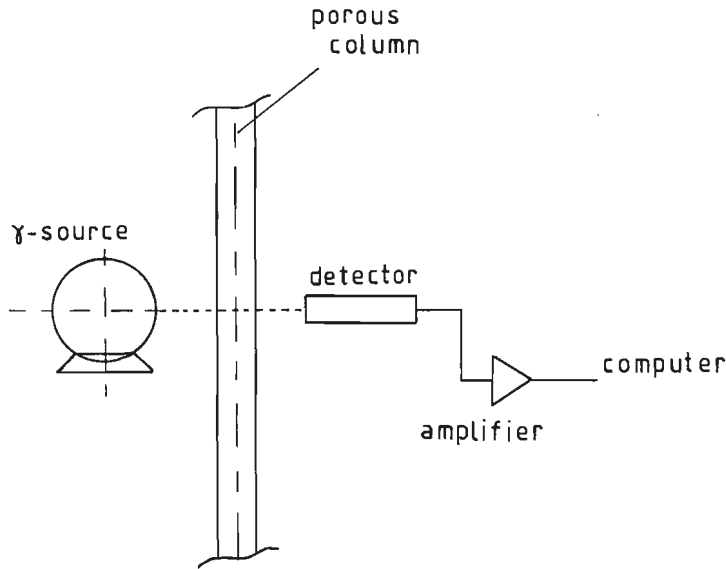
Figure 6.1: *Schematic drawing of the gamma-ray transmission scanner. The ^{137}Cs γ-source and the detector are translated simultaneously along the porous cylinder. Detector signals are amplified and recorded by the computer.*

length of 1410 mm and a diameter of 74 mm, and was extensively described by Van der Grinten (1987, pp. 43-45). In a review of studies (Dullien 1975; Macdonald, El-Sayed, Mow & Dullien 1979), it was shown that local deviations from the average porosity value may influence permeability properties enormously. Therefore the homogeneity of the sand column was tested by Van der Grinten by means of a gamma-ray transmission scanner, developed at Delft Geotechnics (Van der Grinten 1987, pp. 45-47). Variations in the porosity appeared to be within 7% of the average value.

We used the same method to test the homogeneity of the Bentheim sandstone column. The principle of this method was described by De Swart & Groeneveld (1970), Been (1981), Davidson, Bigger & Nielsen (1963) and Van der Grinten (1987, p 46). The set-up is drawn schematically in figure 6.1. A ^{137}Cs γ-source and a detector are moved simultaneously along a porous cylinder and the detector signal versus the position along the sample is recorded. The main energy of ^{137}Cs is a 0.66 MeV γ-peak. The detector is a 1 inch NaI scintillation crystal with a photo multiplier. By means of a narrow windowed one-channel pulse height analyser, only the non-scattered photons are counted, and we measure the attenuation due to the Compton effect, which is the most important attenuation mechanism at the 0.66 MeV
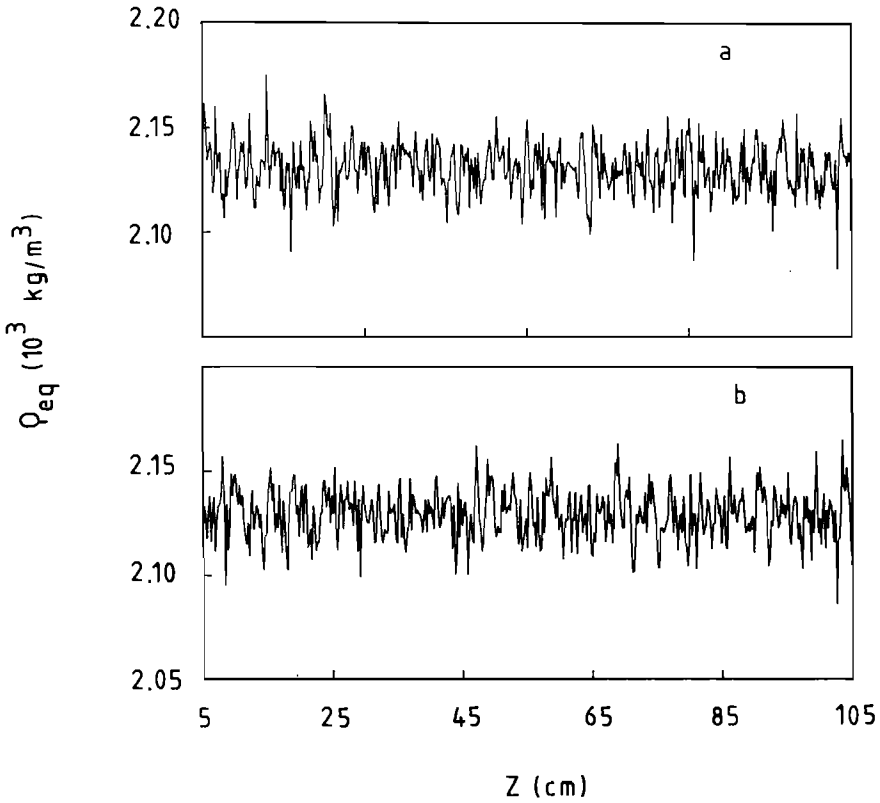
Figure 6.2: *Equivalent density plots of the Bentheim sandstone column, obtained by means of a γ-ray transmission scanner. In (b) the column is rotated 90 degrees from the initial state (a). The density is plotted versus the position z along the column*

energy level. We may write the ratio of the recorded intensity I and the source intensity I_0:

$$\frac{I}{I_0} = \exp(-\mu\rho d_0), \tag{6.1}$$

where μ is the mass attenuation coefficient, ρ the density of the porous sample, and d_0 the diameter of the sample. For Compton attenuation, μ is proportional to the ratio of the atomic number Z and the mass number B of an element. This means that for light elements ($Z/B = 1/2$), μ is a constant. The only exception is hydrogen ($Z/B = 1$). Therefore in γ-attenuation experiments, the equivalent water density ρ_{eq} is $20/18 = 1.11$

times the physical water density. From eq.(6.1) we write:

$$\frac{I}{I_0} = \exp(-\mu_{eq}\rho_{eq}d_0), \tag{6.2}$$

where the equivalent mass attenuation coefficient, μ_{eq}, is now a constant for all light elements. The γ-intensity is recorded, which initially leads to a logarithmic density scale. After scaling, we obtained a linear density scale (figure 6.2a). After the first density measurement the column is rotated 90 degrees and a second density scan is performed (figure 6.2b). As the diameter and the grain density of the porous column are constants, variations in density must be caused by porosity variations. From the results of figures 6.2 we find $\phi_0 = 0.20 \pm 0.02$, which is in agreement with the average value. The density measurement procedure was calibrated with small water-filled calibration vessels of several diameters.

	sample type	ϕ_0	ρ_s (10^3 kgm^{-3})
1	Bentheim sandstone	0.23±0.02	2.65 ± 0.05
2	sand grains 0.3-0.6 mm	0.29±0.02	2.44 ± 0.05
3	glass beads 0.40-0.52 mm	0.31±0.02	2.67 ± 0.05
4	glass beads 1.16-1.40 mm	0.31±0.02	2.71 ± 0.05
5	sand grains 2.0-4.0 mm	0.31±0.02	2.44 ± 0.05
6	glass beads 2.50-3.50 mm	0.32±0.02	2.65 ± 0.05

Table 6.1. Porosities and grain densities.

6.2 Tortuosity

The tortuosity is determined in an electrical conductivity experiment. The analogy between the acceleration of an inviscid incompressible fluid within a rigid porous medium, and the electrical current density within an electrolyte filled porous insulator, was first demonstrated by Brown (1980). Later this analogy was also discussed by Johnson & Sen (1981), and experimentally verified by Johnson, Plona, Scala, Pasierb & Kojima (1982). We may write:

$$\frac{\alpha_\infty}{\phi_0} = \frac{\sigma_f}{\sigma}, \tag{6.3}$$

where σ is the conductivity of the fluid filled porous insulator, and σ_f is the intrinsic fluid conductivity. The α_∞/ϕ_0 ratio is known as the formation factor F. The set-up is drawn in figure 6.3. Two electrodes, consisting of
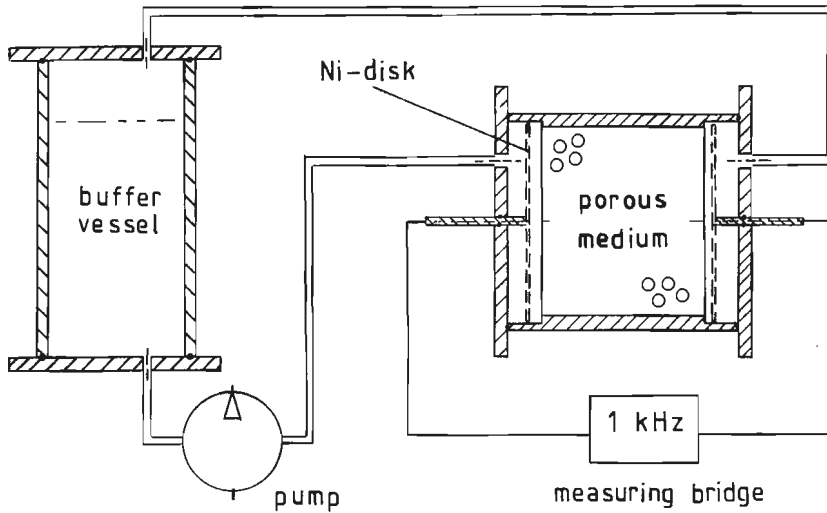
Figure 6.3: *Set-up for measuring the formation factor of a porous sample that is saturated with a saline solution. The buffer vessel helps to maintain constant temperature and saline concentration.*

porous Ni-disks, are placed on both sides against the porous sample, which has previously been saturated with a de-gassed 0.01 mol/l KCl saline solution. Conductivity is measured, using a resistance bridge (Marconi Universal Bridge TF2700). In order to avoid electrolysis, all conductivities are measured AC with a 1000 Hz frequency. For obvious conductivity reasons, the model porous samples within their containing brass cylinders (see section 6.1) could not be used. Five new samples were prepared in an identical way within perspex cylinders with a length of 85 mm and an internal diameter of 70 mm. Each porous sample has a length of 60 mm. For a sample of Bentheim sandstone, with a lenght of 50 mm and a diameter of 74.5 mm, a separate perspex containing cylinder was produced. In order to maintain constant temperature and saline concentration, we included a buffer vessel and a rotary pump in the set-up (see figure 6.3). The same set-up, but without the buffer vessel and rotary pump, was also used by Van der Grinten (1987, pp. 53-55). The results of the tortuosity measurements are presented in table 6.2.

	sample type	F
1	Bentheim sandstone	10.3 ± 0.2
2	sand grains 0.3-0.6 mm	9.3 ± 0.2
3	glass beads 0.40-0.52 mm	9.1 ± 0.2
4	glass beads 1.16-1.40 mm	8.7 ± 0.2
5	sand grains 2.0-4.0 mm	9.7 ± 0.2
6	glass beads 2.50-3.50 mm	8.2 ± 0.2

Table 6.2. Formation factors.

6.3 Steady-state permeability measurements

Stationary permeability properties were determined in two different one-dimensional flow set-ups, as will be descibed in the forthcoming. For low velocities the Darcy law holds:

$$\frac{\partial p}{\partial x} = -\frac{\eta}{k_0}\frac{Q}{A_0},\qquad(6.4)$$

where A_0 is the total cross sectional area of the porous sample and Q is the flow rate. For higher velocities, the Darcy law has to be extended by an extra term proportional to the flow rate squared:

$$\frac{\partial p}{\partial x} = -\frac{\eta}{k_0 A_0}Q + b_f \rho \left(\frac{Q}{A_0}\right)^2,\qquad(6.5)$$

where b_f is an arbitrary phenomenological constant, with the dimension of inverse length. The density of the fluid or gas in the pores is denoted by ρ. This relation (6.5) is often referred to as Forchheimer's law (Forchheimer 1901). If the flow is in the laminar regime, b_f is a function of the pore geometry only, and not of the Reynolds number. The second term on the right hand side accounts for the convective inertial effects, which are proportional to ρQ^2. The linear superposition of the viscous and inertial effects embodied in equation (6.5), cannot be justified on purely theoretical grounds, but experimental and numerical verificatation has been given in the past (Beavers & Sparrow 1969; Beavers, Sparrow & Rodenz 1973; Van der Grinten 1987, pp. 47-51; Coulaud, Morel & Caltagirone 1988).
In order to obtain low Reynolds numbers, the three most permeable porous media were saturated with a fluid of high viscosity. We used a clear oil with a density $\rho = 860.0$ kgm^{-3} at a temperature of 23 °C.
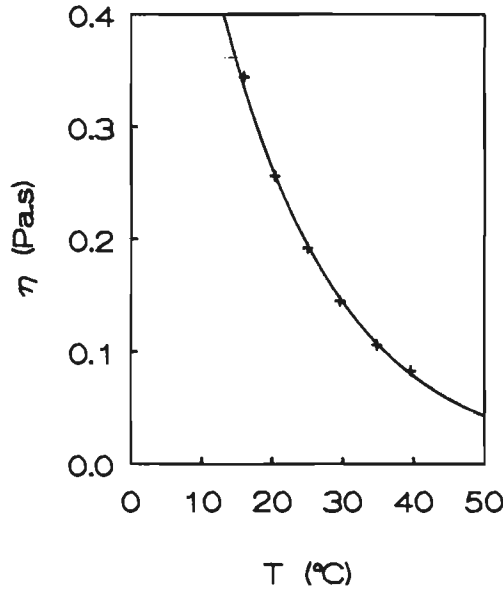
Figure 6.4: *Viscosity of oil used in permeability measurements*

The viscosity of the oil is given in figure 6.4 as a function of temperature. Permeabilities were then determined by means of a so-called falling head test. The set-up is drawn in figure 6.5. On top of the brass cylinder containing the porous sample, we mounted a perspex cylinder with a length of 1150 mm and an internal diameter A_1 of 70 mm (not visible in figure 6.5). This cylinder was filled with oil. The momentary oil level height above a certain reference height, is called $h(t)$. The reference height is defined in figure 6.5. The initial oil level height is called h_0. Ignoring the second term in eqation (6.5), from (6.5) we may write:

$$\ln\left(\frac{h_0}{h}\right) = \frac{k_0}{\eta}\frac{\rho g}{L}\frac{A_0}{A_1}t, \tag{6.6}$$

where g is the constant of gravity. The amount of oil permeating, which is directly related to $h(t)$, is measured by means of an electronic balance (Mettler P3600) as a function of time. We also measured $h(t)$ directly, by means of a calibration on the perspex cylinder. Measurements for all three samples are presented in figure 6.6. We find, indeed, that there is a neat linear relationship between $\ln[h_0/h(t)]$ and time. Resulting permeabilities are presented in table 6.3 at the end of this paragraph.
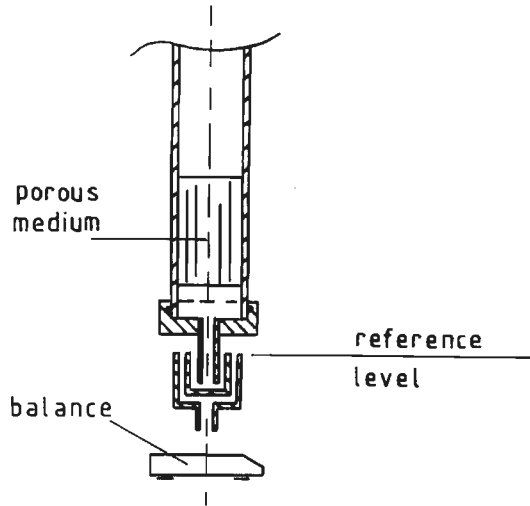
Figure 6.5: *Set-up for permeability measurements by means of an oil flow. The permeating oil flow is measured as a function of time.*
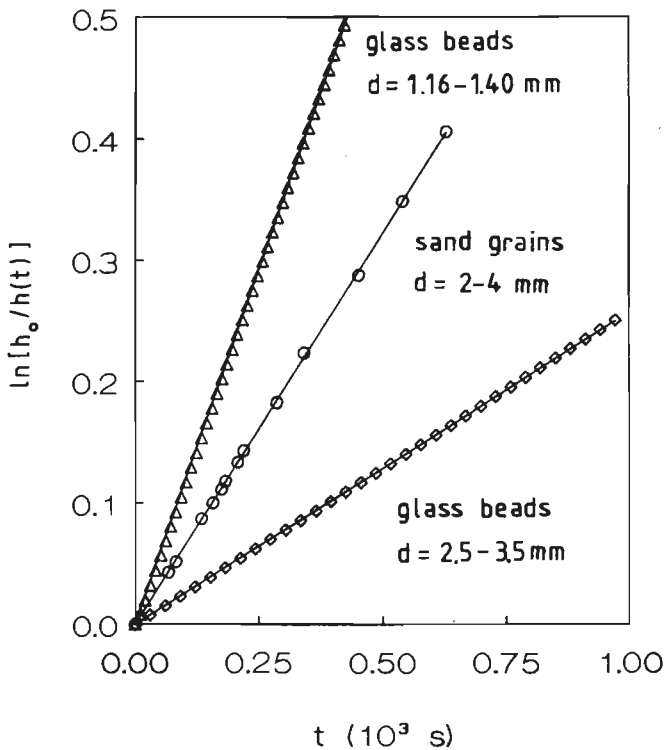
Figure 6.6: *Permeability measurements for three model porous samples at a temperature of 23 °C. The reduced oil level height $h_0/h(t)$ is plotted logarithmically against time.*

67
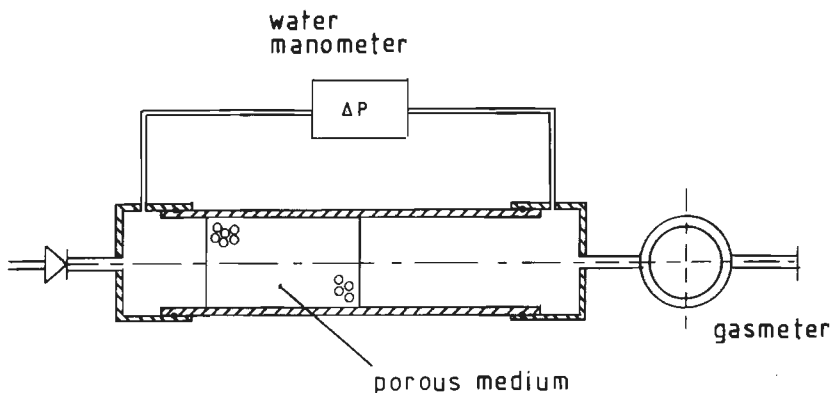
Figure 6.7: *Set-up for permeability measurements by means of an air flow. The air flow is measured by means of a gasmeter. The air flow resistance follows from the pressure drop over the porous sample.*
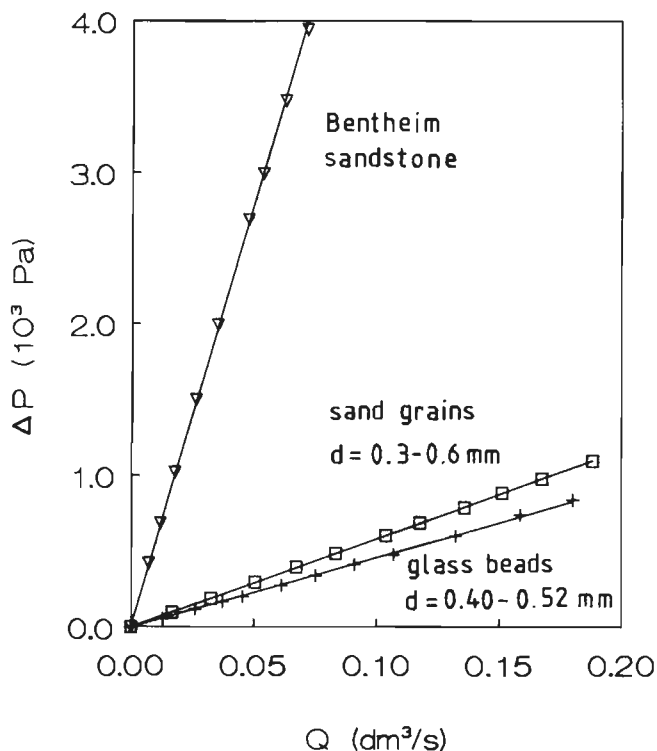
Figure 6.8: *Results of air flow permeability measurements for two model porous samples and for the Bentheim sandstone sample at a temperature $T_0 = 23°C$ and a pressure $p_0 = 1.01$ bar. The pressure drop over the porous sample is plotted against fow rate.*

For the three least permeable porous samples, oil percolation experiments are rather time consuming. We performed air flow experiments instead. The set-up is drawn in figure 6.7. It consists of two pressure chambers connected via the porous sample. Flow rates Q are varied modifying the upstream pressure, and measured by means of a gasmeter (Meterfabriek Dordrecht, Natte precisie gasmeter, Type 1). The pressure drop Δp across the sample is measured, using a highly sensitive water manometer (v.Essen, Betz micromanometer, 500 mm). Experimental results are presented in figure 6.8. We find that there is a linear relationship between Q and Δp. Apparently the viscous term is dominant over the inertia term, and the second term on the right hand side of equation (6.5) is therefore neglected. Permeability values are subsequently calculated and presented in table 6.3.

	sample type	k_0 (10^{-10} m^2)
1	Bentheim sandstone	0.037±0.003
2	sand grains 0.3-0.6 mm	1.00±0.05
3	glass beads 0.40-0.52 mm	1.40±0.05
4	glass beads 1.16-1.40 mm	9.00±0.05
5	sand grains 2.0-4.0 mm	27.7±0.5
6	glass beads 2.50-3.50 mm	42.0±0.5

Table 6.3. stationary permeability values.

6.4 Dynamic permeability measurements

Auriault, Borne & Chambon (1985) were the first to report experimental data, showing the transition from the viscosity dominated, low frequency regime towards the inertia dominated, high frequency regime. We must notice that in their paper the dynamic permeability is written in the form: $\eta/k(\omega) = H_1 + iH_2$. Measured data are presented for $\phi_0 a^2 H_1/2\eta$ and $\phi_0 H_2/\rho_f\omega$, where a is a length parameter of the porous medium. For an oscillating flow within a cylindrical duct of radius R, we find $a \equiv R$, $\phi_0 a^2 H_1/2\eta \equiv 4\mathcal{R}e[k_0/k(\omega)]$ and $\phi_0 H_2/\rho_f\omega \equiv \mathcal{R}e[\alpha(\omega)]$. They paid particular attention to the high frequency range. Measurements were performed on one slit-like pore geometry.

In 1988, Charlaix, Kushnick & Stokes presented experimental data over a wide range of reduced frequencies. An oscillating flow was induced by an audio speaker, driving a latex membrane. They used small porous cylinders with lengths of 50-70 mm and diameters of 4.3 mm, consisting of sintered glass beads and sintered, crushed, glass.

69
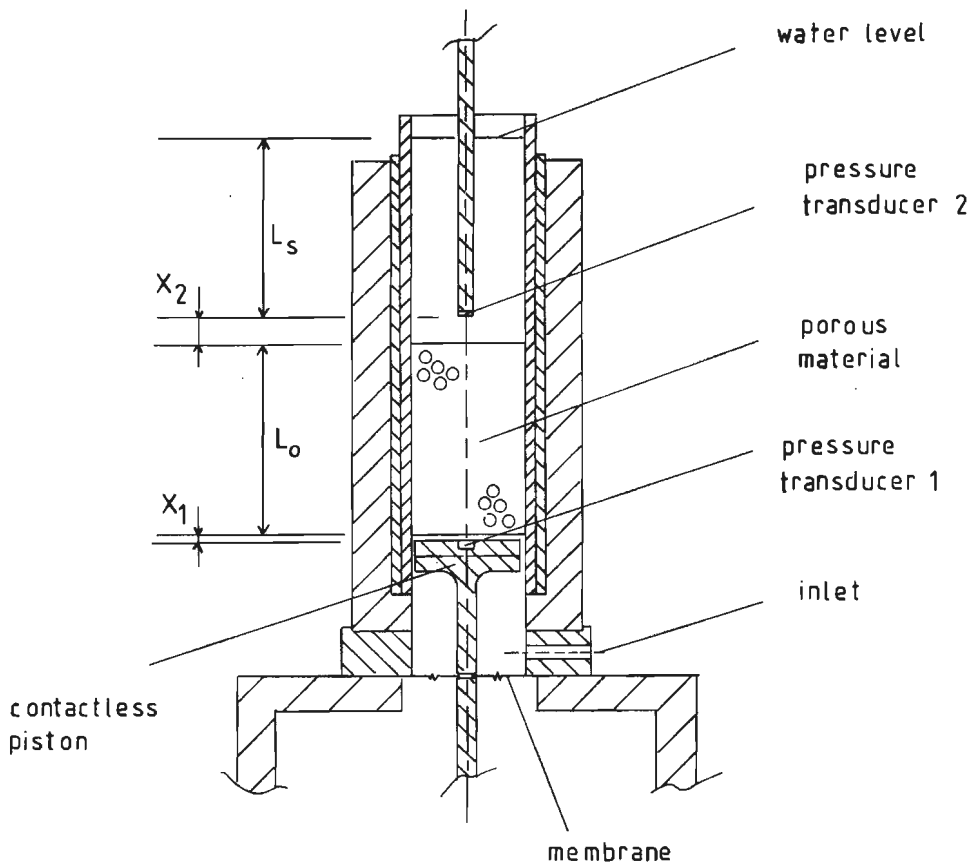
Figure 6.9: *Set-up for dynamic permeability measurements. The pressure drop over the sample is measured by means of two pressure transducers PT1 and PT2. Flow rates are deduced from PT2 measurements.*

We report here experimental data of dynamic permeability, performed on the five model porous media that are described section 6.1. We used the setup drawn in figure 6.9, which was already schematically proposed by Biot (1961). As the particles of the five model porous samples are glued together and to the walls of a brass cylinder by means of an epoxy resin, any free motion of the porous material is avoided. As we described in section 6.1, the brass cylinder has a length of 250 mm and an internal diameter of 60 mm. We also saw that each porous sample has a length L_0 of 100 mm. As described in chapter 5, each porous sample may be characterized by a rollover frequency ω_c, which can only be calculated after determination of the stationary permeability k_0 and the formation factor α_∞/ϕ_0. Measure-

70

ments of the formation factor were described in section 6.2, and stationary permeability values were determined in section 6.3.

The sample is now carefully evacuated and the pores are filled with carbon dioxide. Subsequently, the sample is filled with de-gassed water until the water surface is about 20 mm below the open upper cylinder end. Compared to air, carbon dioxide is far better soluble in water, thus causing a quick dissolution of any gas remnants. An oscillatory flow is induced by means of a MB Electronics EA 1500 permanent magnet exciter, driving a contactless piston. The void space below the piston is bounded by a brass membrane, impermeably connected both to the cylinder wall and the piston-rod. The frequency range is from 12 to 300 Hz, which causes $\lambda/4 \gg L_0$, where we have introduced the wavelength λ. Therefore, on this scale, fluid may be regarded incompressible. The experiment is run for displacement amplitudes corresponding to Reynolds numbers usually less than 1, where Reynolds numbers are taken with respect to the mean particle diameter. Therefore, the response of the fluid to the applied pressure gradient is still to be considered linear. The pressure drop across the porous sample is measured using PCB116A piezo-electric pressure transducers PT1 and PT2. PT1 is installed in the piston, whereas PT2 is mounted on the lower end of a cylindrical perspex shaft. Signals are modified by means of Kistler 5001 amplifiers. Defining $\hat{p}_2$ as the pressure amplitude recorded by PT2, and $\hat{v}_2$ as the undisturbed fluid velocity at some distance above PT2, flow rates are deduced from the upper pressure transducer measurements:

$$\rho_f i \omega \hat{v}_2 = \frac{\hat{p}_2}{L_{eff}}, \qquad (6.7)$$

where we have introduced the effective fluid height L_{eff} above PT2. We computed the local flow pattern and pressure distribution in the vicinity of PT2 as a solution of the steady potential problem, using the SEPRAN finite element package. A description of this finite element package is given in section 5.5. We found $L_{eff} = L_s + \Delta L$, where L_s is the length of the shaft below the fluid surface, and $\Delta L = 3.9$ mm. Introducing the macroscopic fluid velocity $\hat{v}_0$ within the porous sample, we may write a dynamic equivalent of Darcy's law:

$$\phi_0 \hat{v}_0 = \frac{k(\omega)}{\eta} \frac{\hat{p}_h - \hat{p}_l}{L_0}, \qquad (6.8)$$

where $\hat{p}_h$ and $\hat{p}_l$ are the fluid pressure amplitudes right below and above the porous sample, respectively. Pressures $\hat{p}_1$ and $\hat{p}_2$ though, are recorded at some distances x_1 and x_2 below and above the porous sample (see figure 6.9). By means of local application of continuity and momentum equations,

71

the pressures $\hat{p}_h$ and $\hat{p}_l$ can be expressed in terms of the recorded pressures $\hat{p}_1$ and $\hat{p}_2$:

$$\hat{p}_h = \hat{p}_1 - \hat{p}_2 \frac{(1-\beta)x_1}{L_{eff}} \tag{6.9}$$

$$\hat{p}_l = \hat{p}_2[1 + \frac{(1-\beta)(x_2 - \Delta L)}{L_{eff}}], \tag{6.10}$$

where β is the shaft-to-cylinder area ratio. Results of dynamic permeability measurements are presented in figures 6.10a and 6.10b. For each porous sample, dynamic permeability and frequency are scaled by corresponding k_0 and ω_c values, which are determined in the previous sections. In figure 6.10a, one clearly observes the rollover of the modulus of $k(\omega)/k_0$ from the value 1 at low frequencies to a $(\omega/\omega_c)^{-1}$ dependence at high frequencies. This rollover behaviour is also clearly visible considering the argument of $k(\omega)/k_0$ in figure 6.10b. Errors are represented by the magnitude of the data symbols. The drawn curves in figures 6.10 correspond to a scaling function proposed by Johnson, Koplik & Dashen (1987):

$$\frac{k(\omega)}{k_0} = \frac{1}{[1 + \frac{1}{2}iM\frac{\omega}{\omega_c}]^{1/2} + i\frac{\omega}{\omega_c}}, \tag{6.11}$$

where for the sake of definiteness we have chosen $M = 1$. We notice that there is good overall agreement between experiment and theory for both absolute and phase values. At ω/ω_c-values of about 0.5, the experimentally determined absolute values of $k(\omega)/k_0$ are somewhat lower than predicted. This is caused by a persistent set-up resonance observed in the case of small particles. At the same ω/ω_c-values, this set-up resonance is also visible in the phase plot. Summarizing, we find that the present experimental results support the experiment-based conclusions of Charlaix *et al.* (1988) and the computational results of Sheng & Zhou (1988).

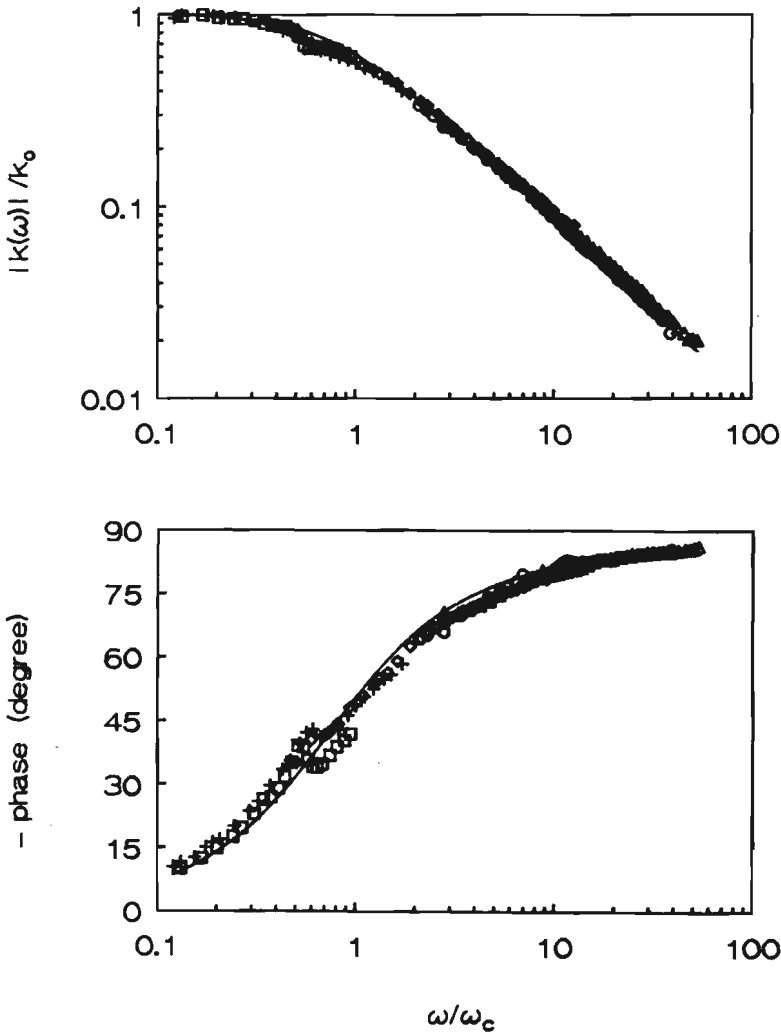Figure 6.10: *Absolute values (a) and negative phase values (b) of dynamic permeability measurements.* □ *sand grains 0.3-0.6 mm.* + *glass beads 0.40-0.52 mm.* ◇ *glass beads 1.16-1.40 mm.* △ *glass beads 2.50-3.50 mm.* O *sand grains 2.0-4.0 mm. The drawn curve represents the theoretical scaling function. Errors are indicated by the magnitude of the data symbols.*

6.5 Elastic Properties

In an isotropic elastic medium, the elastic constants E (Young's modulus), K_b (bulk modulus), K_p (constrained modulus), ν (Poisson's ratio), G (shear modulus) and λ and μ (Lamé's coefficients) may be defined. There are, however, only two independent parameters. Some frequently used relations are:

$$\mu = G = \frac{E}{2(1+\nu)}$$

$$\lambda = \frac{E\nu}{(1+\nu)(1-2\nu)}$$

$$K_b = \lambda + \frac{2}{3}\mu = \frac{E}{3(1-2\nu)}$$

$$K_p = \lambda + 2\mu = \frac{E(1-\nu)}{(1+\nu)(1-2\nu)}$$

Some of these relations are given by Achenbach (1973, p. 54). Van der Grinten (1987, pp. 52-53) determined the moduli of Young and the constrained moduli of both porous columns used for the wave experiments described in chapter 7. These porous samples are denoted as 1 and 2 in all tables in chapter 6.

For the determination of K_p, a pulse propagation experiment was performed, by means of a concrete tester (CSI-ctt4). For the determination of E, a resonance experiment was performed, by means of a so-called Elastomat (Institut Dr. Forster, Typ 1.015). The results are shown in table 6.4. From the E and K_p values, the ratios of Poisson were calculated.

	sample type	E (GPa)	K_p (GPa)	ν
1	Bentheim sandstone	13.4±0.2	14.7± 0.2	0.19 ± 0.01
2	sand grains 0.3-0.6 mm	3.9±0.2	10.2± 0.2	0.42 ± 0.01

Table 6.4. Elastic constants.

6.6   Preparation of a water-air mixture

Up to now we have only discussed the properties of the porous medium. We will now focus on the pore fluid. For the wave experiments, described in chapter 7, we need to create a homogeneous pore fluid with uniformly distributed air bubbles of equal size. An inhomogeneous air bubble distribution may cause reflections and extra damping, that makes it hard to give an adequate interpretation of the wave experiments. From our theoretical models, it follows that the minimum occurring wavelength is about 2 cm, corresponding to frequencies in the order of 100 kHz. The size of the air bubbles and their distance must therefore be smaller than 2 cm in order to justify the use of continuum theory. Therefore, the size and concentration of the air bubbles is controlled by adding some $Ca(OH)_2$ to the pore fluid. The reliability of this method was checked in optically transparant gelatin-water mixtures, as will be reported in section 6.10. Mean air bubble size and concentration are determined from measurements of the pore fluid compressibility, as will be discussed in section 6.9.

The preparation of the pore fluid, consisting of a water-air mixture, proceeds as follows. First, the porous sample is fully water-saturated. This is done by carefully evacuating the sample and filling the pores with carbon dioxide. Subsequently, the sample is filled with de-gassed water. Compared to air, carbon dioxide is far better soluble in water, thus causing a complete dissolution of any gas remnants. Next, in a separate vessel (see figure 6.11), an amount of water is saturated with air, at a constant pressure level. This is done by blowing air bubbles into the vessel. The amount of air dissolving in the water is controlled by the vessel pressure, which is higher than the atmospheric pressure. By means of a rotary pump, this air-saturated water is flushed through the porous column until its entire pore volume is refreshed about 50 times. Meanwhile, the porous column is held at the same pressure as within the vessel, and the blowing of air bubbles continues. Finally, the circulation is stopped, and the pressure is released. The pore fluid is now a super-saturated (200-300 %) air solution. Gas molecules start to form gas bubble nuclei. This may take place at any microscopic roughness in the pore surface, or in the surface of small pore fluid particles. This process is called heterogeneous nucleation. A description of this process and of the subsequent conditions for bubble growth is given by Ward, Johnson, Venter, Ho, Forest & Fraser (1982). The spontaneous (homogeneous) formation of air bubbles does not occur. For this process a super-saturated air solution of 2000 % is needed (Van Stalen & Cole 1987; Sillen 1983).
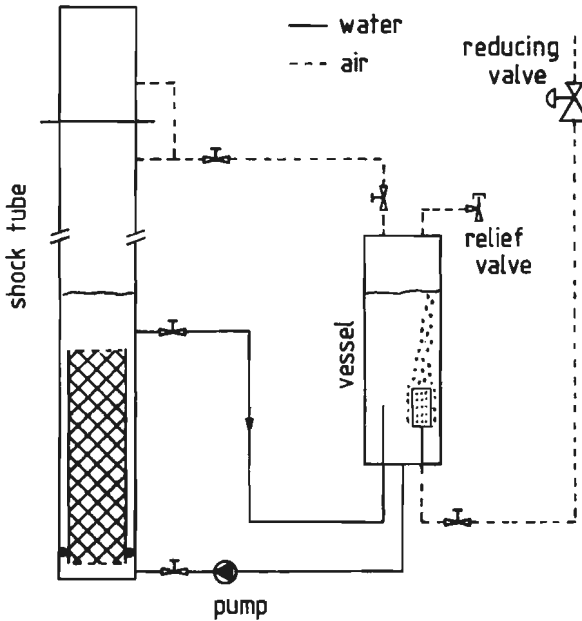
Figure 6.11: *Set-up for the preparation of a water-air mixture in the shock tube sample. In a separate vessel, an amount of water is saturated with air at a constant, super-atmospheric pressure. This is done by blowing small air bubbles into the water. The air-saturated water is circulated through the porous column by means of a rotary pump. After releasing the pressure, air bubbles are formed in the shock tube sample.*

6.7   Compressibility

By means of pore fluid compressibility measurements, the mean air bubble size and concentration may be determined. These data are needed to compute the dynamic bubble behaviour, described in chapter 4. For a compressibility experiment, the pore fluid is subjected to a small pressure increase Δp_1 during a time interval τ_1 (typically in the order of several minutes), which is small enough to ensure that almost no air from the bubbles is dissolved in the liquid. From the corresponding change in liquid volume, the pore fluid compressibility β_f is found:

$$\beta_f = \frac{1}{\rho_f}\frac{\partial \rho_f}{\partial p},\qquad(6.12)$$

which is a direct measure for the momentary air volume fraction $1 - s$. In this case, the compressibility experiment is denoted as "frozen". If, on the

other hand, the pore fluid is subjected to a stepwise pressure change Δp_2 during a time interval τ_2; $\tau_2 \gg \tau_1$, part of the air will gradually dissolve into the fluid until a new equilibrium is reached. This process is diffusion dominated. Both frozen and equilibrium conditions were reported previously by Sniekers, Smeulders, van Dongen & van der Kogel (1989).

In order to find a relation between the pore fluid compressibility and the air volume fraction, we write the mean density of the water-air mixture:

$$\rho_f = s\rho_l + (1-s)\rho_g + s\rho_d, \qquad (6.13)$$

where ρ_d is the mass of dissolved gas per unit fluid volume. To find the density change $d\rho_f$, we assume that the number of air bubbles per unit fluid volume will remain constant. The location of the individual air bubble is fixed. This assumption differs slightly from that of Barends and Teunissen. Barends (1980) assumes the total air mass in a unit volume to be constant, whereas Teunissen (1982) assumes that the relative velocity of air bubbles and water is zero. A pressure increase will cause the air bubbles within the unit fluid volume to shrink, which, in its turn, will cause pore fluid to enter the unit volume. Continuity of air mass within the unit volume requires:

$$d[(1-s)\rho_g + s\rho_d] = \rho_d ds \qquad (6.14)$$

Combination of equations (6.13) and (6.14) yields:

$$d\rho_f = (\rho_l + \rho_d)ds + s d\rho_l \qquad (6.15)$$

In good approximation, we may replace ρ_f by $s\rho_l$ in equation (6.12). We may then write from equations (6.12) and (6.15):

$$\beta_f = \beta_l + \frac{1}{s}\left(1 + \frac{\rho_d}{\rho_l}\right)\frac{\partial s}{\partial p} \qquad (6.16)$$

The second term between brackets in the above equation is in the order of 10^{-5}, and henceforth it will be neglected. The above relation is valid for both the frozen and the equilibrium condition.

In the "frozen" condition we assume $d\rho_d = 0$. From equation (6.14) we may write after integrating:

$$\frac{\rho_g}{\rho_{g0}} = \frac{1 - s_0}{1 - s}, \qquad (6.17)$$

where the subscript 0 refers to the initial state. Assuming that the vapour pressure in the air bubble, and the surface tension σ may both be neglected,

we find $p_g = p$. We also assume that the bubbles are compressed isothermally. Using the ideal gas law, we may write from equation (6.17):

$$\frac{p}{p_0} = \frac{1 - s_0}{1 - s} \tag{6.18}$$

From both the equations (6.16) and (6.18) we now find an expression for the "frozen" fluid compressibility:

$$\beta_f = \beta_l + \frac{(1 - s_0)\frac{p_0}{p^2}}{1 - (1 - s_0)\frac{p_0}{p}} \tag{6.19}$$

We shall next consider the equilibrium condition. Henry's solubility law states that, under isothermal conditions, the dissolved gas density ρ_d is very nearly proportional to the gas density ρ_g. This proportionality is expressed by the solubility coefficient ω_H, which is about 0.02 at room temperature. For the equilibrium condition, we may therefore write:

$$\rho_d = \omega_H \rho_g \tag{6.20}$$

From equation (6.14), we now find after integration:

$$\frac{\rho_g}{\rho_{g0}} = \left(\frac{1 - s_0 + \omega_H s_0}{1 - s + \omega_H s}\right)^{\frac{1}{1 - \omega_H}} \tag{6.21}$$

In good approximation, we may finally write:

$$\frac{\rho_g}{\rho_{g0}} = \frac{p}{p_0} = \frac{1 - s_0 + \omega_H s}{1 - s + \omega_H s}, \tag{6.22}$$

which is the equilibrium equivalent of (6.18). In figure 6.12, we have indicated what happens when the pore fluid, e.g. consisting of a water-air mixture of saturation $s_0 = 0.982$, is subjected to a pressure increase $\Delta p = p - p_0$. The instantaneous "frozen" saturation change, $\Delta s = s - s_0$, is found from (6.18), and indicated by the curve segment $A_0 A_1$ (see figure 6.12). When the pressure is subsequently held constant, air from the bubble is dissolved in the liquid, until a new equilibrium is reached. This is a diffusion dominated process, indicated by the line segment $A_1 A_\infty$ in figure 6.12. The equilibrium curves in figure 6.12 are found from equation (6.22). As we see, the equilibrium curve is depending on the initial saturation s_0, whereas this is not the case for the "frozen" curve. As an example, we have drawn two equilibrium curves in figure 6.12. We notice that for $p/p_0 \geq (1 - s_0)/\omega_H + 1$, all air bubbles will finally dissolve in the liquid.
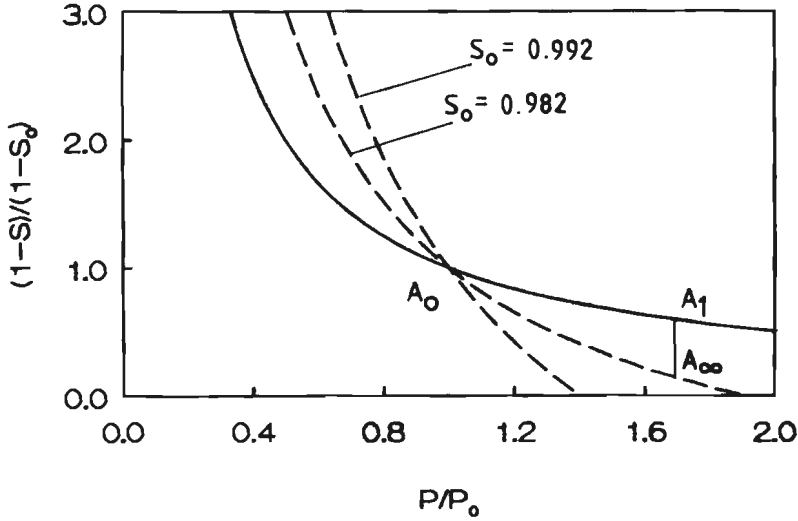
Figure 6.12: *Reduced air volume fraction versus the reduced pressure. The frozen (solid line) and two different equilibrium (dashed lines) curves are plotted. For a given pressure increase, and for $s_0 = 0.982$, the air bubbles will shrink according to the path $A_0 A_1 A_\infty$. Above a certain limiting pressure increase, all the air bubbles will finally dissolve.*

6.8 Diffusion

We shall now give a quasi-steady description of the diffusion process. We will follow the procedure of Smeulders, De la Rosette & van Dongen (1992). Considering a gas bubble of radius R, we define the origin of coordinates at the bubble centre, which is at rest. The position of any point in the fluid is indicated by $\mathbf{r}$. Following Henry's law, a sudden stepwise increase, Δp, will cause a corresponding increase in the dissolved gas density at the bubble radius ρ_{db}. Defining a reduced dissolved gas density C at a fixed time t, we may write:

$$C = \frac{\rho_d(\mathbf{r}, t) - \rho_{d\infty}(t)}{\rho_{db} - \rho_{d\infty}(t)}, \tag{6.23}$$

where $\rho_{d\infty}$ is the dissolved gas density far away from the bubble. From the quasi-steady diffusion equation, $\nabla^2 C = 0$, we find $C = R/r$. The mass flux dM/dt from the bubble towards the surrounding fluid may now be calculated:

$$-\frac{4}{3}\pi \rho_g \frac{dR^3}{dt} = \frac{dM}{dt} = 4\pi R D_e (\rho_{db} - \rho_{d\infty}), \tag{6.24}$$

79

where D_e is an effective diffusion constant. It is equal to the diffusion constant D in water, divided by the tortuosity parameter α_∞: $D_e = D/\alpha_\infty$ (Smeulders *et al.* 1992). Considering next the situation of a large number of bubbles with number density N m^{-3}, we define the average bubble distance $2a$ as $N^{-1/3}$. If this average bubble distance far exceeds the bubble radius, equation (6.24) still holds if we replace the factor $\rho_{d\infty}(t)$ by $\rho_d(a,t)$. From the mass conservation law we may write:

$$\frac{4}{3}\pi\rho_g R^3 + \int_R^a 4\pi R^2 \rho_d d\tau = \frac{4}{3}\pi\rho_g R_1^3 + \frac{4}{3}\pi\rho_{d1}(a^3 - R_1^3), \qquad (6.25)$$

where the index 1 refers to the initial state. This initial state is indicated as A_1 in figure 6.12. In good approximation, the integral in the above equation is equal to $\frac{4}{3}\pi\rho_d(a,t)(a^3 - R^3)$. Assuming $R^3 \ll a^3$, and $R_1^3 \ll a^3$, we find from equation (6.25):

$$\rho_d(a,t) = \rho_{d1} + \rho_g\left(\frac{R_1^3}{a^3} - \frac{R^3}{a^3}\right) \qquad (6.26)$$

Substitution of this equation in (6.24) yields a differential equation for the reduced bubble radius $\eta(t) = R(t)/a$:

$$\eta\frac{d\eta}{dt'} = \eta_\infty^3 - \eta^3, \qquad (6.27)$$

where $\eta_\infty^3 = (\rho_{d1} - \rho_{db})/\rho_g + R_1^3/a^3$. Furthermore, we have introduced the reduced time $t' = D_e t/a^2$. When the diffusion process is approaching its new equilibrium state for $t' \to \infty$, obviously $d\eta/dt'$ will tend to zero. The equilibrium state is indicated as A_∞ in figure 6.12. From equation (6.27), we find that $\eta \to \eta_\infty$. Solving the differential equation (6.27), we find:

$$
\begin{aligned}
t' &= \frac{1}{6\eta_\infty}\left[\ln\frac{\eta_\infty^2 + \eta_\infty\eta + \eta^2}{(\eta_\infty - \eta)^2} - \ln\frac{\eta_\infty^2 + \eta_\infty\eta_1 + \eta_1^2}{(\eta_\infty - \eta_1)^2}\right] \\
&+ \frac{1}{\eta_\infty\sqrt{3}}\left[\arctan\frac{2\eta_1 + \eta_\infty}{\eta_\infty\sqrt{3}} - \arctan\frac{2\eta + \eta_\infty}{\eta_\infty\sqrt{3}}\right], \qquad (6.28)
\end{aligned}
$$

where $\eta_1 = R_1/a$. Introducing a dimensionless parameter $\delta = \eta/\eta_1$, the above equation (6.28) may be rewritten:

$$
\begin{aligned}
t'\eta_1 &= \frac{1}{6\delta_\infty}\left[\ln\frac{\delta_\infty^2 + \delta_\infty\delta + \delta^2}{(\delta_\infty - \delta)^2} - \ln\frac{\delta_\infty^2 + \delta_\infty + 1}{(\delta_\infty - 1)^2}\right] \\
&+ \frac{1}{\delta_\infty\sqrt{3}}\left[\arctan\frac{2 + \delta_\infty}{\delta_\infty\sqrt{3}} - \arctan\frac{2\delta + \delta_\infty}{\delta_\infty\sqrt{3}}\right], \qquad (6.29)
\end{aligned}
$$

where, obviously $\delta_\infty = \eta_\infty/\eta_1$. We still have to make a link to the air volume fraction $1 - s$. We notice that:

$$1 - s = \frac{R^3}{a^3} = \eta^3 \qquad (6.30)$$

$$\frac{1 - s}{1 - s_1} = \delta^3 \qquad (6.31)$$

In figure 6.13, some diffusion curves are drawn for different values of the reduced equilibrium (end) saturation δ_∞. We notice that a negative (virtual) value for δ_∞ corresponds to a situation where the equilibrium state is under-saturated.
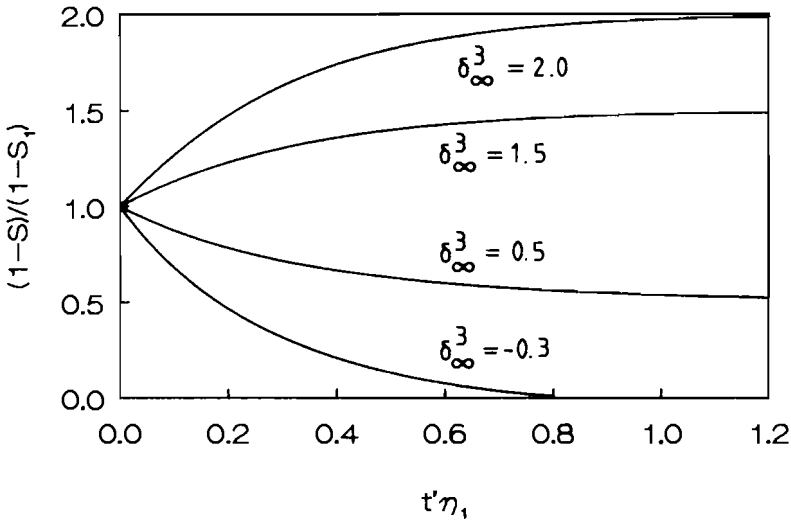

Figure 6.13: *Diffusion curves for different, reduced, equilibrium (end) saturations δ_∞. A negative value for δ_∞ corresponds to a situation where the equilibrium state is under-saturated.*

6.9   Optical set-up and measurements

The optical set-up for compressibility measurements of a fluid-saturated porous medium is depicted in figure 6.14. It was described previously by Van der Grinten (1987, p. 60). In the shock tube, we have mounted an optical section, containing two parallel windows. This section is located at some decimeters above the porous column, which is at the bottom of

the shock tube. The porous column is fluid-saturated, and the water level is some millimeters below the windows of the optical section. The optical section contains a He-Ne laser, the beam of which is reflected by a mirror. The mirror can be translated by means of a stepping motor. The reflected
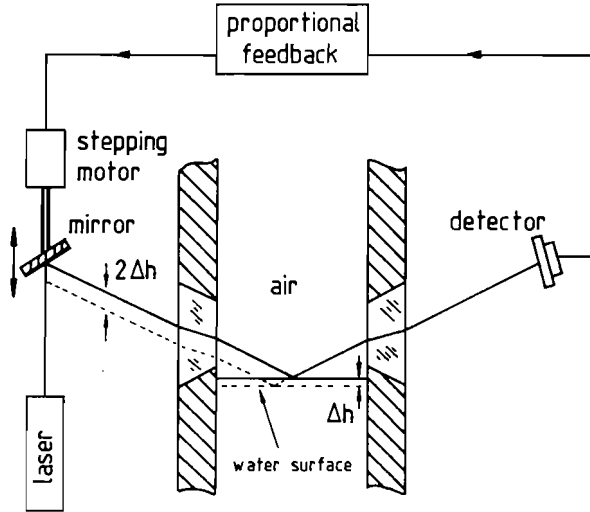

Figure 6.14: *Optical section for compressibility experiments of a fluid-saturated porous column.*

beam passes the window, reflects from the water surface, and reaches a differential diode detector. This detector generates a voltage, proportional to the difference in light intensity between the upper and lower half of the sensitive surface of the diode. This voltage signal is then used to activate the stepping motor and to translate the mirror, in such a way that the differential light intensity of the diode is minimized. The result is that the laser beam is always directed towards the centre of the diode detector, by means of mirror adjustment. The mirror displacement is detected by a transducer (Sangamo transducer 72822). One step of the stepping motor causes a mirror displacement of 10 μm. From figure 6.14, it becomes clears that this corresponds to a 5 μm displacement of the water surface. In this way, volume changes of $2.33 \cdot 10^{-5}$ dm^3 can be detected. A compressibility experiment will therefore consist of the registration of the mirror displacement as a function of the pressure change above the water surface. Calibration is performed when the shock tube is filled with de-aired water (Van der Grinten 1987, p. 61). We measured the compressibilities of the water-saturated sand column, and of the water-saturated Bentheim sandstone column. The

results are shown in figure 6.15. The measured volume change is reduced by the total water volume V_0, and the pressure change by the initial pressure p_0. We found $\beta_{ref1} = (7.7 \pm 0.1) \cdot 10^{-10}$ Pa^{-1} for the sand column, and $\beta_{ref2} = (5.1 \pm 0.1) \cdot 10^{-10}$ Pa^{-1} for the Bentheim sandstone column. These
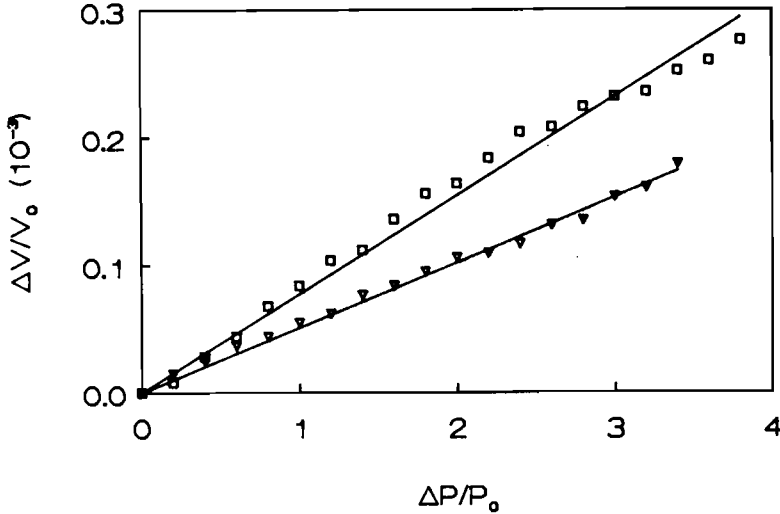

Figure 6.15: *Compressibility measurements of fully water-saturated porous columns.* □ *sand column* ▽ *Bentheim sandstone column.* V_0 *is the total water volume; p_0 is the initial pressure*

values obviously include the compressibilty of the o-rings and silicone kit, which are used in the set-up. From the linear relation between displacement and pressure in figure 6.15, it follows that the compressibity is a constant value, indicating that both columns are indeed fully water-saturated.

We will now consider the partially saturated case. A water-air mixture was prepared as described in section 6.6. After the release of the pressure, air bubble growth will begin, which is a diffusion dominated process. It is our aim to determine both mean air bubble radius and concentration. We shall show that this is possible by measuring the air volume fraction $(1-s)$ as a function of time, during the diffusion process. Therefore, a series of compressibility experiments was performed over a period of as much as 622 hours after the beginning of bubble growth, initiated by the pressure release. Each single experiment took about 10 minutes, and can therefore be considered as "frozen". This means that we assume that the diffusion process itself is not disturbed by the successive compressibility experiments. As pointed out

	t (hours)	1−S (%)
1.	92	0.23
2.	141	0.40
3.	260	0.67
4.	357	0.93
5.	622	1.14
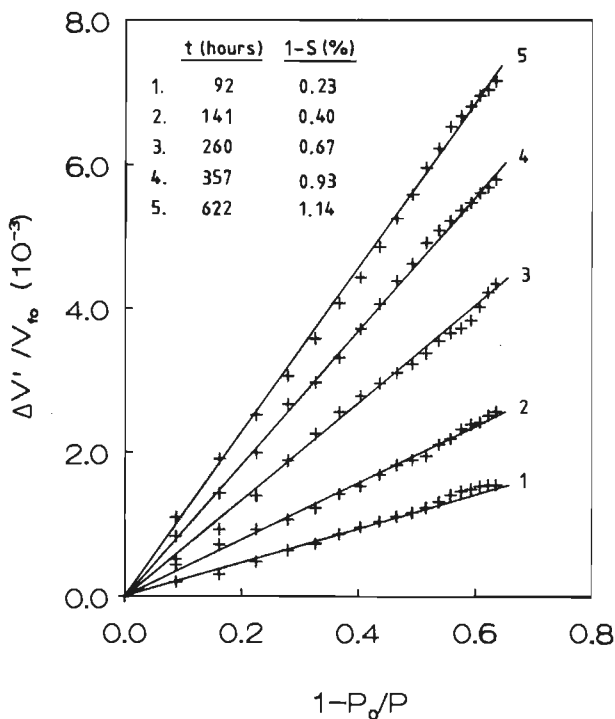
Figure 6.16: *A series of compressibility experiments performed on a partially saturated porous sand column. The reduced volume change is plotted versus the reduced pressure* $1 - p_0/p$. $t = 0$ *corresponds to the beginning of air bubble growth, due to the release of pressure. Each single experiment took about 10 minutes. After about 622 hours, a new equilibrium was reached.*

by Van der Grinten (1987, p. 64), compressibility experiments, performed on a partially saturated porous column, will no longer yield straight lines, if we plot the change in volume versus the change in pressure. We notice that, in this case, the total compressible volume V_0 consists of a liquid part V_l, and a fluid part V_f: $V_0 = V_l + V_f$, where V_f denotes the water-air mixture. The total compressibility β may therefore be written:

$$\beta = \frac{V_l}{V_0}\beta_l + \frac{V_f}{V_0}\beta_f \tag{6.32}$$

All compressibilities are defined in full analogy with (6.12). Substitution of equation (6.19) in the above equation (6.32) yields:

$$\beta = \beta_{ref} + \frac{V_f}{V_0}(1 - s)\frac{p_0}{p^2}, \tag{6.33}$$

where we have assumed $(1 - s)p_0/p \ll 1$. Furthermore, we have also taken
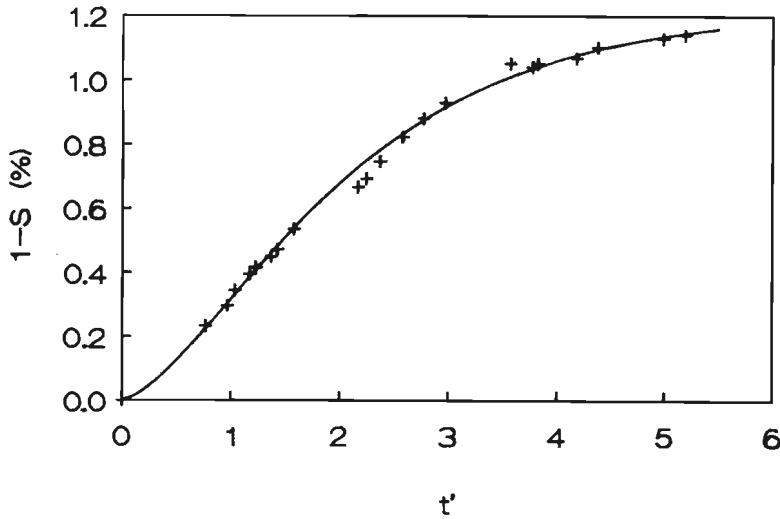
84

Figure 6.17: *Air volume fraction measurements as a function of reduced time. The drawn curve represents the theoretical curve, which is fitted by means of a least squares method. The equilibrium air volume fraction is 1.22 %.*

into account the compressibility of o-rings and silicone kit by introducing the reference compressibility β_{ref}. Integration of this equation yields:

$$\frac{\Delta V'}{V_{f0}} = (1 - s)\left(1 - \frac{p_0}{p}\right), \tag{6.34}$$

where, as usual, the index 0 refers to the initial state. In this equation, we have introduced the parameter

$$\Delta V' = V_0 - V - \beta_{ref}V_0(p - p_0)$$

In figure 6.16, $\Delta V'/V_{f0}$ has been plotted as a function of $(1-p_0/p)$. Indeed, as we expected, we find a series of straight lines, the slopes of which equal $(1 - s)$.

Once the values $(1 - s)$ are obtained during the diffusion-dominated process of bubble growth, they can be plotted against the reduced time (figure 6.17). As will be explained in the forthcoming, we are now able to deduce the mean air bubble size and concentration.
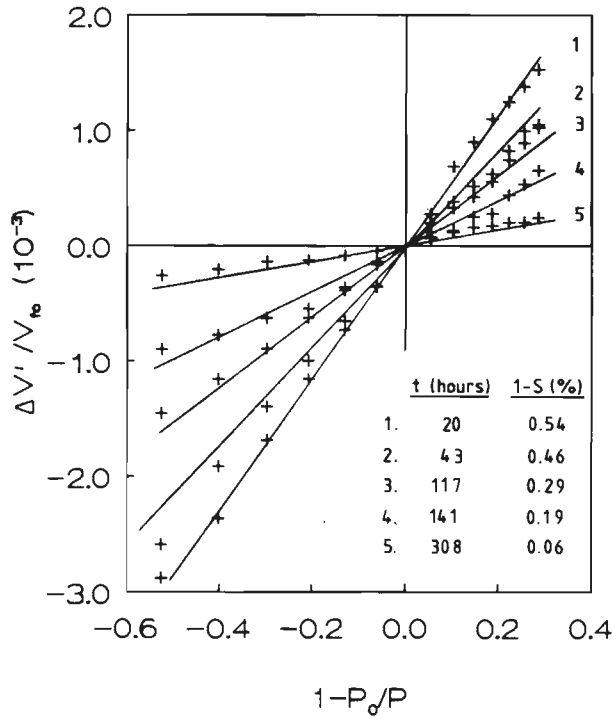
85

Figure 6.18: *A series of compressibility experiments performed on a partially saturated porous sand column. The reduced volume change is plotted versus the reduced pressure $1 - p_0/p$. $t = 0$ corresponds to the beginning of air bubble shrinkage, due to a rise of pressure. Each single experiment took about 10 minutes.*

By means of a least squares method, the measured data for $(1 - s)$ are fitted to the theoretical diffusion curve, which, in this case, is described by the equation:

$$t' = \frac{D_e t}{a^2} \; = \; \frac{1}{6\eta_\infty} \ln \frac{\eta_\infty^2 + \eta_\infty \eta + \eta^2}{(\eta_\infty - \eta)^2}$$
$$+ \; \frac{1}{\eta_\infty \sqrt{3}} \left[\frac{\pi}{6} - \arctan \frac{2\eta + \eta_\infty}{\eta_\infty \sqrt{3}} \right] \tag{6.35}$$

The result is displayed in figure 6.17. The best fitting curve is described by the parameters $a = 1.97$ cm and $\eta_\infty = 0.230$. This implies that the equilibrium air volume fraction is 1.22 %, and that the mean equilibrium air bubble radius is 0.45 cm. A further check on these parameters was obtained by a subsequent bubble shrinking experiment. The pressure was raised, and for a period of 308 hours we, again, performed compressibity experiments.
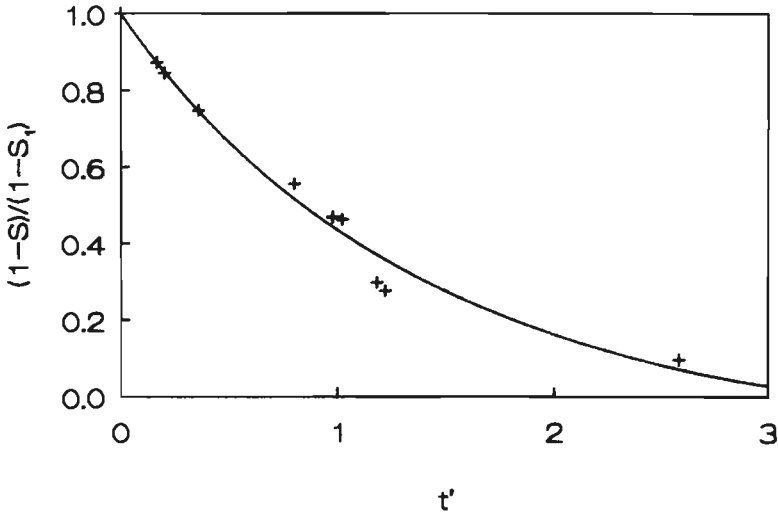
86

Figure 6.19: *air volume fraction measurements as a function of reduced time. The drawn curve represents the theoretical diffusion curve, which is fitted by means of a least squares method. Eventually, all bubbles will disappear.*

The results are presented in figure 6.18. Also in this case, we find a series of straight lines, the slopes of which equal $(1 - s)$.

The theoretical diffusion curve is now described by equation (6.29). We again searched for a best fit by means of a least squares method. In this case, we found $a = 1.95$ cm and $\eta_\infty = -0.143$, which means that the equilibrium condition is under-saturated. This result for a confirms our assumption that the location of the individual bubbles is fixed, and that their distance $2a$ is a constant. The theoretical curve and the measured air volume fractions are depicted in figure 6.19.

6.10 Air bubble distribution

For the preparation of the water-air mixture in the porous column, a super-saturation technique is used, as described in section 6.6. The size and concentration of the gas bubbles is controlled by adding some $Ca(OH)_2$ to the pore liquid. The reliability of this method was checked in optically transparant water-gelatin mixtures. In the same way as described in section 6.6, air-saturated water is prepared in a separate vessel. The amount of air dissolving in the water is controlled by the pressure in the vessel, which is higher than the atmospheric pressure. After the addition of gelatin, the pressure is released, and air bubble growth is initiated. When the equilibrium situation was reached, pictures were taken of the air bubbles trapped in the gelatin. They are presented in figures 6.20 and 6.21. Compared to destilled and tap water, the addition of $Ca(OH)_2$ results in a homogeneous distribution of small, equally sized, air bubbles.

6.11 Air bubble shape

In order to investigate the shape and the structure of the air bubbles in a porous medium, a porous disk with a diameter of 40 mm and a thickness of 5.5 mm was prepared from sintered particles of crushed glass. The diameter of the particles was about 0.5 mm. The disk was submerged in a 1.35 g/ml NaI saline solution, which has the same index of refraction as the glass particles. After the submergence of the disk, pictures were subsequently taken of the remaining air bubbles in the pores (figures 6.22 and 6.23). We find that the air bubbles commonly occupy several pores and have a ramified structure, e.g. like alveoli in the human lungs. In figures 6.23, air bubbles are pictured at atmospheric pressure p_0 (left) and at a differential pressure $p - p_0 = 1.5$ bar (right). Bubble shrinkage due to pressure increase is clearly visible.
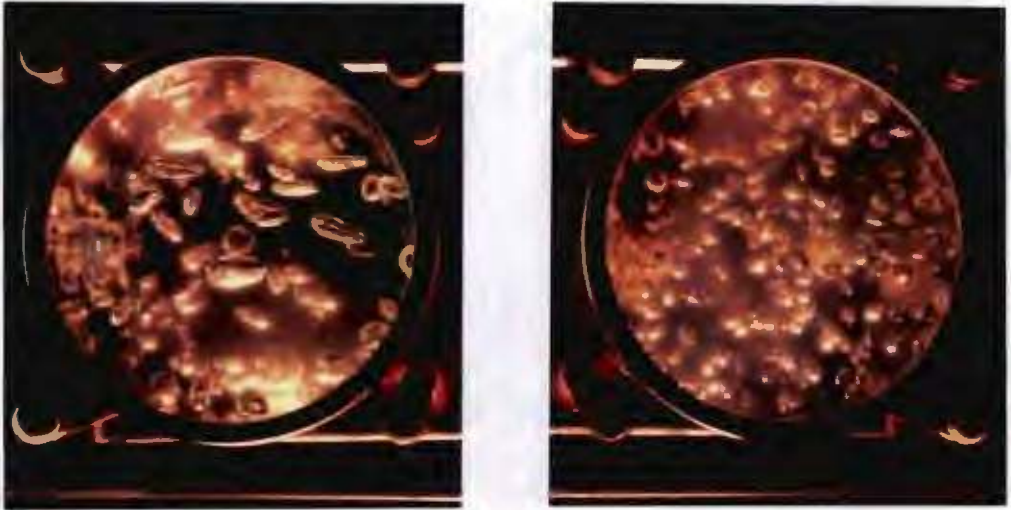
Figure 6.20: *Air bubbles in destilled (left) and tap water (right). The diameter of the vessels is 80 mm.*
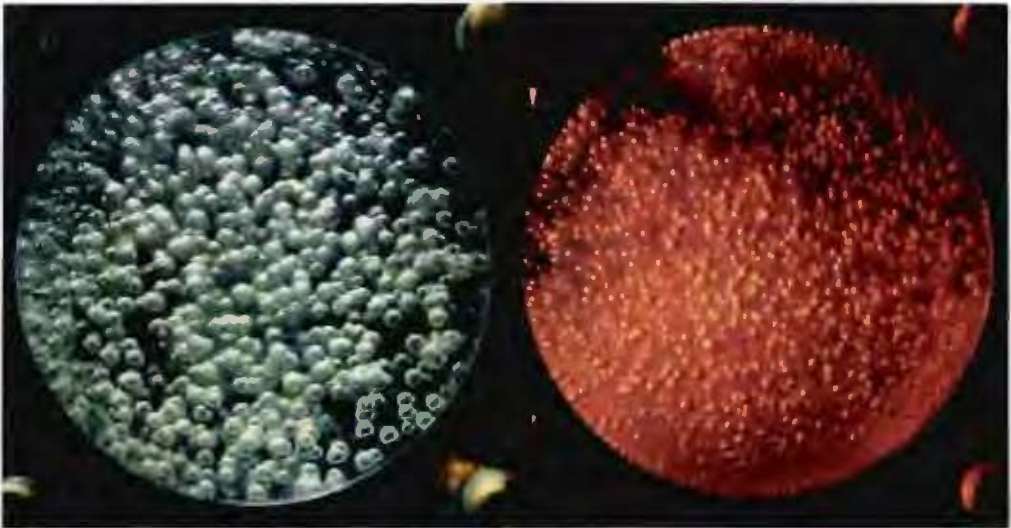
Figure 6.21: *Air bubbles in a filtered (left) and non-filtered (right) 0.5 g/l $Ca(OH)_2$ solution. The diameter of the vessels is 80 mm. The filtering has been performed by means of the sand column used in the wave experiments (see chapter 7).*

Figure 6.22: *Air bubbles in a porous medium, submerged in a 1.35 g/ml NaI saline solution. The picture covers a width of the porous medium of about 16 mm.*
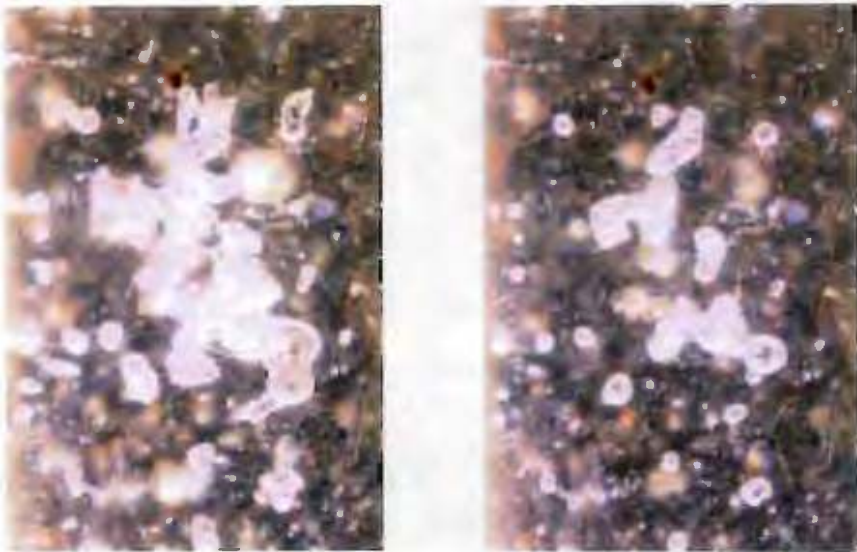
Figure 6.23: *Air bubbles in a porous medium at atmospheric pressure (left) and at a differential pressure of 1.5 bar (right). The pictures cover a width of the porous medium of about 5 mm.*

7 Wave propagation experiments

7.1 Experimental set-up

Figure 7.1: *Experimental set-up for wave propagation experiments in a porous medium. The porous medium is placed in the test section of the shock tube.*

The experimental set-up consists of a vertical shock tube with a length of about 8 m and an internal diameter of 77 mm. This set-up was described by different authors like Van der Grinten, van Dongen & van der Kogel (1985, 1987); Sniekers, Smeulders, van Dongen & van der Kogel (1989) and Smeulders, De la Rosette & 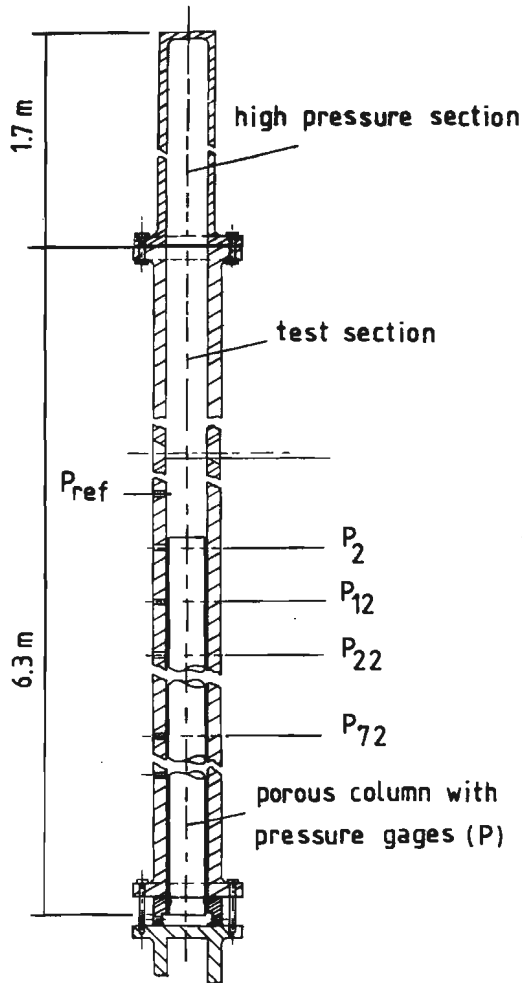van Dongen (1992). A shock tube technique for the experimental investigation of wave propagation in porous media was also used by Dontsov, Kuznetsov & Nakoryakov (1987). The set-up is drawn in figure 7.1. The shock tube sections are made out of steel with a wall thickness of 24 mm. Below, in the test section, we have placed the porous, cylindrical, test sample, which is either a Bentheim sandstone column with a diameter of 75 mm, or a sand column with a diameter of 74 mm. This implies that there is a gap of 1 - 1.5 mm in between the walls of the shock tube and the porous column, in order to prevent any shear interaction between the walls of the shock tube and the porous sample. The side walls of both samples are covered with an epoxy coating (Sigma, Colturiet TCN), in order to prevent any lateral fluid flow through the sample walls while flushing the column (see section 6.6). The properties of both porous columns are discussed in chapter 6. Both porous samples are equally equipped with 4 miniature pore pressure transducers (Druck PDCR 81, without ceramic filters), located at 2, 12, 22 and 72 cm from the top of the sample. Moreover, the sand column is also equipped with 8 dual strain gages (M-M CEA-06-125 UT-350), located at 2, 12, 22 and 82 cm from the top of the sample. At each location, two dual strain gages are attached at the opposite sides of the sample. They are used for measuring both axial and circumferential strains. Each pair constitutes the two active elements in a Wheatstone bridge, whereas the two other resistors in the bridge consist of passive strain gages outside the shock tube, used for temperature compensation. All wiring of the pore pressure transducers and the strain gages is carried down in a narrow slit in the wall of the porous column. Finally, we have the possibility to mount piezoelectric pressure gages (Kistler 603B) in the shock tube wall at various locations. One of them is always located at some distance above the porous sample (see figure 7.1), and is used for triggering the data recording system. The upper part of the shock tube is the high pressure section, which is separated from the test section by means of a thin plastic membrane. A wave experiment proceeds as follows. The porous sample is fully or partially saturated as described in section 6.6, and the pressure in the high pressure section is raised to 1.5 - 4 bar. By means of an electric current, the membrane is subsequently burned, and a stepwise pressure wave in air is generated.

A general description of the wave propagation process is given in the z-t plot of figure 7.2. We have assumed that the porous medium is fully water-saturated. For reference, the shock tube is also drawn. The shock
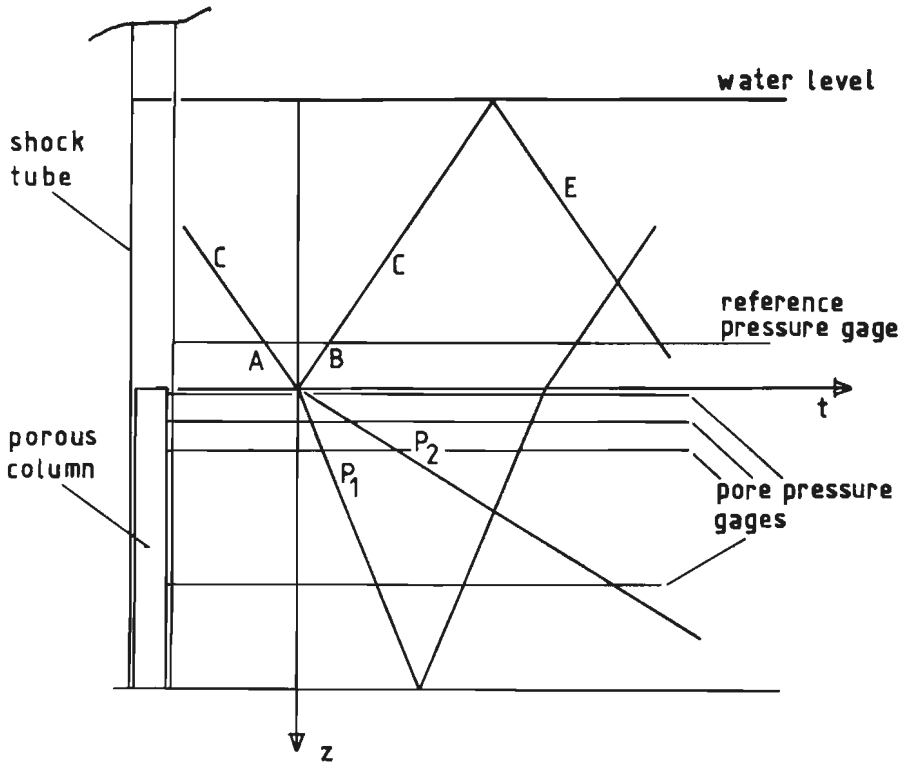
Figure 7.2: *Space-time plot of incident, reflected and transmitted waves for a water-saturated porous medium. C denotes a compression wave and E denotes an expansion wave. A and B correspond to the detection of the incident and reflected wave by the reference pressure gage P_{ref}. P_1 and P_2 are the two dilatational waves in the porous sample.*

wave in air is transmitted into the water layer on top of the porous column, where it is detected by the reference pressure gage P_{ref} (A). This triggers the data recording system. Subsequently, the wave is partially reflected from the porous column, causing a second pressure increment at P_{ref} (B). Now, the value of the pressure at P_{ref} equals the amplitude of the step loading $\hat{p}_0$ at the top of the sample at $t = 0$. When reflecting from the porous sample, the wave in the water layer generates two irrotational waves in the porous sample. They are often referred to as P (primary) - waves. The existence of both waves was theoretically predicted by Biot (1956), but it was not until 1980 that the first experimental observation of the second (slow) irrotational wave was reported (Plona 1980). Both irrotational waves are successively detected by the pressure and strain gages in the porous sample.

95

Data recording and storage takes place by means of a laboratory computer, consisting of a 5-channel transient recorder. The maximum sample rate is 1 MHz. Per channel, a 4K, 10 bit memory is available. This computer system, based on a M68000 microprocessor, was developed at Eindhoven University of Technology, Department of Applied Physics.

7.2 Water-saturated Bentheim sandstone

As far as we know, the second compressional wave has, up to now, only been observed in artificially made porous media, consisting of sintered glass beads (Plona 1980; Dontsov *et al.* 1987), or sand grains glued together by means of an epoxy resin (Van der Grinten *et al.* 1985, 1987). We shall report here the experimental results, obtained from a fully water-saturated sample of natural Bentheim sandstone. In figure 7.3a, the recorded reference pressure is shown. The shock tube generates a step-like pressure increment in air, which is transmitted into the water layer on top of the porous column, and recorded by the reference pressure gage P_{ref} at $t = -0.12$ ms. The amplitude of this step loading is denoted $\hat{p}_{in}$. This wave partially reflects from the top of the saturated porous sample, causing a second pressure increment at P_{ref} at $t = 0.12$ ms. As the distance between the top of the porous sample and the reference pressure gage is known, the velocity of sound in water may be calculated. It is found to be 1450 ± 50 m/s, which is in agreement with the literature value (1484 m/s at $20\,^{0}$C). Now, the value of the differential pressure $(p - p_0)$ at P_{ref} equals the amplitude of the step loading $\hat{p}_0$ at the top of the porous sample at $t = 0$. This value is approximately 1.3 bar. The reflection coefficient $r = \hat{p}_0/\hat{p}_{in} - 1$ is found to be 0.52 ± 0.02.

When reflecting from the top of the porous sample, the wave in the water layer generates two P-waves in the porous sample. The P_1 (fast) wave reflects from the bottom of the porous sample, and is eventually recorded by the reference pressure gage at $t \approx 1$ ms (see figure 7.3a).

The wave, which reflected from the top of the porous sample, reflects again from the water-air interface, and returns as an expansion wave. It is recorded by the reference pressure gage at $t = 1.35$ ms. This expansion wave, in its turn, reflects from the top of the porous sample, and is recorded by P_{ref} at $t = 1.61$ ms. The entire process is schematically shown in figure 7.2.

In figure 7.3b, the recorded pore pressures at 12 and 22 cm from the top of the porous sample are shown. They are denoted P_{12} and P_{22}, respectively. At both locations, we notice the arrival of the first wave, followed by a plateau. Next, there is a pressure rise, caused by the arrival of the second P-wave at $t \approx 0.16$ ms and $t \approx 0.31$ ms, respectively. From these recorded

pore pressures at the two different locations, estimates were obtained for the high frequency limits of the velocities of both P-waves. As a criterion, the propagation velocities of the foots of the wave fronts were taken. We found $c_1 = 2900 \pm 150$ m/s and $c_2 = 710 \pm 40$ m/s. Moreover, the pressure signals gave a value for the reduced pressure amplitude of the first wave $\hat{p}_{10}/\hat{p}_0 = 0.48 \pm 0.04$.
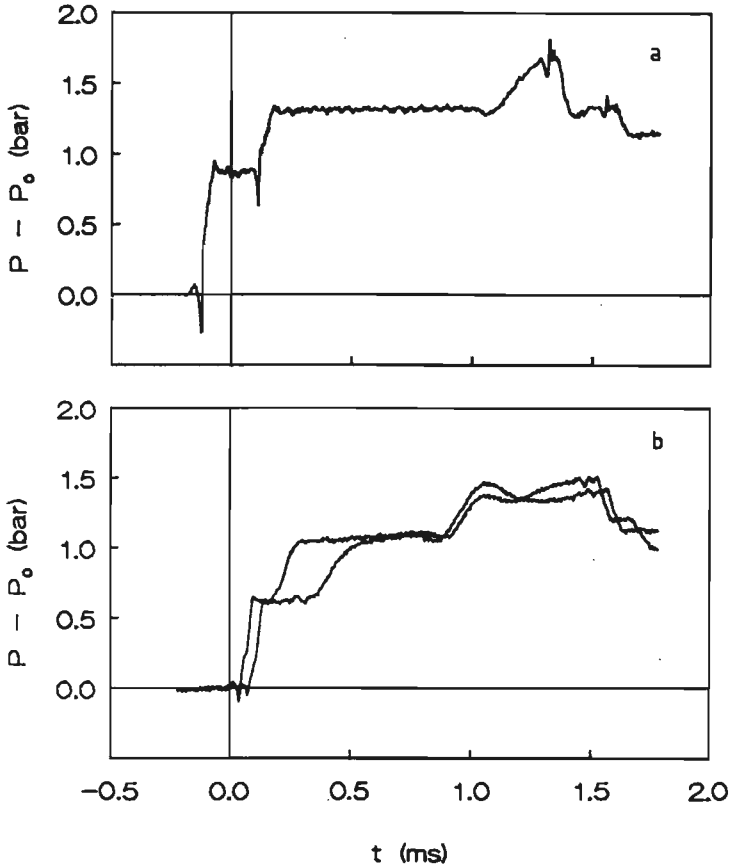

Figure 7.3: *Pressure signals for the reference pressure P_{ref} (a), and for the pore pressures P_{12} and P_{22} (b) in a water-saturated column of Bentheim sandstone. p_0 is the atmospheric pressure. Time $t = 0$ corresponds to the arrival of the pressure step $\hat{p}_0 = 1.3$ bar at the top of the sample.*

The measured values of c_1, c_2, $\hat{p}_{10}/\hat{p}_0$ and r, were subsequently fitted to the results of linear theory, described in chapter 3. We used the tortuosity α_∞ and the constrained modulus K_p as fitting parameters. As a result, we found $\alpha_\infty = 2.4$ and $K_p = 10.0$ GPa. The best fit for the tortuosity parameter α_∞ is in agreement with the value we determined in the conductivity experiment in section 6.2. The value of K_p, however, is lower than the one we found in section 6.5 (14.7 GPa). Yet, the latter value was determined for a dry sample; long periods of water exposure may very well influence the elasticity properties of the porous sample. In figure 7.4, the measured pore pressures are compared to the results from computations. Two different permeabilities, $k_0 = 3.7$ D and $k_0 = 18.0$ D, have been taken into account. Here, we have introduced the Darcy (D) unit, which is approximately equal to 10^{-12} m^2. We find that the independently determined permeability value (see section 6.3) $k_0 = 3.7$ D, does not adequately describe the diffusive pressure rise of the second dilatational wave. The value $k_0 = 18.0$ D, on the other hand, gives a nice fit for the pore pressure signals at both 12 and 22 cm. From straightforward considerations, presented in appendix B, it follows that wave propagation properties are seriously affected by the presence of the gap between the shock tube wall and the porous sample. Compared to the elastic properties of water, the epoxy coating of the cylinder wall is a flexible membrane, which cannot sustain any pressure differences. This means that there is a complicated interaction process between the pore fluid and the gap fluid, which may very well affect the measured permeability value of the porous sample. In case the pore fluid consists of a water-air mixture, the compressibility of the pore fluid far exceeds the compressibility of the liquid in the gap. Also in this case, wave propagation and damping in the porous sample may be affected by the liquid-filled gap. This is discussed in appendix B.

7.3   Water-saturated sand

Wave experiments, performed on a fully water-saturated sand column have been reported by Van der Grinten *et al.* (1985, 1987). They found phase velocities $c_1 = 2190 \pm 90$ m/s and $c_2 = 790 \pm 20$ m/s.

For the pressure amplitude of the first wave $\hat{p}_{10}/\hat{p}_0$, a value of 0.59 ± 0.03 was reported. These measured values were subsequently fitted to the computational results from linear theory. Again, α_∞ and K_p were used as fitting parameters. They found $\alpha_\infty = 1.45$ and $K_p = 4.5$ GPa. These values are obviously not in agreement with the values, which we determined in sections 6.2. and 6.5, respectively ($\alpha_\infty = 2.7 \pm 0.2$ and $K_p = 10.2 \pm 0.2$ GPa). Some remarks can be made about these discrepancies. There are indications that
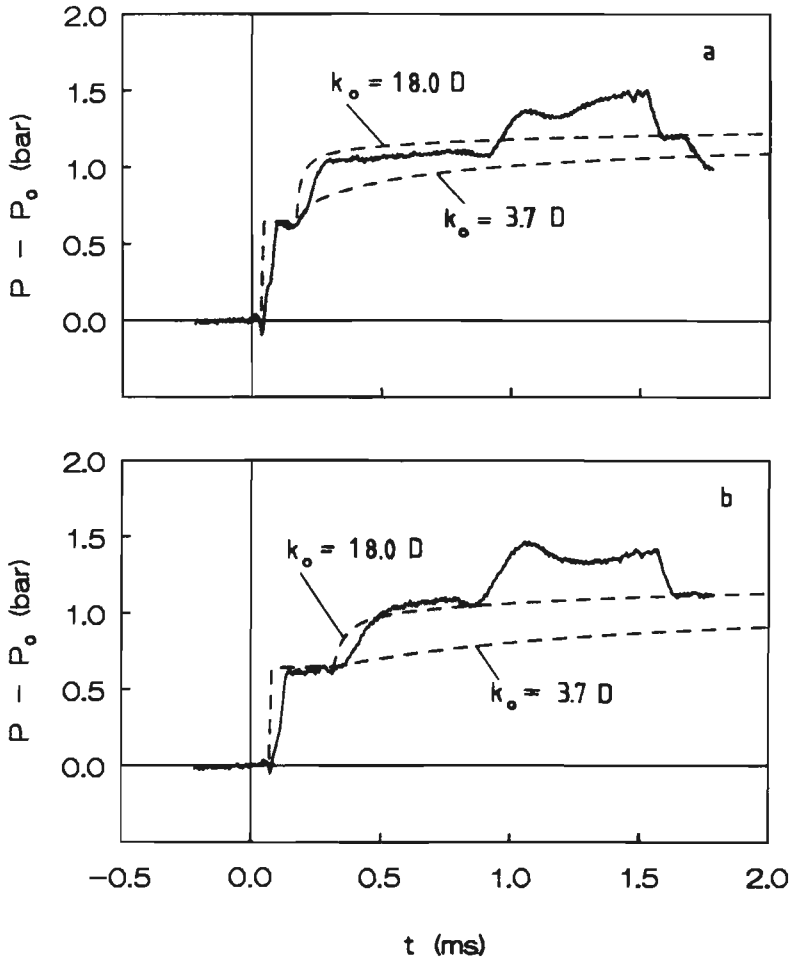
Figure 7.4: Pore pressure signals, recorded at 12 cm (a) and 22 cm (b) from the top of a water-saturated Bentheim sandstone column. The dashed lines represent the computational results from linear theory. The computations are performed for two different k_0 values, and for $K_p = 10$ GPa, $\phi_0 = 0.23$ and $\alpha_\infty = 2.4$. We have introduced the Darcy (D) unit for the steady-state permeability. A definition is given in the text.

water absorption of the resin influences the elastic properties of the porous column. For the epoxy resin, we determined the moduli of Young E_1 before, and E_2 after 48 days of water immersion. This was done by means of a tensile test. We found $E_1 = 0.6 \pm 0.05$ GPa and $E_2 = 0.18 \pm 0.05$ GPa. The water absorption thus causes a decrease of Young's modulus by more than a factor 3.

The tortuosity parameter α_∞ may be affected by the liquid-filled gap between the sample and the shock tube walls. This is qualitatively discussed in appendix B.

7.4   Partially saturated sand

In this section, we will discuss wave experiments, performed on a partially saturated sand column. The column consists of sand grains in the range 0.3-0.6 mm, which are glued together by means of an epoxy resin (Scotchcast, 3M electrical resin 8, 5236). Details of the preparation of a water-air mixture and the determination of the mean air bubble size and concentration can be found in sections 6.6 - 6.9. Once we have prepared a water-air mixture of specific mean air bubble radius R and gas volume fraction $(1 - s)$, these experimental conditions may easily be altered by changing the ambient pressure in the test section of the shock tube (see figure 7.1). If the pore fluid is, for example, subjected to an ambient pressure increase Δp_1, the mean air bubble radius and the gas volume fraction will both decrease. This process may be considered "frozen", if Δp_1 is applied for a time interval τ_1, which is short enough to ensure that almost no air from the bubbles is dissolved in the liquid. With the results from section 6.7, the "frozen" gas volume fraction and mean air bubble radius may then be calculated.

The wave experiments, performed on a partially saturated sand column, will now be discussed both in the time domain and in the frequency domain.

7.4.1   Time domain

The immense influence of a minor gas volume fraction on wave propagation, as was theoretically described in chapter 4, is also distinctly visible in our experiments. In figure 7.5, we have plotted two pore pressure signals, recorded at 12 cm from the top of the porous sample. One of the signals was recorded in a fully water saturated column. The other signal corresponds to a pore fluid, consisting of a water-air mixture with a gas volume fraction of only 0.12 %. For the fully saturated sand column, the two P-waves can clearly be recognized in the recorded pressure signal. This was also found by Van der Grinten *et al.* (1985, 1987). We notice the sudden pressure rise at
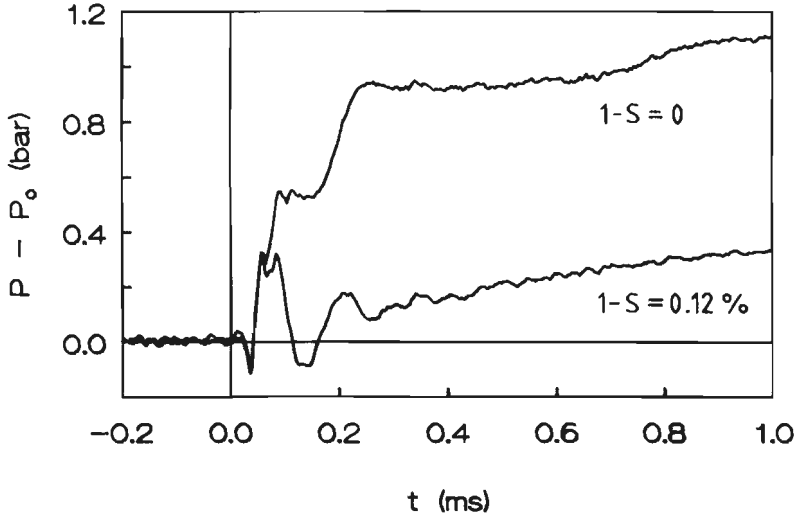
Figure 7.5: *Pore pressure signals for a fully water-saturated case and for a pore fluid consisting of a water-air mixture with a gas volume fraction of 0.12 %. Time $t = 0$ corresponds to the arrival of the incident pressure step $\hat{p}_{in} = 0.8$ bar at the top of the sample.*

the arrival of the first dilatational wave, followed by a more gradual pressure rise at the arrival of the second, dispersive, wave. When there is a gas volume fraction of only 0.12 % in the pores, this two step structure completely disappears. Instead, an oscillatory pore pressure signal is recorded, followed by a gradual pressure rise. We also notice that this gradual pressure rise commences from a certain offset value, which is about 0.1 bar in this case.

Figure 7.6: *Experimental and theoretical pore pressure signals at 12 cm from the top of the porous sample. $t = 0$ corresponds to the arrival of the incident pressure step $\hat{p}_{in} = 0.8$ bar at the top of the sample. The gradual pressure rise commences at a certain offset value. For higher $(1 - s)$ and R values, the offset value and the gradual pressure rise both decrease.*
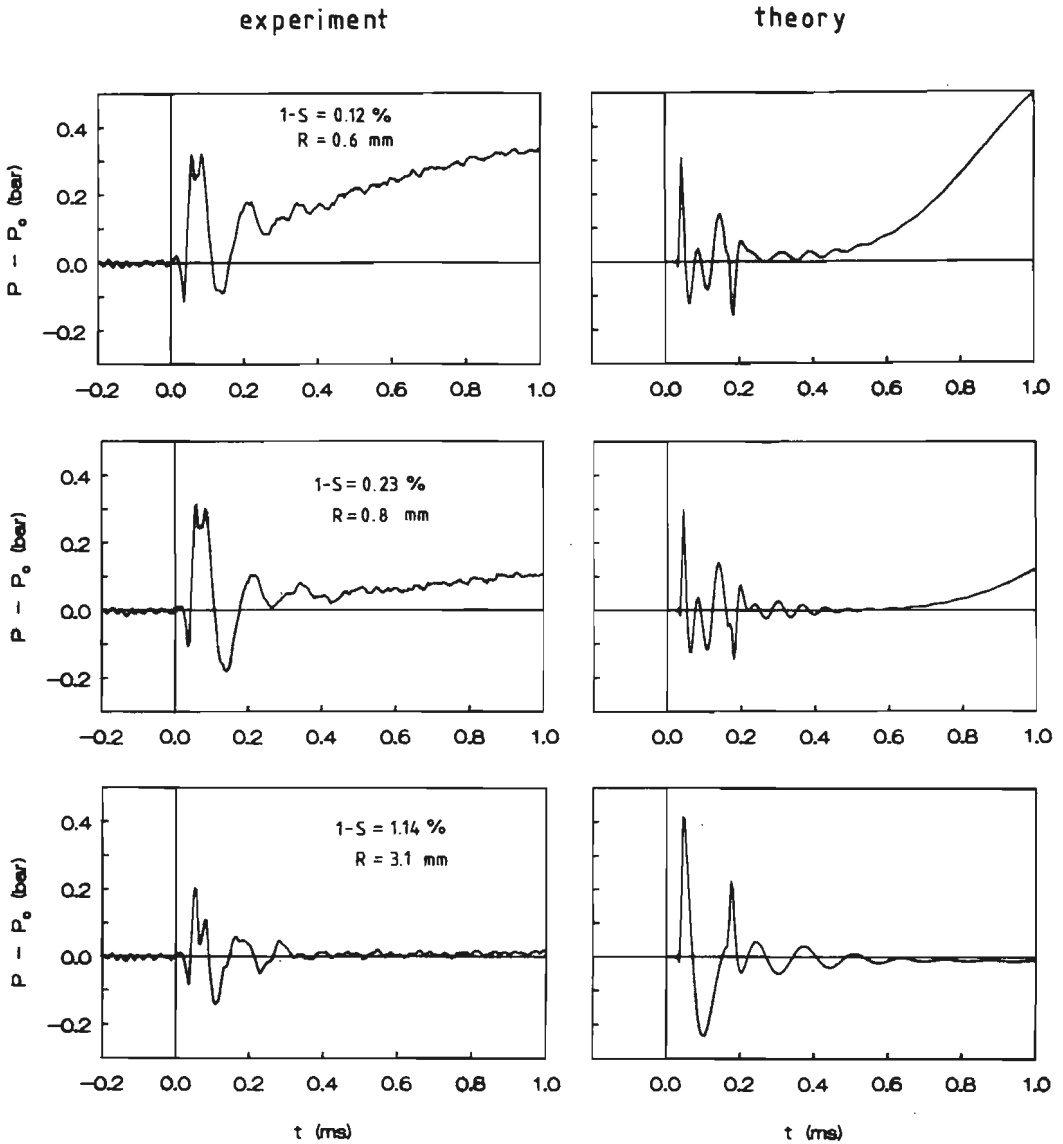
In figure 7.6, we have indicated what happens when the gas volume fraction $(1 - s)$, and the corresponding mean air bubble radius R, are increased further. We notice that the offset pressure value gradually diminishes. We also find that the long-term pressure rise becomes less, and, finally, is no longer visible on our time scale.

In figure 7.6, we have also plotted the corresponding theoretical pore pressures. The computed pore pressure signals indeed display an oscillatory behaviour. A Fourier analysis of recorded and computed oscillations is discussed in the next section. The diffusive pressure rise is also found from computations, and, indeed, diminishes for higher gas volume fractions and gas bubble radii. However, there are still some discrepancies between the amplitudes of the recorded and computed pore pressure signals.

7.4.2 Frequency domain

The recorded pore pressure signals have been analysed in the frequency domain by means of straightforward Fourier analysis. From theoretical considerations, presented in chapter 4, we found that a change of the ambient pressure in the test section does not so much alter the frequency spectra. That is because the effect of a "frozen" change in $(1-s)$ is, at least partially, undone by the corresponding "frozen" change in R. We therefore prepared three different water-air mixtures in the way that was described in section 6.6. From successive compressibility experiments, we determined mean air bubble size and concentration (see sections 6.7 - 6.9).

The results were: a. $(1 - s) = 1.14\%$, $R = 3.1$ mm; b. $(1 - s) = 1.09\%$, $R = 1.6$ mm; c. $(1 - s) = 0.66\%$, $R = 2.9$ mm. Subsequently, in each case, a series of wave experiments was performed. Fourier spectra of the recorded pore pressure signals at 22 (a), 12 (b) and 22 cm (c) from the top of the porous column are presented in figures 7.7. We notice that the pore pressures are in different ranges for all three cases, which allows a comparison between experimental and theoretical data for a total differential pressure range of 0-8 mbar. The experiments display a remarkable two peak structure. Two separate frequency bands, with corresponding frequency maxima, are clearly visible. In the forthcoming, the location of the maximum of the first frequency band is denoted ω_1, and the location of the maximum of the other frequency band is denoted ω_2. The separate frequency bands correspond to the two Biot wave modes, as was discussed in chapter 4.

In the same figure 7.7, theoretical curves are also drawn. Pore pressures have been computed with, and without including the acoustic damping mechanism. In all three cases, the amplitudes of both frequency maxima are in agreement with the theoretical values, if the acoustic damping mechanism

is omitted. Including the acoustic damping in the way it was presented in section 4.4, will apparently overestimate its importance.

Experimental and theoretical values for ω_1 and ω_2 are presented in table 7.1. We find that, in all three cases, the experimental ω_1 values are in good agreement with the theoretical values, whereas this is not the case for the ω_2 values. This may be caused by gas bubble inhomogeneities, as the ω_2 values are particularly sensitive to a small variation in mean gas bubble radius. Another possible reason is the lateral interaction effect between the pore fluid and the liquid in the gap between the porous sample and the shock tube walls (see appendix B). From table 7.1, we also find that a decrease in mean gas bubble radius R will cause an increase of both ω_1 and ω_2. A decrease in gas volume fraction, however, acts in the opposite direction.

	a	b	c
1-s (%)	1.14 ±0.02	1.09 ±0.02	0.66 ±0.02
R (mm)	3.1 ±0.1	1.6 ±0.1	2.9 ±0.1
experimental ω_1 (10^5 rad/s)	0.38 ±0.04	0.72 ±0.04	0.33 ±0.04
theoretical ω_1 (10^5 rad/s)	0.36	0.69	0.30
experimental ω_2 (10^5 rad/s)	0.87 ±0.05	1.86 ±0.08	0.91 ±0.05
theoretical ω_2 (10^5 rad/s)	0.58	1.07	0.47

Table 7.1   Comparison between experimental and theoretical values of the maxima of the Fourier spectra.
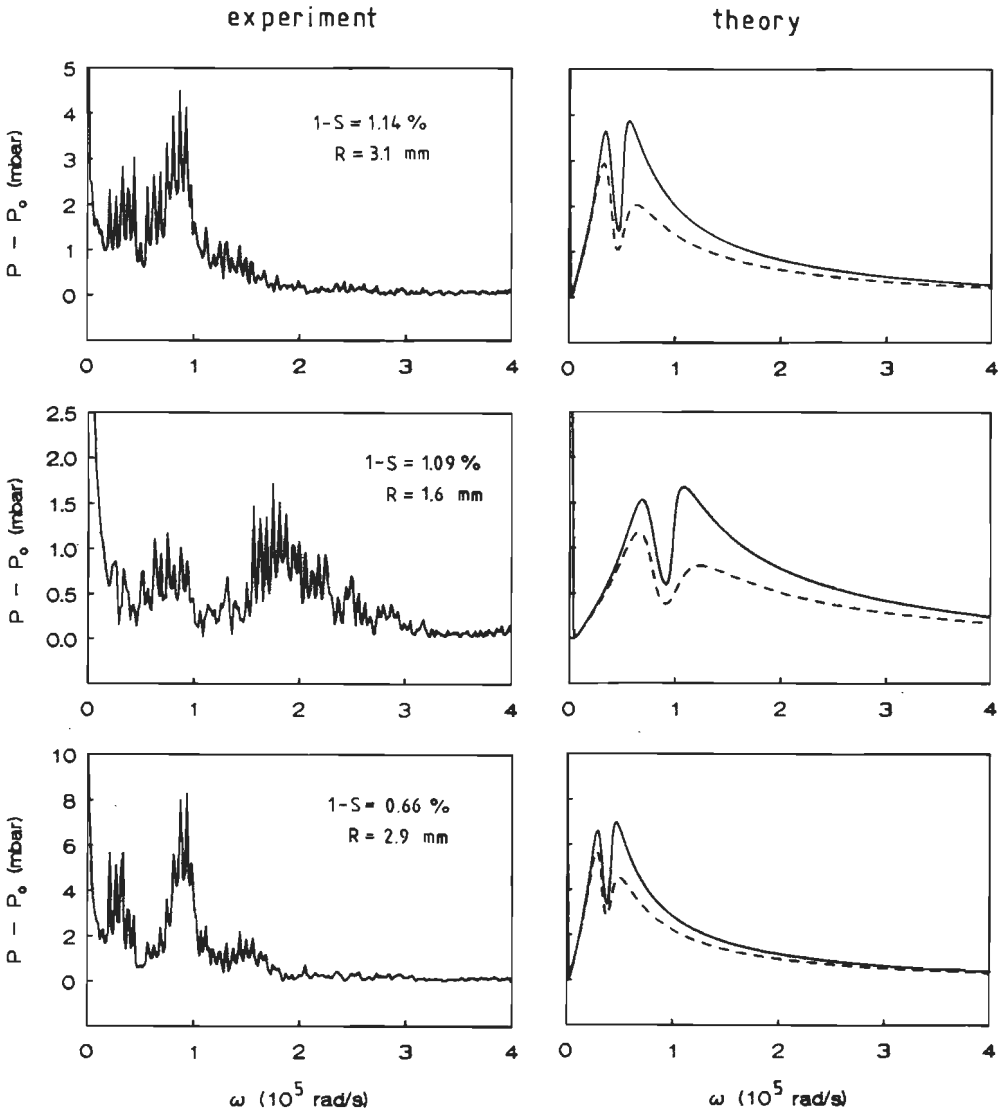
Figure 7.7: *Power spectra of recorded and computed pore pressure signals. Pore pressure signals have been computed with (dashed lines), and without (drawn lines) including the acoustic damping mechanism. Two separate frequency bands are detected, corresponding to the two Biot wave modes.*

7.5 Partially saturated Bentheim sandstone

Preliminary experiments were performed on a partially saturated Bentheim sandstone column. An experimental result is shown in figure 7.8. Also in this case, the expected oscillatory behaviour is recorded, and the diffusive long-term pressure rise is visible. Comparison with computed pore pressure signals is a point for future investigation.
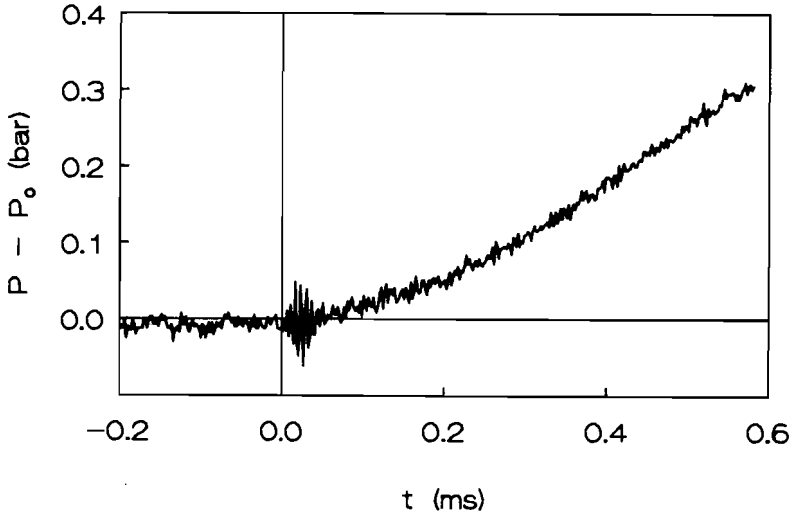

Figure 7.8: *Recorded pore pressure signal in a partially saturated Bentheim sandstone column at a depth of 2 cm. The air volume fraction is 0.48 %. Time $t = 0$ corresponds to the arrival of the incident pressure step $\hat{p}_{in} = 0.8$ bar at the top of the sample.*

8 Conclusions

In this chapter, we will summarize the results of the experimental and theoretical studies of the previous chapters. These studies were performed for fully saturated and partially saturated porous media. Particular attention was paid to oscillating gas bubbles in porous media; the way they are damped, and the way in which they affect wave propagation phenomena. For the wave experiments, we used a sand column, consisting of glued sand particles, and a natural Bentheim sandstone column. The results of the studies allow some conclusions to be drawn.

In order to perform well-defined wave experiments on partially saturated porous media, a homogeneous water-air mixture in the pores was prepared, using a super-saturation technique. By means of a series of successive compressibility experiments, both mean gas bubble radius and concentration can be determined. These pore fluid properties can easily be varied by altering the ambient pressure conditions. In this way, wave experiments can be performed for different experimental conditions.

The presence of even a small gas volume fraction in the pores largely influences wave propagation, reflection and damping phenomena. Instead of the distinct two-step structure of the fully saturated case, an oscillatory pore pressure behaviour is observed. The propagation velocity of this oscillation is about the same as the phase velocity of the first Biot wave mode in the fully saturated case. On a longer time scale, the oscillation is followed by a gradual diffusive pressure rise.

Straightforward Fourier analysis of the oscillatory pressure signals shows two distinct frequency bands, which were also theoretically predicted. They correspond to the two Biot wave modes. From the damping-versus-frequency plot, we find, indeed, that there exist two frequency bands, where low damping coefficients occur. A partially saturated porous media obviously acts as a frequency band filter; some frequency bands are easily transmitted into the porous medium, and have low damping factors and high phase velocities.

The experimental data from wave propagation experiments were compared to linear one-dimensional theory. The effect of oscillating gas bubbles in the porous media was represented by a dynamic, i.e. frequency dependent, fluid bulk modulus, which was incorporated in the Biot theory. When the gas bubbles are vibrating in phase with the exerted pressure in the sur-

rounding liquid, the pore fluid becomes very compressible. When, on the other hand, the gas bubbles are vibrating out-of-phase, i.e an increase in the liquid pressure causes the gas bubbles to expand, the pore fluid compressibility is very low.

The oscillating gas bubbles in a partially saturated porous medium, are damped by thermal, viscous, Darcy and acoustic mechanisms. Of these four, the Darcy damping mechanism is by far the most important one. It is caused by the dynamic interaction between the pore fluid and the porous material. This dynamic interaction was experimentally investigated in a separate set-up, in which a low-frequency oscillating liquid flow was induced in a fully saturated, rigid, porous medium. This was done, using an exciter-driven frictionless piston. By means of scaling the size of the grains of the porous samples, experiments could be performed for a reduced frequency range, which was the same as for the shock tube wave experiments. The measurements of the so-called dynamic permeability, or dynamic tortuosity, were in agreement with a scaling function over the full frequency range. For low frequencies, the viscous effects are dominant, whereas in the high frequency range the inertial effects prevail. In between there is a transition region, characterized by a so-called rollover frequency. The viscous effects are characterized by the steady-state permeability; the intertial effects by the tortuosity parameter.

This dynamic behaviour can be described on the basis of a two-scale homogenization formalism. In this way, it is possible to derive new expressions for the real and imaginary parts of the dynamic tortuosity. These are exact results, applicable over the entire frequency range. It is shown that in the high frequency limit, when the viscous boundary layers are small compared to the size of the pores, we may describe the macroscopic permeability by two parameters α_∞ and Λ, characterizing the microscopic pore geometry properties. We also find that it is possible to calculate Λ in two different ways, yielding the same result within limits of accuracy.

Over the entire frequency range we found that the reduced dynamic permeability is a function of, at least, two parameters. The first is the rollover frequency, we mentioned before, and the other is a similarity parameter M. From numerical computations for several pore geometries, we found that $M \approx 1$, although we observed deviations up to 20 % for strongly curved pore geometries.

The acoustic damping mechanism is found to be overestimated, in case we assume that all energy from an oscillating gas bubble is freely radiated into the surrounding, infinitely extended, compressible pore fluid. There is obviously reflection of energy from the walls of the porous sample, which does not contribute to the energy dissipation of the system. A more detailed

study of this phenomenon is a point for future investigation.

For the fully water-saturated sand, both the "in-phase" and the "out-of-phase" wave modes were already observed previously. In the present study, both waves are also recorded in a natural Bentheim sandstone. In the latter case, the measured wave speeds and pressure amplitudes for both wave modes are fitted to linear, one-dimensional theory, with the constrained modulus and the steady-state permeability as fitting parameters. We find that these fitted values differ significantly from the expected values. This may be caused by several reasons. The discrepancy in the constrained moduli may be caused by water absorption by the porous material, which may change the elastic properties of the porous skeleton. The same effect was also found for the fully saturated sand column, where we measured that a reduction by a factor 3 of Young's modulus of the epoxy resin was caused by a water immersion of 48 days.

Another factor of importance is the presence of a liquid-filled gap between the porous sample and the shock tube walls. For a rigid porous material, it is shown that the interaction between the liquid in the gap and the pore fluid may be represented in one-dimensional theory by a lower tortuosity value and a higher value for the steady-state permeability. This tortuosity effect was, indeed, observed for the saturated sand column, whereas the permeability effect was observed for the Bentheim sandstone. A detailed quantitative description could not not be given due to the fact that the elastic motion of the porous material was not taken into account.

For the partially saturated cases, the compressibility of the pore fluid far exceeds the compressibility of the liquid in the gap. Also in this case, however, there are indications that the influence of the gap can not be neglected. When the power spectra of the recorded pore pressure signals are compared to the results from a theoretical analysis, a good agreement is reached only in the case that the "effective" tortuosity and constrained modulus are taken into account.
As we expected, we find that the frequeny band, corresponding to the second Biot wave mode, is especially sensitive to a variation in the tortuosity parameter.

Appendix A

Computation of Λ_1

In order to calculate the real part of the frequency dependent tortuosity $\alpha(\omega)$, we have assumed the potential flow solution to be bounded by the actual pore walls, thus neglecting viscosity effects and therefore introducing an error of $O(\delta)$. We shall now present a more detailed analysis to actually calculate the error under consideration, by linking the actual pore velocity u_0 to a potential flow solution $u_p = -\nabla_y \psi$. We shall choose ψ in such a way that the flow rate Q_0, corresponding to the velocity distribution u_0 equals the flow rate Q, corresponding to the potential flow velocity distribution u_p. We shall introduce the pore wall shift as a potential flow modifying factor.

A velocity u'_0 is defined in such a way that u'_0 equals u_0 everywhere except in the viscous boundary layer where u'_0 has a fixed value $u'_{0\delta}$:

$$\int |u_0|^2 dV = \int |u'_0|^2 dV + \int (|u_0|^2 - |u'_0|^2) dV \tag{A.1}$$

The second part of the right hand side of the above equation is zero, except in the boundary layer. Substituting the boundary layer velocity distribution:

$$u_0 = u'_{0\delta}[1 - e^{-ik\beta}] \tag{A.2}$$

and integrating the second part of the right hand side of eq.(A.1) we arrive at:

$$\int |u_0|^2 dV = \int |u'_0|^2 dV - \frac{\delta}{2} \int |u'_{0\delta}|^2 dS, \tag{A.3}$$

where the integration in the second part of the right hand side is over the pore-grain interface surface. Next, aiming to link u'_0 to the previously defined potential flow solution u_p, we note that, at constant flow rate, the presence of a viscous boundary layer of thickness δ will cause the non-viscous velocity modulus $|u_p|$ in the whole of the pore to be lower than $|u'_0|$. Taking this into consideration, we write the squared velocity modulus $|u'_0|^2$ as a Taylor series:

$$|u'_0|^2 = |u_p|^2 + \Delta r [\frac{\partial}{\partial r} |u_p|^2]_Q + \dots, \tag{A.4}$$

where Δr is some virtual outward displacement of the pore walls at constant flow rate and $\frac{\partial}{\partial r}G$ denotes the derivative of some quantity G with respect to this virtual displacement. To emphasize the derivative is at constant flow rate, the subscript Q is added.

In order to estimate the value of Δr, we will compare the velocity distribution $\mathbf{u}'_0$ to the actual velocity distribution $\mathbf{u}_0$. We notice that the presence of the viscous boundary layer will introduce a small, complex valued, flow rate difference $Q_\delta = Q'_0 - Q_0$, where Q'_0 is the flow rate corresponding to the velocity distribution $\mathbf{u}'_0$. As $|Q_\delta| \ll |Q'_0|$, we may write a first order approximation for $|Q_0|$:

$$|Q_0| \approx |Q'_0| - \mathcal{R}e \int (\mathbf{u}'_0 - \mathbf{u}_0).\mathbf{n}d\beta dl, \qquad (A.5)$$

where l is a circumferential coordinate perpendicular both to the pore wall surface and the boundary layer velocity. Furthermore, $\mathbf{n}$ is the normal vector defining the surface element $d\beta dl$. Substitution of eq.(A.2) into eq.(A.5) yields:

$$|Q_0| \approx |Q'_0| - \frac{\delta}{2} \oint \mathbf{u}'_{0\delta}.\mathbf{n}dl. \qquad (A.6)$$

The second part of the right hand side of the above equation can be interpretated as a virtual shifting of the pore walls over a distance $-\delta/2$. By definition we may write $Q = Q_0$ and we may therefore conclude $\Delta r = -\delta/2$.

Now integrating eq.(A.4) over the pore volume we arrive at:

$$\int |\mathbf{u}'_0|^2 dV = \int |\mathbf{u}_p|^2 dV - \frac{\delta}{2}[\frac{\partial}{\partial r}\int |\mathbf{u}_p|^2 dV]_Q + \frac{\delta}{2}\int |\mathbf{u}_{pw}|^2 dS. \qquad (A.7)$$

In equation (A.3) we may replace $\mathbf{u}'_{0\delta}$ by the potential flow velocity at the wall $\mathbf{u}_{pw}$ without loss of accuracy, i.e. accepting an error of $O(\delta^2)$. This is easily seen by writing $|\mathbf{u}'_{0\delta}|^2$ as a Taylor series also. Subsequent substitution of eq.(A.7) into eq.(A.3) yields a relation between the actual pore velocity distribution $\mathbf{u}_0$ and the potential flow velocity distibution $\mathbf{u}_p$:

$$\int |\mathbf{u}'_0|^2 dV = \int |\mathbf{u}_p|^2 dV - \frac{\delta}{2}[\frac{\partial}{\partial r}\int |\mathbf{u}_p|^2 dV]_Q. \qquad (A.8)$$

Dividing the entire equation (A.8) by the pore volume V_p and by the squared macroscopic velocity modulus $|\mathbf{v}_0|^2$, we find that the left hand side of the above equation is the real part of the dynamic tortuosity $\mathcal{R}e(\alpha)$, and that the first term of the right hand side is the extreme high frequency limit of the dynamic tortuosity α_∞. From eq.(A.8) we write:

$$\mathcal{R}e(\alpha) = \alpha_\infty[1 + \frac{\delta}{2}\frac{2}{\Lambda_1}], \qquad (A.9)$$

111

where the parameter Λ_1 has the dimension of length and is given by:

$$\frac{2}{\Lambda_1} = \frac{-[\frac{\partial}{\partial r} \int |\mathbf{u}_p|^2 dV]_Q}{\int |\mathbf{u}_p|^2 dV} \tag{A.10}$$

Equation (A.10) offers the opportunity for numerical computation of the value of Λ_1, by shifting the pore walls while maintaining constant flow rate by adapting the flow potential difference $\Delta\psi$ between two equipotential surfaces. This rather laborious procedure may be simplified considerably writing

$$-[\frac{\partial}{\partial r} \int |\mathbf{u}_p|^2 dV]_Q = [\frac{\partial}{\partial r} \int |\mathbf{u}_p|^2 dV]_{\Delta\psi} \tag{A.11}$$

The differentiation at constant flow rate has now been replaced by a more convenient differentiation at constant flow potential difference. We shall prove (A.11), considering an incompressible flow at microscale:

$$\nabla_y.(\psi \nabla_y \psi) = |\mathbf{u}_p|^2 \tag{A.12}$$

Integration over the pore volume and application of Gauß' theorem yields:

$$\oint \psi(\mathbf{u}_p.\mathbf{n})dA = \int |\mathbf{u}_p|^2 dV, \tag{A.13}$$

where A is the integrating surface consisting of pore wall surfaces and two arbitrary bounding equipotential surfaces. Furthermore, $\mathbf{n}$ is the normal vector defining such surface element dA. As we have $\mathbf{u}_p.\mathbf{n} = 0$ at the pore wall surfaces, we arrive at:

$$\int |\mathbf{u}_p|^2 dV = Q\Delta\psi \tag{A.14}$$

We now proceed taking the derivative with respect to r of (A.14) at constant flow rate:

$$[\frac{\partial}{\partial r} \int |\mathbf{u}_p|^2 dV]_Q = Q[\frac{\partial \Delta\psi}{\partial r}]_Q = -Q\frac{[\frac{\partial Q}{\partial r}]_{\Delta\psi}}{[\frac{\partial Q}{\partial \Delta\psi}]_r} \tag{A.15}$$

At constant r, i.e. not changing the pore geometry we may write:

$$[\frac{\partial Q}{\partial \Delta\psi}]_r = \frac{Q}{\Delta\psi} \tag{A.16}$$

By substitution of (A.16) into (A.15), we finally arrive at (A.11).

Appendix B

The influence of a liquid-filled gap on wave propagation in rigid porous media

In this appendix, we will give a qualitative survey of the influence of the gap between the porous sample and the shock tube walls on wave propagation in a liquid-filled, rigid, porous medium. This obviously means that only the second Biot wave mode is considered. The configuration is drawn in figure B.1. The area marked 1 in the figure, corresponds to a liquid-filled gap; the area marked 2, is the liquid-saturated porous medium. The components in
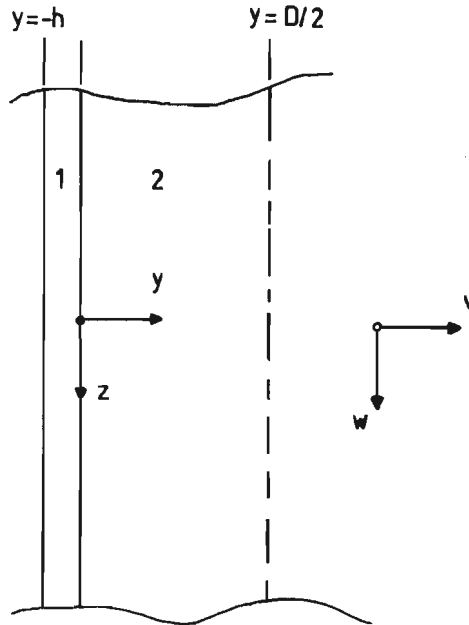

Figure B.1: *Configuration and axes used in computations. The area 1 corresponds to a liquid-filled gap; the area 2 is the liquid-saturated porous medium. v and w are the components of the displacement vector in the y and the z direction, respectively.*

the y and in the z direction of the fluid displacement vector $\mathbf{U}_i$ are denoted v_i and w_i, respectively. The index $i = 1, 2$ corresponds to the areas in figure B.1. We may define the displacement potentials Φ_1 and Φ_2, such that $v_i = \partial \Phi_i / \partial y$ and $w_i = \partial \Phi_i / \partial z$. The dynamic fluid equations then become:

$$\nabla^2 \Phi_1 = \frac{1}{c_l^2} \ddot{\Phi}_1 \tag{B.1}$$

$$\phi_0 K_l \nabla^2 \Phi_2 = \rho_{22} \ddot{\Phi}_2 + b_0 \dot{\Phi}_2, \tag{B.2}$$

where the dot denotes a derivation with respect to time. The velocity of sound in the liquid is called c_l, and the density ρ_{22} is defined in section 2.4. For the fluid pressures we may write:

$$p_i = -K_l \nabla^2 \Phi_i \tag{B.3}$$

The boundary conditions are:

$$y = 0: \qquad p_1 = p_2$$
$$\phi_0 \dot{v}_2 = \dot{v}_1 \quad \text{(continuity of filtration velocity)}$$

$$y = -h: \qquad v_1 = 0$$
$$y = D/2: \qquad v_2 = 0$$

If an exponential solution for both Φ_1 and Φ_2 is substituted in equations (B.1) and (B.2), we find:

$$\Phi_1 = \left(A e^{-qy} + B e^{qy} \right) e^{i(\omega t - \kappa z)} \tag{B.4}$$

$$\Phi_2 = \left(C e^{-sy} + D e^{sy} \right) e^{i(\omega t - \kappa z)}, \tag{B.5}$$

where A, B, C and D are arbitrary constants and κ is the wave number. Furthermore, $q = \sqrt{\kappa^2 - \kappa_l^2}$ and $s = \sqrt{\kappa^2 - \kappa_\alpha^2}$, where κ_α is the wave number for $h \equiv 0$ (no gap). We may write:

$$\kappa_\alpha^2 = \alpha_\infty \omega^2 \frac{\rho_f}{K_f} - \frac{i \omega b_0}{\phi_0} K_f \tag{B.6}$$

Substitution of both equations (B.4) and (B.5) in the boundary conditions yields, after some algebraic manipulations, an expression for the wavenumber κ:

$$- \phi_0 \, \kappa_l^2 \, s \tanh(\frac{1}{2} D s) = \kappa_\alpha^2 \, q \tanh(qh) \tag{B.7}$$

In first approximation, we may write $\tanh(\frac{1}{2}Ds) \approx \frac{1}{2}Ds$ and $\tanh(qh) \approx qh$. We then find:

$$\kappa^2 = \kappa_\alpha^2 \left(\frac{1 + \frac{2h}{\phi_0 D}}{1 + \frac{2h}{\phi_0 D} \frac{\kappa_g^2}{\kappa_l^2}} \right) \tag{B.8}$$

In figure B.2, we have drawn the phase velocity $\omega/\mathcal{R}e(\kappa)$ and the attenuation coefficient $\mathcal{I}m(\kappa)$ as a function of angular frequency. When the influence
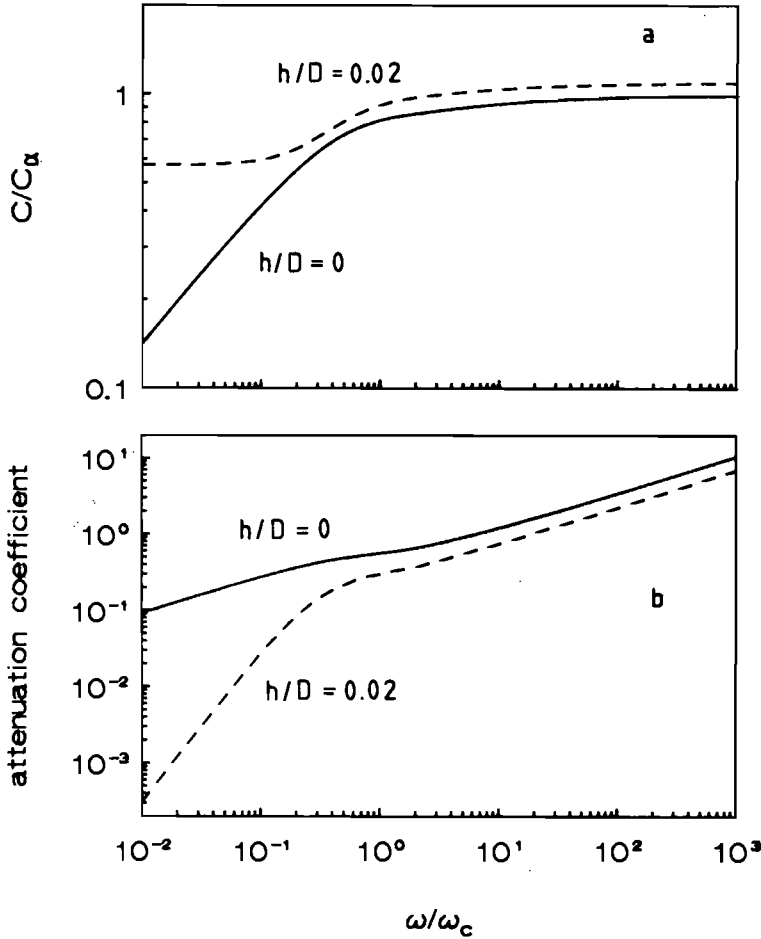

Figure B.2: *Reduced phase velocities (a) and attenuation coefficients (b) as a function of reduced angular frequency. c_α is the high frequency limit of the phase velocity when the liquid-filled gap is not taken into account. c_α is also defined in section 3.1.*

of the liquid-filled gap is taken into account, we find that, over the entire

frequency range, the phase velocity is higher, and the damping is less. In one-dimensional theory, both effects can be represented by introducing an "effective" tortuosity parameter α_{eff} and an "effective" permeability k_{eff}. The effective tortuosity should be less than α_∞ to account for the high frequency limit of the phase velocity, and k_{eff} should be greater than k_0 to account for the damping effect. Both effects have also been observed experimentally. Van der Grinten, van Dongen & van der Kogel (1985, 1987) introduced an effective tortuosity to account for the phase velocity of the second compressional wave in a porous sand column, and in chapter 7, we showed that the introduction of a higher permeability value gives a better explanation of the experimentally observed damping of the second compressional wave in a Bentheim sandstone column. A quantitative explanation of the observed phenomena is only possible when also the elasticity of the porous material is taken into account. This, however, implies a severe complication of the dynamic equations.

For a sand column, it was found previously (Van der Grinten *et al.* 1985, 1987) that a good match between experiment and one-dimensional theory was obtained by the introduction of an "effective" constrained modulus K_{eff}, the value of which is less than the value of K_p. In chapter 7, we showed that this also holds for a Bentheim sandstone column.

The liquid-filled gap may also influence wave propagation and damping in case the pore fluid consists of a water-air mixture. Therefore, we have again compared the experimental data of section 7.3 to linear one-dimensional theory. In this case, however, the computations were performed with the "effective" parameters $K_{eff} = 4.5$ GPa and $\alpha_{eff} = 1.45$ (Van der Grinten *et al.* 1985, 1987). The results are shown in figures B.3. We find that the agreement between experiment and theory is quite satisfactory.
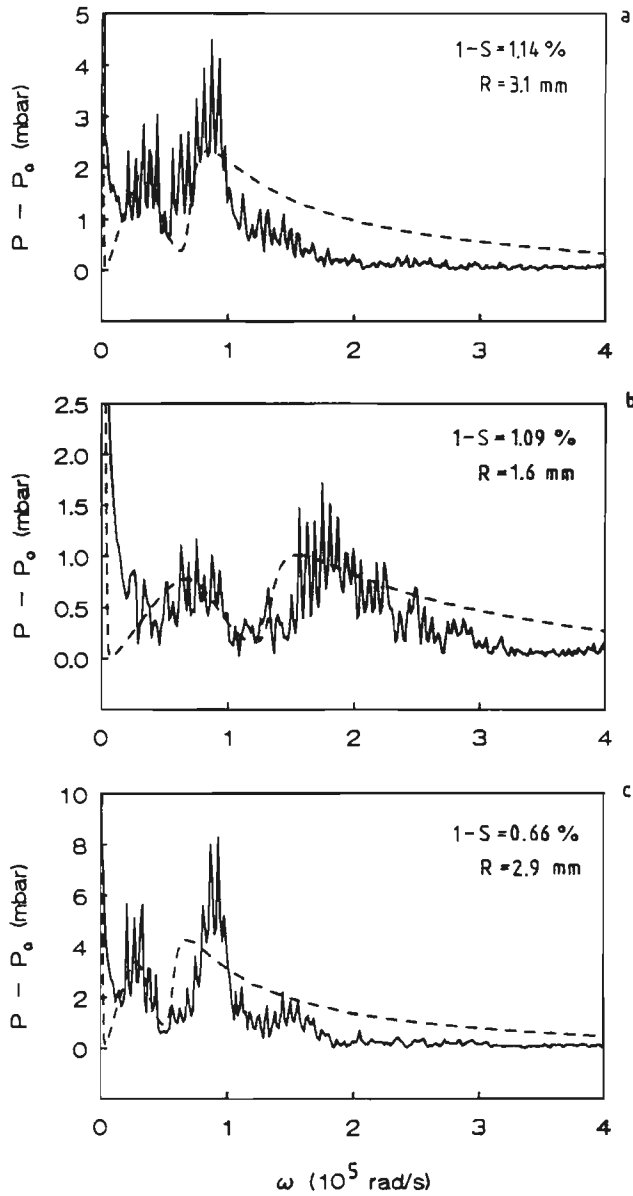
Figure B.3: *Power spectra of recorded (drawn lines) and computed (dashed lines) pore pressure signals. The computations were performed with the "effective" parameters $K_{eff} = 4.5$ GPa and $\alpha_{eff} = 1.45$. Acoustic damping was not included. a: $1 - s = 1.14$ %, $R = 3.1$ mm; b: $1 - s = 1.09$ %, $R = 1.6$ mm; c: $1 - s = 0.66$ %, $R = 2.9$ mm.*

References

Achenbach, J.D. 1973. *Wave propagation in elastic solids.* North-Holland Publishing Co.

Anderson, A.L. & Hampton, L.D. 1980 Acoustics of gas-bearing sediments I. Background. *J. Acoust. Soc. Am.* **67**, 1865-1889.
II. Measurements and models. *J. Acoust. Soc. Am.* **67**, 1890-1903.

Attenborough, K. 1987. On the acoustic slow wave in air-filled granular media. *J. Acous. Soc. Am.* **81**, 93-102.

Auriault, J.L. 1980. Dynamic behaviour of a porous medium saturated by a Newtonian fluid. *Int. J. Engng. Sci.* **18**, 775-785.

Auriault, J.L., Borne, L. & Chambon, R. 1985. Dynamics of porous saturated media, checking of the generalized law of Darcy. *J. Acous. Soc. Am.* **77**, 1641-1650.

Bachmat, Y & Bear, J. 1987. The concept and size of a REV. In *Proc. of the 1985 NATO Advanced Study Institute on the Fundamentals of Transport Phenomena in Porous Media* (ed. J. Bear & M.Y. Corapcioglu). Nijhoff, 3-20.

Barends, F.B.J. 1980. *Non-linearity in groudwater flow.* L.G.M. mededelingen 21 (Reprint of Ph.D. Thesis), Delft Geotechnics.

Bear, J. 1972. *Dynamics of Fluids in Porous Media.* American Elsevier.

Bear, J. & Bachmat, Y. 1984. Transport phenomena in porous media - basic equations. In *Proc. of the 1982 NATO Advanced Study Institute on the Fundamentals of Transport Phenomena in Porous Media* (ed. J. Bear & M.Y. Corapcioglu). Nijhoff, 3-62.

Bear, J. & Bachmat, Y. 1990. *Introduction to Modeling of Transport Phenomena in Porous Media.* Kluwer.

Beasley, J.D. & Torquato, S. 1988. New bounds on the permeability of a random array of spheres. *Phys. Fluids* **A** 1, 199-207.

Beavers, G.S. & Sparrow, E.M. 1969. Non-Darcy Flow Through Fibrous Porous Media. *J. Appl. Mech.* **36**, 711-714.

Beavers, G.S., Sparrow, E.M. & Rodenz, D.E. 1973. Influence of Bed Size on the Flow Characteristics and Porosity of Randomly Packed Beds of Spheres. *J. Appl. Mech.* **40**, 655-660.

Bedford, A. & Stern, M. 1983. A model for wave propagation in gassy sediments. *J. Acoust. Soc. Am.* **73**, 409-417.

Bedford, A., Costley, R.D. & Stern, M. 1984. On the drag and virtual mass coefficients in Biot's equations. *J. Acous. Soc. Am.* **76**, 1804-1809.

Been, K. 1981. Nondestructive soil bulk density measurements by X-ray attenuation. *Geotechnical Testing J.* 4, 169-176.

Berryman, J.G. 1980. Confirmation of Biot's theory. *Appl. Phys. Lett.* **37**, 382-384.

Berryman, J.G. 1981. Elastic wave propagation in fluid-saturated porous media I. *J. Acous. Soc. Am.* **69**, 416-424.
II. *J. Acous. Soc. Am.* **70** 1754-1756.

Berryman, J.G., Thipgen, L. & Chin, R.C.Y. 1988. Bulk elastic wave propagation in partially saturated porous solids. *J. Acoust. Soc. Am.* **84**, 360-373.

Biot, M.A. 1941. General Theory of Three-Dimensional Consolidation. *J. Appl. Phys.* **12**, 155-164.

Biot, M.A. 1955. Theory of Elasticity and Consolidation for a Porous Anisotropic Solid. *J. Appl. Phys.* **26**, 182-185.

Biot, M.A. 1956. Theory of propagation of elastic waves in a fluid-saturated solid. I. Low frequency range. *J. Acoust. Soc. Am.* **28**, 168-178.
II. Higher frequency range. *J. Acoust. Soc. Am.* **28**, 179-191.

Biot, M.A. & Willis, D.G. 1957. The Elastic Coefficients of the Theory of Consolidation. *J. Appl. Mech.* **24**, 594-601.

Biot, M.A. 1961. Generalized Theory of Acoustic Propagation in Porous Dissipative Media. *J. Acous. Soc. Am.* **34**, 1254-1264.

Bird, R.B., Stewart, W.E. & Lightfoot, E.N. 1960. *Transport Phenomena.* John Wiley and Sons.

Boender, W., Chesters, A.K. & van der Zanden, A.J.J. 1991. An approximate analytical solution of the hydrodynamic problem associated with an advancing liquid-gas contact line. *Int. J. Multiphase Flow* **17**, 661-676.

Boulon, M. 1988. Numerical and physical modelling of piles behaviour under monotonous and cyclic loading. In *Proc. Int. Symp. on Modelling Soil-Water-Structure Interactions* (ed. P.A. Kolkman, J. Lindenberg & K.W. Pilarczyk). Balkema, 285-293.

Bourbié, T., Coussy, O. & Zinszner, B. 1987. *Acoustics of porous media.* Gulf Publishing Co.

Brown, R.J.S. & Korringa, J. 1975. On the dependence of the elastic properties of a porous rock on the compressibility of the pore fluid. *Geophysics* **40**, 608-616.

Brown, R.J.S. 1980. Connection between formation factor for electrical resistivity and fluid-solid coupling factor in Biot's equation for acoustic waves in fluid-filled porous media. *Geophysics* **45**, 1269-1275.

Burridge, R. & Keller, J.B. 1981. Poroelasticity equations derived from microstructure. *J. Acoust. Soc. Am.* **70**, 1140-1146.

Carman, P.C. 1956. *Flow of Gases Through Porous Media.* Butterworths.

Chandler, R.N. 1981. Transient streaming potential measurements on fluid-saturated porous structures: An experimental verification of Biot's slow wave in the quasi-static limit. *J. Acoust. Soc. Am.* **70**, 116-121.

Chandler, R.N. & Johnson, D.L. 1981. The equivalence of quasistatic flow in fluid-saturated porous media and Biot's slow wave in the limit of zero frequency. *J. Appl. Phys.* **52**, 3391-3395.

Charlaix, E., Kushnick, A.P. & Stokes, J.P. 1988. Experimental Study of Dynamic Permeability in Porous Media. *Phys. Rev. Lett.* **61**, 1595-1598.

Cheruvier, E. & Winkler, K.W. 1987. Field example of in situ permeability indication from full acoustic wavetrains. In *Proc. SPWLA Twenty-Eight Annual Logging Symp.*

Cheng, C.H. & Toksöz, M.N. 1981. Elastic Wave Propagation in a Fluid-Filled Borehole and synthetic Acoustic Logs. *Geophysics* **46**, 1042-1053.

Coulaud, O., Morel, P. & Caltagirone, J.P. 1988. Numerical modelling of nonlinear flow through a porous medium. *J. Fluid Mech.* **190**, 393-407.

Cuvelier, C., van Steenhoven, A.A. & Segal, G. 1986. *Finite element methods and Navier-Stokes equations.* Reidel.

Darcy, H.P.G. 1856. *Les Fontaines Publiques de la Ville de Dijon.* Victor Dalmond, Paris.

Davidson, J.M., Biggar, J.W. & Nielsen, D.R. 1963. Gamma-radiation attenuation for measuring bulk density and transient water flow in porous materials. *J. Geophys. Res.* **68**, 4777-4783.

De Josselin de Jong, C. 1956. What happens in soil during pile driving ? *De Ingenieur* **68**, B77-B88.

De Swart, J.G. & Groenevelt, P.H. 1971. Column scanning with 60 keV gamma radiation. *Soil Science* **112**, 419-424.

Devin, C. 1959. Survey of Thermal, Radiation and Viscous Damping of Pulsating Air Bubbles in Water. *J. Acous. Soc. Am.* **31**, 1654-1667.

Dontsov, V.E., Kuznetsov, V.V. & Nakoryakov, V.E. 1987. Pressure waves in a porous medium saturated with a gassy fluid. *Mekh. Zhidk. i Gaza* 4, 85-92.

Dowling, A.P. & Ffowcs Williams, J.E. 1983. *Sound and sources of sound.* Ellis Horwood Publishers.

Dullien, F.A.L. 1975. Single phase flow through porous media and pore structure. *Chem. Eng. J.* **10**, 1-34.

Ebbens, E.H., Molenkamp, F. & Ruygrok P. 1988. Effect of wave impact on asphalt revetments of Dutch sea dikes. In *Proc. Int. Symp. on Modelling Soil-Water-Structure Interactions* (ed. P.A. Kolkman, J. Lindenberg & K.W. Pilarczyk). Balkema, 271-281.

Forchheimer, P.H. 1901. Wasserbewegung durch Boden. *Zeitschrift des Vereines Deutcher Ingenieure* **45**, 1782-1788.

Garg, S.K. & Nayfeh, A.H. 1986. Compressional waves propagation in liquid-saturated elastic porous media. *J. Appl. Phys.* **60**, 3045-3055.

Gassmann, F. 1951. Elastic Waves through a Packing of Spheres. *Geophysics* **16**, 673-685.

Geertsma, T. & Smit, D.C. 1961. Some aspects of elastic waves propagation in fluid-saturated porous solids. *Geophysics* **26**, 169-181.

Hampton, L.D. 1974. *Physics of sound in marine sediments.* Plenum.

Hovem, J.M. & Ingram, G.D. 1979. Viscous attenuation of sound in saturated sand. *J. Acous. Soc. Am.* **66**, 1807-1812. Hsui, A.T. & Toksöz, M.N. 1986. Application of an acoustic model to determine in situ permeability of a borehole. *J. Acous. Soc. Am.* **79**, 2055-2059.

Johnson, D.L. 1980. Equivalence between fourth sound in liquid He II at low temperatures and the Biot slow wave in consolidated porous media. *Appl. Phys. Lett.* **37**, 1065-1067.

Johnson, D.L. & Sen, P.N. 1981. Multiple scattering of acoustic waves with application to the index of refraction of fourth sound. *Phys. Rev.* **B 24**, 2486-2496.

Johnson, D.L. & Plona, T.J. 1982. Acoustic slow waves and the consolidation transition. *J. Acous. Soc. Am.* **72**, 556-565.

Johnson, D.L., Plona, T.J., Scala, C., Pasierb, F. & Kojima, H. 1982. Tortuosity and Acoustic Slow Waves. *Phys. Rev. Lett.* **49**, 1840-1844.

Johnson, D.L., Koplik, J. & Dashen, R. 1987. Theory of dynamic permeability and tortuosity in fluid-saturated porous media. *J. Fluid Mech.* **176**, 379-402.

Johnson, D.L. 1989. Scaling Function for Dynamic Permeability in Porous Media. *Phys. Rev. Lett.* **63**, 580.

Korringa, J. 1981. On the Biot-Gassmann equations for the elastic moduli of porous rocks (Critical comment on a paper by J.G. Berryman). *J. Acous. Soc. Am.* **70**, 1752-1753.

Lamb, H. 1963. *Hydrodynamics.* Cambridge University Press.

Landau, L.D. & Lifshitz, E.M. 1959. *Fluid Mechanics.* Pergamon.

Larson, R.E. & Higdon, J.J.L. 1989. A periodic grain consolidation model of porous media. *Phys. Fluids* **A 1**, 38-46.

Lévy, T. 1979. Propagation of waves in a fluid-saturated porous elastic solid. *Int. J. Engng. Sci.* **17**, 1005-1014.

Love, A.E.H. 1944. *A Treatise on the Mathematical Theory of Elasticity.* Dover Publications.

Macdonald, I.F., El Sayed, M.S., Mow,K. & Dullien, F.A.L. 1979. Flow through porous media - The Ergun equation revisited. *Ind. Eng. Chem. Fundam.* **18** 199-208.

Mei, C.C. & Auriault, J.L. 1991. The effect of weak inertia on flow through a porous medium. *J. Fluid. Mech.* **222**, 647-663.

Paterson, N.R. 1956. Seismic wave propagation in porous granular media. *Geophysics* **21**, 691-714.

Pfriem, H. 1940. Zur thermischen Dämpfung in kugelsymmetrisch schwingende Gasblasen. *Akust. Z.* **5**, 202.

Plesset, M.S. 1949. The dynamics of cavitation bubbles. *J. Appl. Mech.* **16**, 277-282.

Plona, T.J. 1980. Observation of a second bulk compressional wave in a porous medium at ultrasonic frequencies. *Appl. Phys. Lett.* **36**, 259-261.

Rubenstein, J. & Torquato, S. 1989. Flow in random porous media: mathematical formulation, variational principles and rigorous bounds. *J. Fluid Mech.* **206**, 25-46.

Ruygrok, P.A. & van der Kogel, H. 1980. Some results of impact experiments on nearly saturated and dry sand. In *Proc. Int. Symp. on Soils under Cyclic and Transient Loading* (ed. G.N. Pande & O.C. Zienkiewicz). Balkema, 211-224.

Scheidegger, A.E. 1974. *The Physics of Flow Through Porous Media.* University of Toronto Press.

Sheng, P. & Zhou, M.-Y. 1988. Dynamic Permeability in Porous Media. *Phys. Rev. Lett.* **61**, 1591-1594.

Sheng, P., Zhou, M.Y., Charlaix, E., Kushnick, A.P. & Stokes, J.P. 1989. Reply to D.L. Johnson. 1989. Scaling Function for Dynamic Permeability in Porous Media. *Phys. Rev. Lett.* **63**, 581.

Sillen, C.W.P.M. 1983. *The effect of gas bubble evolution on the energy efficiency in water electrolysis.* Ph.D. Thesis. Eindhoven University of Technology.

Smeulders, D.M.J., De la Rosette, J.P.M. & van Dongen, M.E.H. 1992. Waves in partially saturated porous media. *Transport in Porous Media.* To be published.

Smeulders, D.M.J., Eggels, R.L.G.M. & van Dongen, M.E.H. 1992. Dynamic permeability: reformulation of theory and new experimental and numerical data. *J. Fluid Mech.* To be published.

Sniekers, R.W.J.M., Smeulders, D.M.J., van Dongen, M.E.H. & van der Kogel, H. 1989. Pressure wave propagation in a partially water-saturated porous medium. *J. Appl. Phys.* **66**, 4522-4524.

Spitzer, L. 1943. *Acoustical properties of gas bubbles in a liquid.* NRDC Rep. 6, 1-sr20-918, PB31026. Columbia University Office of Scientific Research and Development.

Stoll, R.D. 1974. Acoustic waves in saturated sediments. In *Physics of sound in marine sediments* (ed. L.D. Hampton). Plenum.

Terzaghi, K. 1925. *Erdbaumechanik auf Bodenphysikalischer Grundlage.* F. Deuticke, Leipzig.

Terzaghi, K. 1944. *Theoretical Soil Mechanics.* John Wiley and Sons, New York.

Teunissen, J.A.M. 1982. Mechanics of a fluid-gas mixture in a porous medium. *Mechanics of Materials* 1, 229-237.

Van der Grinten, J.G., van Dongen, M.E.H. & van der Kogel, H. 1985. A shock tube technique for studying pore pressure propagation in a dry and water-saturated porous medium. *J. Appl. Phys.* **58**, 2937-2942.

Van der Grinten, J.G., van Dongen, M.E.H. & van der Kogel, H. 1987. Strain and pore pressure propagation in a water-saturated porous medium. *J. Appl. Phys.* **62**, 4682-4687.

Van der Grinten, J.G.M. 1987. *An experimental study of shock-induced wave propagation in dry, water-saturated, and partially saturated porous media.* Ph.D. Thesis. Eindhoven University of Technology.

Van der Grinten, J.G., van Dongen, M.E.H. & van der Kogel, H. 1988. An experimental study of shock-induced wave propagation in dry, water-saturated, and partially saturated porous media. In *Proc. Int. Symp. on Modelling Soil-Water-Structure Interactions* (ed. P.A. Kolkman, J. Lindenberg & K.W. Pilarczyk). Balkema, 469-478.

Van Stralen, S. & Cole, R. 1979. *Boiling Phenomena.* Hemisphere Publishing Co.

Van Wijngaarden, L. 1970. On the structure of shock waves in liquid-bubble mixtures. *Appl. Sci. Res.* **22**, 366-381.

Van Wijngaarden, L. 1972. One dimensional flow of liquids containing small gas bubbles. *Annu. Rev. Fluid Mech.* **4**, 369-395.

Verruijt, A. 1982. Some remarks on the principle of effective stress. In *Proc. IUTAM Conf. on Deformation and Failure of Granular Materials* (ed. P.A. Vermeer & J.H. Luger). Balkema, 167-170.

Verruijt, A. 1982. The Theory of Consolidation. In *Proc. NATO Advanced Study Institute on Mechanics of Fluids in porous media.* Nijhoff, 349-368.

Ward, C.A., Johnson, W.R., Venter, R.D., Ho, S., Forest, T.W. & Fraser, W.D. 1983. Heterogeneous bubble nucleation and conditions for growth in a liquid-gas system of constant mass and volume. *J. Appl. Phys.* **54**, 1833-1843.

Whitaker, S. 1977. Simultaneous Heat, Mass, and Momentum Transfer in Porous Media: A Theory of Drying. *Advances in Heat Transfer* **13**, 119-203.

Whitaker, S. 1986. Flow in Porous Media I. A technical derivation of Darcy's law. *Transport in Porous Media* **1**, 3-25.
II. The governing equations for immiscible, two-phase flow. *Transport in Porous Media* **1**, 105-125.
III. Deformable Media. *Transport in Porous Media* **1**, 127-154.

Yavari, B. & Bedford, A. 1990. The Biot drag and virtual mass coefficient for face centered cubic granular materials. *Int. J. Multiphase Flow* **16**, 885-897.

Zwikker, C. & Kosten, C.W. 1949. *Sound absorbing materials.* American Elsevier, New York.

Abstract

The propagation and damping of compressional waves in a porous medium are investigated, both theoretically and experimentally, in case the pore liquid contains a small volume fraction of gas.

The effect of oscillating gas bubbles is taken into account by the introduction of a frequency dependent fluid bulk modulus, which is incorporated in the Biot theory. This dynamic fluid bulk modulus relates the exerted fluid pressure to a change in the average fluid volume, and is strongly dependent on the dynamic gas bubble behaviour. Oscillating gas bubbles in a partially saturated porous medium are damped by means of thermal, Darcy, viscous and acoustic mechanisms. A careful analysis of all mechanisms involved, shows that the Darcy damping is by far the most important. It can be represented by a dynamic, frequency dependent, permeability. In a separate set-up, this dynamic permeability is measured and compared to theoretical results from homogenization theory. Measurements are performed on five different fully water-saturated porous samples. Over the entire domain of reduced frequencies, the measured data for the dynamic permeability are in agreement with a theoretical scaling function.

It is shown that even minor gas fractions largely influence the dynamic fluid bulk modulus and, consequently, the wave propagation phenomena in a porous medium. Close to gas bubble resonant frequencies, the compressional waves are very strongly damped. In this way, a porous medium, with small gas inclusions in the pore liquid, can be described in terms of a frequency band filter for pressure waves.

Wave experiments are performed by means of a shock tube technique. A vertical shock tube generates a pressure step wave in air, which is transmitted into the water layer on top of a porous column. This wave partially reflects, partially transmits into the porous medium. Two different cylindrical porous samples are used. One of them consists of sand particles, glued together by means of an epoxy resin; the other is a column of natural Bentheim sandstone. Both samples are equally equipped with miniature pore pressure transducers. The porosities, steady-state permeabilities and tortuosities of both samples are determined experimentally. Shock tube wave experiments are performed on both water-saturated porous columns. Two longitudinal pore pressure waves are observed, as is also theoretically predicted. There is one wave in which fluid and skeletal velocities are in phase, and another in which they are in opposite phase. The latter has higher damping and lower phase velocity. It is shown that for a detailed description of the observed phenomena, it is necessary to take into account the liquid-filled gap between the porous sample and the shock tube wall.

Particular care is paid to the preparation of a homogeneous water-air mixture in the pores of both samples. A super-saturation technique is described, which implies that a diffusion dominated air bubble growth is induced in the pores of the porous samples. Mean gas bubble radius and concentration are determined by means of a series of successive compressibility experiments. Subsequently, a series of wave experiments is performed on both partially saturated porous columns. In this case, the pore pressures at several distances from the top of both porous samples display an oscillatory behaviour. Detailed study of this behaviour for several gas bubble radii and concentrations is presented for the sand column. In all cases, the observed oscillations consist of two distinct frequency bands, with two distinct maxima. The partially saturated porous medium acts as a frequency band filter. Two frequency bands are easily transmitted into the porous medium and have high propagation velocities and low damping factors. The amplitudes of the oscillations are in agreement with the theoretical analysis. The location of the first frequency maximum is in quantitative agreement with the linear one-dimensional theoretical analysis. The location of the second frequency maximum is particulary sensitive to the influence of the liquid-filled gap between the porous sample and the shock tube wall, which can be represented by the introduction of "effective" skeletal properties. The location of the two frequency maxima appears to depend strongly on mean air bubble radius and concentration. For smaller air volume fractions and for greater air bubble radii, both frequency maxima are shifted towards lower frequencies. This tendency is in agreement with the theoretical analysis.

Samenvatting

Theoretisch en experimenteel onderzoek is verricht naar de voortplanting en demping van drukgolven in poreuze media, waarvan de porievloeistof een geringe hoeveelheid lucht bevat.

De invloed van oscillerende luchtbellen wordt in rekening gebracht door in de Biot theorie een frequentieafhankelijke compressiemodulus van de porievloeistof op te nemen. Deze dynamische compressiemodulus legt een verband tussen de uitgeoefende poriedruk en de verandering van het gemiddelde vloeistofvolume in de poriën, en is in hoge mate afhankelijk van het dynamisch belgedrag. Oscillerende luchtbellen in gedeeltelijk verzadigde poreuze materialen worden gedempt door middel van thermische, Darcy, visceuze en acoustische dissipatiemechanismen. Een zorgvuldige analyse laat zien dat de Darcy demping veruit het belangrijkst is. Deze Darcy demping kan worden beschreven met behulp van een dynamische, frequentieafhankelijke, doorlatendheid. In een afzonderlijke opstelling wordt de dynamische doorlatendheid gemeten van vijf verschillende poreuze materialen, die vooraf volledig met water verzadigd zijn. De metingen worden vergeleken met voorspellingen op grond van de homogenisatietheorie. De gemeten doorlatendheid blijkt over het gehele gebied van dimensieloze frequenties overeen te komen met een theoretische schalingsfunctie.

Aangetoond wordt dat zelfs zeer geringe hoeveelheden lucht de dynamische compressiemodulus van de porievloeistof in hoge mate beïnvloeden en, daarmee samenhangend, een grote invloed uitoefenen op de golfvoortplanting in poreuze materialen in het algemeen. Nabij de resonantiefrequentie van de luchtbellen worden de drukgolven sterk gedempt. Een poreus materiaal met kleine luchtinsluitsels in de poriën kan dus worden opgevat als een frequentiebandfilter.

De golfexperimenten worden verricht met een schokbuismethode. Een verticale schokbuis genereert een stapvormige drukgolf in lucht, die zich vervolgens voortplant in de waterlaag boven een poreuze kolom. Deze golf reflecteert voor een deel aan de poreuze kolom, en plant zich voor een ander deel voort in de poreuze kolom. Er wordt gebruik gemaakt van twee verschillende poreuze kolommen. De een bestaat uit zandkorrels die onderling zijn verlijmd met een epoxyhars; de ander is een Bentheimer zandsteenkolom. Beide kolommen zijn voorzien van miniatuur poriedrukopnemers. De porositeit, doorlatendheid en tortuositeit van beide kolommen worden experimenteel bepaald. Vervolgens worden golfexperimenten verricht op beide kolommen, die vooraf volledig verzadigd zijn met water. Zoals op theoretische gronden verwacht mag worden, worden twee longitudinale poriedrukgolven waargenomen. Bij de eerste golf zijn de snelheden van het poreuze

materiaal en van de porievloeistof met elkaar in fase, terwijl er bij de tweede golf sprake is van snelheden in tegenfase. De tweede golf wordt sterker gedempt, en heeft een kleinere fasesnelheid. Aangetoond wordt dat het voor een gedetailleerde beschrijving van de waargenomen verschijnselen noodzakelijk is de met water gevulde spleet tussen de poreuze kolom en de wand van de schokbuis in de beschouwingen te betrekken.

Veel zorg is besteed aan de preparatie van een homogeen mengsel van water en luchtbellen in de poriën van beide poreuze kolommen. Een oververzadigingstechniek wordt beschreven, die erop neerkomt dat er een aangroei van luchtbellen in de poriën wordt geïnduceerd. Deze belgroei is overwegend een diffusieproces. De concentratie en de gemiddelde straal van de luchtbellen worden bepaald door middel van een reeks opeenvolgende compressibiliteitsmetingen. Vervolgens wordt een reeks golfexperimenten beschreven, uitgevoerd op beide gedeeltelijk verzadigde poreuze kolommen. Nu vertonen de poriedruksignalen op verschillende afstanden van de bovenkant van beide kolommen een oscillerend gedrag. Voor de verlijmde zandkolom is dit gedrag onderzocht als functie van de concentratie en de gemiddelde straal van de luchtbellen. In alle gevallen bestaan de waargenomen oscillaties uit twee afzonderlijke frequentiebanden met twee afzonderlijke maxima. De gedeeltelijk verzadigde poreuze kolom gedraagt zich als een frequentiebandfilter. Twee frequentiebanden worden relatief eenvoudig ingekoppeld in de poreuze kolom, worden in geringe mate gedempt, en hebben een hoge voortplantingssnelheid. De amplitudes van de oscillaties zijn in overeenstemming met de theorie. De ligging van het eerste frequentiemaximum is in overeenstemming met de lineaire, eendimensionale theorie. De ligging van het tweede frequentiemaximum wordt sterk beïnvloed door de aanwezigheid van de met vloeistof gevulde spleet tussen de poreuze kolom en de wand van de schokbuis. Deze invloed kan worden verdisconteerd door "effectieve" eigenschappen van de poreuze kolom te introduceren. De ligging van beide frequentiemaxima blijkt sterk afhankelijk te zijn van de concentratie en de gemiddelde straal van de luchtbellen. Zowel voor geringere volumefracties lucht als voor grotere gemiddelde belstralen, blijkt de ligging van beide frequentiemaxima te verschuiven naar lagere frequentiewaarden. Deze tendens is in overeenstemming met de theoretische analyse.

Gassmann, F. 1951. Elastic Waves through a Packing of Spheres. *Geo-*

Nawoord

Curriculum vitae

14 augustus 1961	geboren te Nuenen
mei 1979	diploma gymnasium β Augustinianum Eindhoven
juni 1987	diploma Technische Universiteit Delft faculteit der Lucht- en Ruimtevaarttechniek vakgroep Theoretische Aërodynamica eerstegraads onderwijsbevoegdheid wis- en natuurkunde
augustus 1987 - december 1987	leraar wis- en natuurkunde Lodewijk Makeblijde College Rijswijk
maart 1988 - maart 1992	promovendus (AIO) in dienst van Stichting Fundamenteel Onderzoek der Materie (FOM) project ETN 37.1274 (Voortplanting van drukgolven in gedeeltelijk met vloeistof verzadigde poreuze media)
september 1991	managementtraining Management Development Centre (MDC) Nijenrode

Stellingen

1. De structuurparameters $\delta^2/8\xi$ en n^2/s, zoals die voorkomen bij Biot en Attenborough, zijn in feite identiek aan de door Johnson *et al.* geïntroduceerde gelijkvormigheidsparameter M.
   Biot, M.A. 1956. J. Acous. Soc. Am. 28, 168-191.
   Attenborough, K. 1983. J. Acous. Soc. Am. 77, 785-799.
   Johnson, D.L., Koplik, J. & Dashen, R. 1987. J. Fluid Mech. 176, 379-402.

2. Het is niet te verwachten dat de tweede Biot golfmode experimenteel zal worden waargenomen in poreuze media met doorlatendheden in het gebied beneden de 1 Darcy.

3. Chroomoxide-deeltjes, verkregen door het verhitten van een nikkel/chroom-draad, zijn uitstekend toepasbaar bij het genereren van een monodisperse nevel door adiabatische expansie van een gas/damp mengsel.
   Smolders, H.J., Willems, J.F., de Lange, H.C. & van Dongen, M.E.H. 1989. A.I.P. Conf. Proc. 17th ISSWST, 802-807.

4. De wetenschappelijke controverse, onstaan bij de beschrijving van een "unjacketed test" op met vloeistof gevulde poreuze media, is een gevolg van een onzorgvuldige definitie van de voorkomende grootheden.
   Berryman, J.G. 1981. J. Acous. Soc. Am. 69, 416-424.
   Korringa, J. 1981. J. Acous. Soc. Am. 70, 1752-1753.
   Berryman, J.G. 1981. J. Acous. Soc. Am. 70, 1754-1756.

5. Bij het bestuderen van golfverschijnselen in natuurlijke gesteenten, kan met vrucht gebruik worden gemaakt van kunstmatig aangemaakte, verlijmde poreuze media.

6. Bij de beschrijving van golfvoortplanting in poreuze media kan een poreuze cylinder waarvan de porievloeistof een geringe hoeveelheid luchtbellen bevat, opgevat worden als een frequentiebandfilter.

7. In de theoretische aërodynamica kan bij de bestudering van een expansiewaaier in een niet-homentrope stroming op elegante wijze gebruik gemaakt worden van een LMS- (Ludford, Martin, Stanyukovich) gas.
   Steketee, J.A. 1972. Quarterly Appl. Math. 30, 167-181.
   Ludford, G.S.S. & Martin, M.H. 1954. Comm. Pure Appl. Math. 7, 45-63.
   Stanyukovich, K.P. 1960. Unsteady motion of continuous media. New York.

8. Vochtabsorptie in poreuze baksteen kan nauwkeurig worden bestudeerd met behulp van neutronenbundelverzwakking.

9. Het zogenaamde "Sick Building Syndrome" is grotendeels een gevolg van het negeren van eenvoudige fysische wetten in de ontwerpfase. *Symposium "Sick Building Syndrome", 8 maart 1988, Utrecht.*

10. Het is begrijpelijk dat de ontwikkelingen van de kleurencopieerapparatuur de officiële geldscheppende instellingen grote zorgen baart. *Dit proefschrift, blz. 89, 91.*

Stellingen behorend bij het proefschrift: "On wave propagation in saturated and partially saturated porous media".
Eindhoven, 23 juni 1992   D.M.J. Smeulders